

4-1-2018

## Pressure Transient Techniques for Continuous Monitoring of CO<sub>2</sub> Storage/EOR

Nam Hoang Tran

*Louisiana State University and Agricultural and Mechanical College*

Follow this and additional works at: [https://digitalcommons.lsu.edu/gradschool\\_theses](https://digitalcommons.lsu.edu/gradschool_theses)



Part of the [Other Engineering Commons](#)

---

### Recommended Citation

Tran, Nam Hoang, "Pressure Transient Techniques for Continuous Monitoring of CO<sub>2</sub> Storage/EOR" (2018). *LSU Master's Theses*. 4661.

[https://digitalcommons.lsu.edu/gradschool\\_theses/4661](https://digitalcommons.lsu.edu/gradschool_theses/4661)

This Thesis is brought to you for free and open access by the Graduate School at LSU Digital Commons. It has been accepted for inclusion in LSU Master's Theses by an authorized graduate school editor of LSU Digital Commons. For more information, please contact [gradetd@lsu.edu](mailto:gradetd@lsu.edu).

# **PRESSURE TRANSIENT TECHNIQUES FOR CONTINUOUS MONITORING OF CO<sub>2</sub> STORAGE/EOR**

A Thesis

Submitted to the Graduate Faculty of the  
Louisiana State University and  
Agricultural and Mechanical College  
in partial fulfillment of the  
requirements for the degree of  
Master of Science

in

The Craft & Hawkins Department of Petroleum Engineering

by  
Nam Hoang Tran  
B.S., Louisiana State University, 2015  
May 2018

Copyright 2018 Nam Hoang Tran

I would like to dedicate my thesis to my beloved parents and grandfather, who I wish to carry on their American dream.

## Acknowledgments

This work would not be possible without Dr. Zeidouni, who was the only one in the petroleum department at Louisiana State University to give me the opportunity to work under him. Dr. Zeidouni has been supportive of my career goals and worked actively to provide me with great opportunities throughout my graduate studies. I would also like to thank the committee members for their guidance throughout my research guidance: Dr. Mayank Tyagi, Dr. Wesley Williams, and Dr. Hughes. The work presented in the thesis was not possible without the generous donation of the commercial reservoir model simulation software by Computer Modeling Group Ltd.

I am grateful to all my friends and colleagues I have met. A specific group of colleagues, I met during my undergraduate years at Louisiana State University, although no longer at LSU have continued to support me: Jeff Madacsi, Clay Curry, Cristina Espinoza, and Tim Schwartzenburg. Nobody has been more important to me in the pursuit of this project than my brother, mother and father. My brother, who has provided me a home during my studies and the reason I wanted to be an engineer from a young age. I truly wish to thank my mother and father for giving up their lives in Vietnam so that they could build their dreams through me in America.

## Table of Contents

Acknowledgments.....	iv
Abstract .....	vii
Chapter 1: Background .....	1
1.1 Leakage from CO <sub>2</sub> Geological Storage.....	1
1.2 Study Objectives .....	2
1.3 Thesis Outline and Chapter (Paper) Linkage.....	3
Chapter 2: Interpretation of Above-Zone Pressure Influence Time to Characterize CO <sub>2</sub> Leakage .....	5
2.1 Introduction.....	5
2.2 Physical Model and Mathematical Formulation .....	8
2.3 Analytical Solution .....	10
2.4 Verification of Analytical Model.....	12
2.5 Evaluation of Plume Size ( $b$ ) from $t_{inf}$ .....	20
2.6 Application for Plume Volume Estimation.....	21
2.7 Conclusions.....	27
Chapter 3: CO <sub>2</sub> Plume Characterization Using Pressure Arrival Time .....	29
3.1 Introduction.....	29
3.2 Methodology .....	32
3.3 Cases for Numerical Model .....	34
3.4 Determination of Average Gas Saturation .....	40
3.5 Results.....	42
Chapter 4: Pressure Transient Test to Constrain CO <sub>2</sub> Plume Boundaries .....	47
4.1 Introduction.....	47
4.2 Methodology .....	50
4.3 Model Setup.....	55
4.4 Results.....	57
4.5 Discussion .....	73
4.6 Conclusions.....	74

Chapter 5: Linear Composite Model with Harmonic Pulse Testing .....	76
5.1 Introduction .....	76
5.2 Overview of Pressure Pulse Processing .....	77
5.3 Methodology .....	77
5.4 Analytical Solution .....	79
5.5 Match for Homogenous Case.....	81
5.6 Discussion and Further Work .....	87
 Chapter 6: Discussion and Main Conclusions .....	 88
 References.....	 91
 Appendix: Analytical Solution Development .....	 100
 Appendix: Acknowledgement Forms .....	 103
 Vita.....	 105

## **Abstract**

Pressure well testing has been widely used in the oil and gas industry for determining reservoir properties and well conditions. More recently, studies have been done to show the applicability of well testing for the continuous monitoring of CO<sub>2</sub> storage projects. In the current thesis, we study a diverse range of pressure transient techniques with the same goal of characterizing CO<sub>2</sub>. The thesis finds that the use of pressure transient analysis is a strong tool for CO<sub>2</sub> monitoring. Each method discussed within the paper has its advantages and disadvantages. The first technique is able to determine the CO<sub>2</sub> plume extent in the reservoir, using a simple test, but relies on high resolution gauges and is unable to determine the location of the CO<sub>2</sub>. The second technique is able to determine the location of the plume boundary along with the average gas saturation but may require multiple monitoring locations inside and outside the plume to determine the boundary. The third method is able to determine the location of the plume boundary by use of a single well test, but other than the boundary, no other information can be derived. The last chapter builds the ground work for the first analytical linear composite model in the frequency domain. This approach has the potential to provide the most accurate representation of the CO<sub>2</sub> within the reservoir in an efficient way.



## **Chapter 1: Background**

### **1.1 Leakage from CO<sub>2</sub> Geological Storage**

Carbon dioxide (CO<sub>2</sub>) is injected in deep underground formations for two main applications. The first application is a means to cut CO<sub>2</sub> atmospheric emissions to mitigate climate change (IPCC 2005). The other application is for use in enhanced oil recovery (EOR). Although these are two separate occasions for CO<sub>2</sub> storage, with cooperation of the federal government and oilfield operators, studies have shown that coupled CO<sub>2</sub> EOR and storage projects may bring long-term benefits for both parties involved which may increase the number of storage projects in the future (Ettehadtavakkol, Lake, and Bryant 2014). CO<sub>2</sub> storage in deep saline aquifers consists of two stages. The first stage is the injection period in which CO<sub>2</sub> is injected at a high flow rate, displacing the brine. The second stage is the post-injection period in which after injection is stopped, the CO<sub>2</sub> plume continues to migrate due to its buoyancy and background hydraulic gradient (MacMinn and Juanes 2009). It is during this post-injection phase that the spatial distribution of injected CO<sub>2</sub> has important implications for the safety and liability of the CO<sub>2</sub> storage projects. It is required to determine the CO<sub>2</sub> footprint during the post-injection period. Such determination will help the operator to optimize the CO<sub>2</sub> injection to avoid any unwanted CO<sub>2</sub> exposure. The main risk of concern is leakage of CO<sub>2</sub> into the atmosphere or freshwater aquifers. For example, a leakage rate of 1% per year from 10 million tons geologically stored CO<sub>2</sub> would exceed the annual (2004) CO<sub>2</sub> emissions from all the power plants in North Dakota (Nelson 2005).

There are three basic leakage mechanisms that can occur during the post-injection phase. The first mechanism is fast-flow path leakage which would involve the movement of CO<sub>2</sub> into improperly abandoned wellbores and up poorly sealed or failed injection well casings. Leaks can also occur through transmissive faults or local pathways in the low-permeability caprock. The second

mechanism is slow leakage, which would mainly consist of gas transport by diffusion processes and loss of dissolved CO<sub>2</sub> due to the hydrodynamic flow of formation water out of the storage zone. The third leakage mechanism is gas desorption. Buoyancy forces would drive the desorbed CO<sub>2</sub> upward and then spread laterally once reaching the cap rock and can migrate to natural leakage pathways. As discussed above, the potential migration of CO<sub>2</sub> gas is known to be hazardous to the atmosphere, but is also detrimental if leaked into fresh water aquifers due to CO<sub>2</sub> intrusion resulting in dissolution and desorption of potentially toxic metals from minerals by acidic CO<sub>2</sub>-charged fluids, and migration of deep formation brine which may contain high concentrations of metals and radionuclides (Kampman, Bickle, Wigley, et al. 2014, Kampman, Bickle, Maskell, et al. 2014).

## 1.2 Study Objectives

This study's goals are to characterize CO<sub>2</sub> plumes in different aspects for reservoir models using a variety of pressure transient analysis techniques. The objectives of this study are:

1. Determine the plume's location and extent between a constant rate active well and a distant observation well by developing a three-region analytical model and making use of a defined influence time inversion;
2. Estimate the average gas saturation and possibly the location of the plume's boundary by utilizing the well which is injecting CO<sub>2</sub> the target zone and observe pressure through observation wells inside and outside the plume;
3. Find the plume boundary relative to a distant a single well outside the plume by use of treating the CO<sub>2</sub> as a constant pressure boundary and utilizing pressure diagnostic plots;

4. Modify the three-region composite model to derive analytical solution for a harmonic flow rate (instead of constant rate) and analyze the pressure pair in frequency domain to determine CO<sub>2</sub> location and extent relative to observation or injection well.

5. Investigate advantages and disadvantages of each method

### 1.3 Thesis Outline and Chapter (Paper) Linkage

The main purpose of this thesis is using a wide variety of well testing and pressure transient techniques to characterize the CO<sub>2</sub> plume in a target reservoir. The style of thesis by publication is conveniently used because each paper utilizes a different pressure transient analysis technique to characterize the CO<sub>2</sub> plume with the exception of Chapter 5 which proposes modifying a developed analytical solution to represent the model. Chapter 2 (published peer-reviewed article) starts off by developing an analytical solution for a linear three region composite model with a middle region containing CO<sub>2</sub>. The goal is to initiate a constant rate injection test and observe the pressure response at a monitoring well located out of the CO<sub>2</sub> plume. The influence time, defined as the time at which the pressure has reached the monitoring well dictated by the gauge resolution, is inverted to detail the extent of the plume. Chapter 2 concludes by applying the method to a more realistic case of CO<sub>2</sub> injection with a realistic shape. We then move into chapter 3 (published conference paper) which utilizes a CO<sub>2</sub> injection well which has already injected CO<sub>2</sub> into a target zone within the reservoir. The active well injects at a constant rate while multiple monitoring points within and outside the plume acquire pressure measurements. The arrival time taken by the first derivative pressure curve is taken and inverted with the use of a 2-phase diffusivity equation to determine the average gas saturation of the plume and (with sufficient monitoring points) the plume boundary. While average gas saturation may seem significant, with monitoring over time, increase or decrease of average gas saturation can help determine if remediation is needed. Chapter

4 (paper currently in review) differs from both chapter 2 and 3 in that the pressure transient analysis technique used is a single well test. Due to the significant contrast between mobility and storativity of the CO<sub>2</sub> and native fluids (oil or brine), the CO<sub>2</sub> boundary causes deviation in the pressure diagnostic response from that corresponding to previously identified heterogeneities. Using the superposition principle, we develop a relationship between the deviation time and the plume boundary. By using this we are able to determine the plume's boundary relative to the active well. In Chapter 5, we utilize the same model from Chapter 2, but instead of constant rate injection, the rate is varied harmonically. This produces sinusoidal pressure signals that can be analyzed in the frequency domain to determine the extent and the location of the plume (region 2). For this chapter the analytical model is developed and verified with a homogenous case where region contains the same fluid as outer regions. Although a perfect match is obtained, modifications to the analytical solution are suggested for future work. Chapter 6 summarizes the results and provide recommendations.

## **Chapter 2: Interpretation of Above-Zone Pressure Influence Time to Characterize CO<sub>2</sub> Leakage**

### **2.1 Introduction**

Storage of large volumes of Carbon Dioxide (CO<sub>2</sub>) in deep geological formations is required to cut atmospheric CO<sub>2</sub> emissions as a means to mitigate climate change (IPCC 2005). One of the main challenges facing safe deployment of CO<sub>2</sub> geological storage is the risk of leakage. CO<sub>2</sub> may migrate to overlying zones through pathways in the caprock separating the injection zone. CO<sub>2</sub> leakage to overlying zones has the potential to impact underground water resources and hydrocarbon exploitation. Improperly drilled and/or plugged and abandoned (P&A) wells, leaking faults/fractures, and stratigraphic variations in the caprock may provide leakage pathways for the injected CO<sub>2</sub>. If the leakage occurs in the vicinity of currently producing oil and gas wells, CO<sub>2</sub> can breakthrough and adversely affect hydrocarbon production. CO<sub>2</sub> leakage into shallow aquifers may cause dissolution (and allow mobilization) of harmful solids in the water (Little and Jackson 2010 and references therein). CO<sub>2</sub> leakage to the surface further impact humans and living habitats while making the operation of reducing the CO<sub>2</sub> emissions ineffective. Subsurface monitoring of CO<sub>2</sub> is required to ensure detecting any leakage before reaching shallow subsurface. Various monitoring approaches have been used for tracking the CO<sub>2</sub> within the injection zone using pressure (Kempka and Kühn 2013, Meckel et al. 2013), temperature (Hovorka, Meckel, and Treviño 2013, Liebscher et al. 2013, Zeidouni, Nicot, and Hovorka 2014), geophysical (Bergmann et al. 2016, Chadwick, Arts, and Eiken 2005, Couëslan et al. 2014), geochemical (Wandrey et al. 2011) and electromagnetic tomography (Bohm et al. 2015, Carcione et al. 2012) data. In addition, monitoring is performed in a permeable zone above the injection zone to determine whether CO<sub>2</sub>

This Chapter, previously published as Mehdi Zeidouni, Nam H. Tran, and Muhammad D. Munawar “Interpretation of above-zone pressure influence time to characterize CO<sub>2</sub> leakage” *Greenhouse Gases Science and Technology* Volume 7, Issue 6 (2017): 1050-1064 is reprinted here by permission of the authors.

migrated from the target injection zone to the above-zone (Hovorka, Meckel, and Treviño 2013, Meckel et al. 2013, Nunez-Lopez, Muñoz-Torres, and Zeidouni 2014). Above-zone pressure monitoring is especially important for CO<sub>2</sub> leakage detection and characterization because it can monitor a large area of investigation at low cost with high resolution and accuracy. Several studies focused on analyzing above-zone pressure data to gain information on the leakage pathways such as leaking wells and fractures and other heterogeneities in the caprock (Wang and Small 2014, Jung, Zhou, and Birkholzer 2013, Sun et al. 2013, Zeidouni and Pooladi-Darvish 2012a, b, Chabora and Benson 2009, Strandli and Benson 2013, Court et al. 2012, Zeidouni 2014, Zeidouni and Vilarrasa 2016, Mosaheb and Zeidouni 2017a, b). All these studies use pressure signal passively i.e. the pressure signal was only due to leakage. Hosseini and Alfi (2015) used pressure monitoring by performing pressure interference test in the above zone and analyzing its response for CO<sub>2</sub> leakage. CO<sub>2</sub> leakage in the above-zone can change its transmissibility ( $kh/\mu$ ) and storativity ( $\phi c_t$ ) which can be inferred from pressure interference tests. In this study we use pressure interference testing to gain information on the leaked CO<sub>2</sub> plume. We introduce a method to analyze the pressure interference times at a network of observation locations to determine the percent volume of leaked CO<sub>2</sub> on the line connecting each of the observation wells to the active pulse well (Figure 2.1). Pressure influence time ( $t_{inf}$ ) is the time at which the pressure change at the observation well is measurable for a given gauge resolution. We develop an analytical model to analyze the  $t_{inf}$  values for plume extent. The analytical model explicitly and deterministically provides the relationship between above-zone properties, the leaked plume, and the pressure measurements. We use the analytical model to invert  $t_{inf}$  values to determine the CO<sub>2</sub> volume percent (or CO<sub>2</sub> plume size) on the line connecting the pulse well to the observation well.

In the following, we start with the description of a physical model of a leaked plume in the above-zone. Next, the governing equations and associated initial and boundary conditions are defined followed by derivation of an analytical solution through combined Laplace and Fourier integral transforms. The analytical solution is verified against a limiting analytical solution where no leak exists and with comparison to numerical simulation results. Numerical simulations are also used to investigate the validity of the analytical model assumption on the plume shape. We refer to the time at which the pressure change at the observation well is measureable for a given gauge resolution as pressure influence time ( $t_{inf}$ ). We show that  $t_{inf}$  is independent of plume shape and can be only a function of the plume length on the line connecting the two interference test wells. With this observation, we show that  $t_{inf}$  can be used to determine the plume size (length) within a narrow confidence interval.

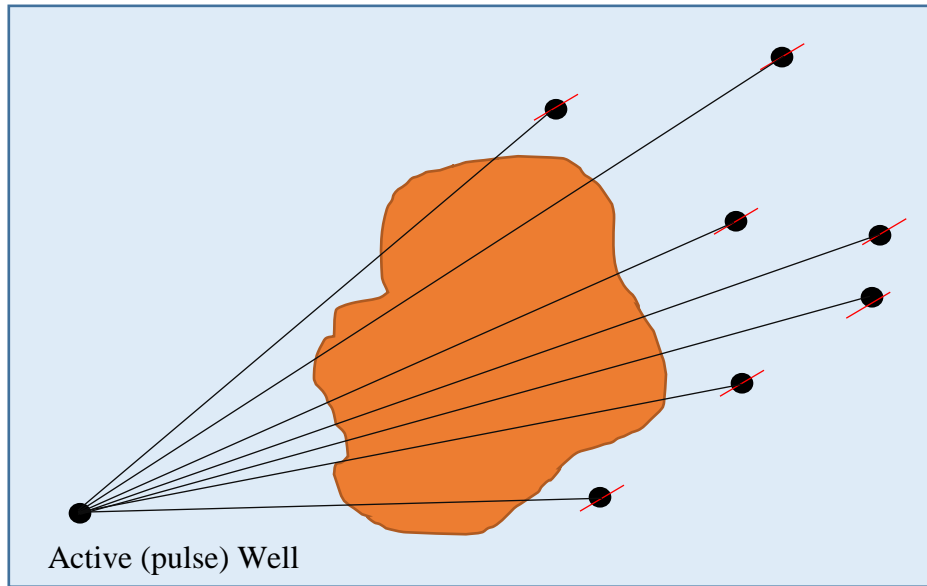


Figure 2.1. Pressure influence time ( $t_{inf}$ ) at a network of observation wells in response to injection/production at an active well can be inverted to determine the plume volume fraction (or plume size) on the line connecting each of the observation wells to the active well.

## 2.2 Physical Model and Mathematical Formulation

Shapes of the CO<sub>2</sub> plume migrated from the injection zone to the above-zone aquifer depends on the heterogeneities, gravity, capillary and viscous forces, structure of the host zone, and the nature of pathways allowing for CO<sub>2</sub> migration and generally can be of any shape (e.g. a plume shown in Figure 2.1). In order to derive an analytical model, we idealize the plume considering a linear composite system shown in Figure 2.2. The above-zone is divided into 3 regions where the altered region (region 2) represent the leaked plume. We develop an analytical solution to determine the pressure response at an observation well in response to a constant rate production/injection at the active well. The usefulness of such analytical solution to the plume characterization will be investigated based on  $t_{inf}$  which is measurable in an interference test comprising an active and observation well.

In the following, we develop analytical model for the linear composite system shown in Figure 2.2. Region 1 has an active well that is producing/injecting at a constant rate. The active well is situated at distance  $a$  from  $x=0$  reference line. Region 2 is a region of altered properties (namely fluid viscosity and compressibility) which represent a leaked CO<sub>2</sub> plume in the above zone. Its left boundary is situated at  $x=0$  while the right boundary is at  $x= b$ . Region 3 has same rock and fluid properties as those of region 1. Note that since the reservoir thickness is small compared to its horizontal length, the vertical flow component can be neglected and the Dupuit assumption holds (Bear 1972). As a result, the pressure diffusivity in the reservoir is considered 2-D in the  $x$ - $y$  plane.



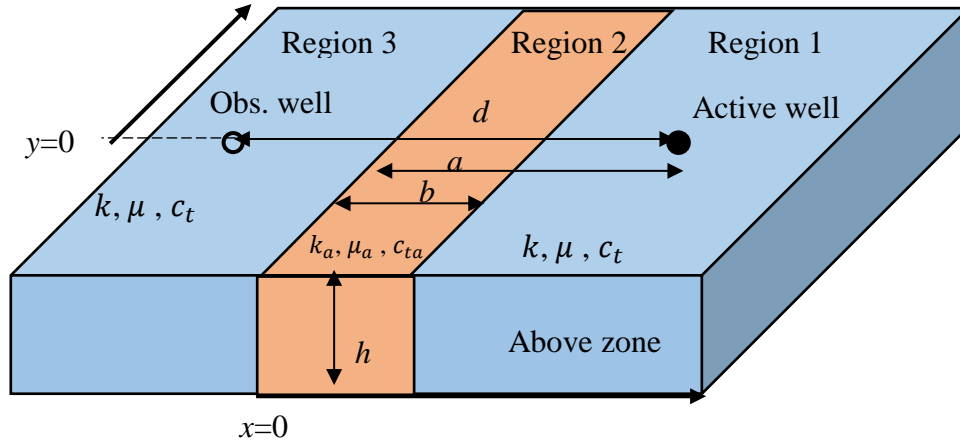


Figure 2.2. 3-D view of three-region linear composite system defined for development of analytical model for a leaked plume (region 2) in a hosting permeable zone overlying the injection zone (above-zone).

Governing equations and corresponding boundary conditions are set up separately for each of the three regions. The fluids in the reservoir and the leaked CO<sub>2</sub> plume are considered slightly compressible. This assumption is valid when CO<sub>2</sub> is under supercritical conditions (e.g. Azizi and Cinar 2013, Mathias et al. 2011, Mathias et al. 2009). If subcritical conditions are reached upon CO<sub>2</sub> leakage to shallow layers, the treatment of the CO<sub>2</sub> plume as a slightly compressible fluid is only valid if the pressure induced by the active well is no more than 10% of the initial pressure of the hosting zone (Spivey and Lee 2013). The governing diffusivity equations for regions 2.1 to 2.3 are given by equations 2.1 to 2.3 respectively (Bixel, Larkin, and K. 1963).

$$\frac{\partial^2 p_1}{\partial x^2} + \frac{\partial^2 p_1}{\partial y^2} + \frac{q\mu}{kh} \delta(x-a)\delta(y) = \frac{1}{\eta} \frac{\partial p_1}{\partial t} \quad (2.1)$$

$$\frac{\partial^2 p_2}{\partial x^2} + \frac{\partial^2 p_2}{\partial y^2} = \frac{1}{\eta_a} \frac{\partial p_2}{\partial t} \quad (2.2)$$

$$\frac{\partial^2 p_3}{\partial x^2} + \frac{\partial^2 p_3}{\partial y^2} = \frac{1}{\eta} \frac{\partial p_3}{\partial t} \quad (2.3)$$

where  $\delta$  is the Dirac delta function,  $q$  is volumetric injection/production rate,  $\mu$  is fluid viscosity, and  $k$ ,  $h$ , and  $\eta$  are above-zone permeability, thickness, and diffusivity coefficient respectively. The diffusivity coefficient,  $\eta$ , is defined as  $k/(\phi \mu c_t)$  where  $\phi$  and  $c_t$  are porosity and total compressibility respectively.  $p_1$ ,  $p_2$ , and  $p_3$  stand for pressure in regions 1, 2, and 3, respectively. The subscript  $a$  indicates the properties of the altered region i.e. region 2.

The initial and boundary conditions are defined for all regions which couple the governing equations for different regions. Partial differential equations (PDEs) 2.1 to 2.3 are 2<sup>nd</sup> order in space and 1<sup>st</sup> order in time here, so 1 initial condition and 4 boundary conditions for each region are required. Initial condition remains the same in all regions in that initially at time  $t=0$ , pressure throughout reservoir is stabilized at the same value of initial pressure  $p_i$ . Boundary conditions at external boundaries are also easier to handle using assumption of infinite acting reservoir in both  $x$  and  $y$  directions. This leaves defining boundary conditions at the interface of different regions. A pressure and flux continuity is assumed at interfaces which yields the following boundary conditions;

$$p_i = p_{i+1} \quad (2.4)$$

$$\frac{k_i A}{\mu_i} \frac{\partial p_i}{\partial x} = \frac{k_{i+1} A}{\mu_{i+1}} \frac{\partial p_{i+1}}{\partial x} \quad (2.5)$$

where  $i$  refers to the region on the left side of the interface.

### 2.3 Analytical Solution

The details of deriving the analytical solution for the governing equations (2.1) through (2.3) subject to boundary conditions (2.4) and (2.5) is given in the Appendix. The analytical solution is derived using combined Laplace and Fourier transforms which are respectively defined by:

$$\bar{p}_D(x, y, s) = \mathcal{L}\{p_D(x_D, y_D, t_D)\} = \int_0^\infty p_D(x_D, y_D, t'_D) e^{-st'_D} dt'_D \quad (2.6)$$

$$g''_{D3} - (\xi^2 + i\omega)g_{D3} = 0 \quad (2.7)$$

The analytical solution in terms of dimensionless pressure in Laplace and Fourier domain in regions (1) to (3) are given by:

$$\tilde{\bar{p}}_{D1} = \frac{e^{-A|a_D - x_D|} + \frac{e^{-A(a_D - 2b_D + x_D)}(-1 + e^{2Bb_D})(A - BM)(A + BM)}{-(A - BM)^2 + e^{2Bb_D}(A + BM)^2}}{2As} \quad (2.8)$$

$$\tilde{\bar{p}}_{D2} = \frac{e^{A(-a_D + b_D)}(BM \cosh(Bx_D) + A \sinh(Bx_D))}{(2ABMs \cosh(Bb_D) + (A^2 + B^2M^2)s \sinh(Bb_D))} \quad (2.9)$$

$$\tilde{\bar{p}}_{D3} = \frac{2Be^{Bb_D + A(-a_D + b_D + x_D)}M}{-(A - BM)^2 s + e^{2Bb_D}(A + BM)^2 s} \quad (2.10)$$

where

$$x_D = \frac{x}{d}, y_D = \frac{y}{d}, a_D = \frac{a}{d}, b_D = \frac{b}{d}, t_D = \frac{\eta t}{d^2}, p_{Di} = \frac{kh}{q\mu} \Delta p_i, A^2 = \omega^2 + s, B^2 = \omega^2 + \frac{C}{M}s \quad (2.11)$$

Also,  $M$  and  $C$  are the mobility ratio and storativity ratio respectively defined by:

$$M = \frac{(k/\mu)_a}{k/\mu}, C = \frac{c_{ta}}{c_i}.$$

Equations (2.8) to (2.10) are in Laplace-Fourier domain and should be converted into time and space domain. We use numerical algorithms of Fast Fourier Transform (Cooley and Tukey 1965) and Stehfest (Stehfest 1970) for Fourier and Laplace inversion respectively. From the analytical solution given by Equations (2.8) to (2.10), the dimensionless pressure is a function of 4 dimensionless groups: mobility ratio ( $M$ ), storativity ratio ( $C$ ), dimensionless plume size ( $b_D$ ), and dimensionless plume distance from the active well ( $a_D$ ). For a given observation location, ( $a_D - x_D$ ) is fixed and independent of relative location of the plume with respect to the observation well. Therefore, if  $b_D$  is fixed, the term ( $-a_D + b_D + x_D$ ) in equation (2.10) is fixed implying that the dimensionless pressure for a fixed observation well at region 3 depends only on  $b_D$ . In other words, changing the location of the plume while the plume size is fixed does not make any change to the

pressure at an observation well in region 3. An interference test in presence of two identical plumes located between the wells but at different distances from the wells will give identical pressure response. This observation confirms the reciprocity principle (Falade and Brigham 1979, Bruggeman 1972) i.e. switching the location of the active and observation wells results in identical pressure signature. More importantly, this observation suggests that there is a one-to-one relationship between the plume size (represented by  $b_D$ ) and the pressure change (represented by dimensionless pressure). This is very important because it allows the observation well to readily determine the plume size from pressure measurements in region 3.

## 2.4 Verification of Analytical Model

In this section, the analytical solution is verified by comparing with numerical simulation results. Numerical simulation is performed using a black-oil commercial numerical reservoir simulator (CMG-IMEX 2015). The above-zone model structure is a single layer 3-m thick brine aquifer (2D) with a slab of altered region representing the CO<sub>2</sub> plume which is introduced by assigning different PVT properties. For the base case problem considered here, the permeability and porosity of the above-zone are 50 mD and 0.2 respectively. Water viscosity is 1 cp and total compressibility is  $10^{-9}$ /Pa. The distance between the active well and the observation well is 400 m which is assigned to  $d$  for convenience. The plume length is  $b=150$  m and the distance from the far end of the plume to the active well is  $a=300$  m. In dimensionless terms:  $a_D=0.75$ ,  $b_D=0.375$ , and  $x_D=-0.25$ . Water is produced at a rate of  $10^{-4}$  m<sup>3</sup>/s.

It is important to obtain and vary  $M$  and  $C$  values over a realistic range. We obtain  $M$  and  $C$  by varying the pressure and temperature considering hydrostatic pressure gradient (0.433 psi/ft or 9.80 kPa/m) and temperature gradients of 0.02, 0.03 and 0.04 deg. °C/m. The pressure and

temperature at surface are set at 101.325 kPa and 25 °C respectively. The depth is varied over a range of 1000 to 5000 m the  $M$  and  $C$  values corresponding to which are shown in Figure 2.3.  $C$  is calculated based on compressibility calculated based on the following relationship:

$$c = -\frac{1}{V} \frac{dV}{dp} \quad (2.12)$$

The volume of CO<sub>2</sub> can be obtained by iteratively solving following Redlich-Kwong equation of state (Redlich and Kwong 1949);

$$V^3 - V^2 \left( \frac{RT}{p} \right) - V \left( \frac{RTb_m}{p} - \frac{a_m}{pT^{0.5}} + b_m^2 \right) - \left( \frac{a_m b_m}{pT^{0.5}} \right) = 0 \quad (2.13)$$

where  $R = 83.1447 \text{ bar cm}^3 \text{ mol}^{-1} \text{ K}^{-1}$ ;  $V$  is in  $\text{cm}^3/\text{mol}$ ;  $p$  is in bar;  $T$  is in K;  $b_m$  is in  $\text{cm}^3/\text{mol}$ ;  $a_m$  is in  $\text{bar cm}^6 \text{ K}^{0.5} \text{ mol}^{-2}$ .  $dV/dp$  is calculated by differentiating this equation with respect to  $p$ .

Viscosity calculations are based on Fanghour correlation (Fenghour 1998).

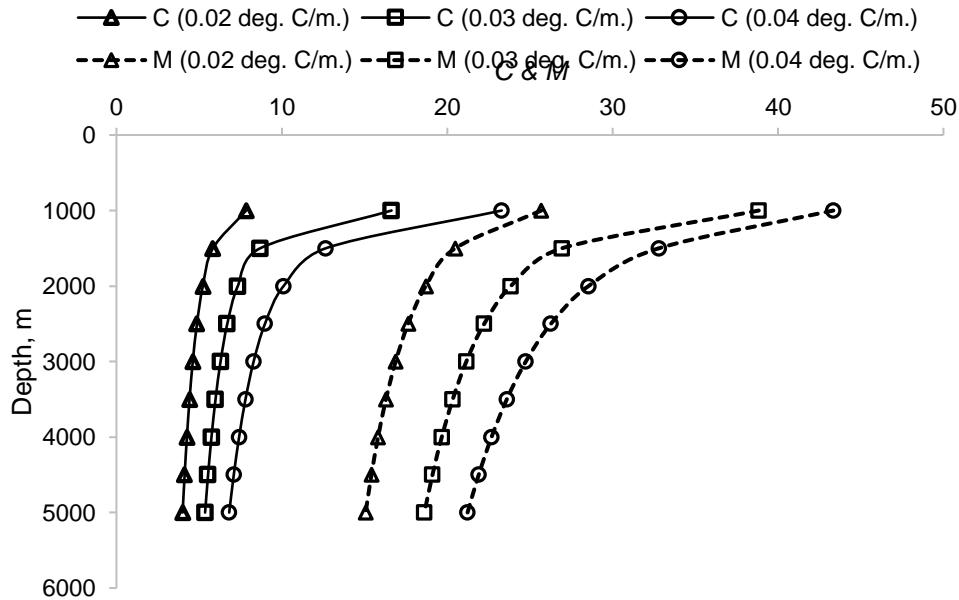


Figure 2.3. Variation of mobility ratio ( $M$ ) and storativity ratio ( $C$ ) versus depth for different geothermal gradients.

We use the analytical model using 4 combinations of  $(M, C)$  given by (15.07, 4.0), (21.23, 6.82), (25.69, 7.84), and (43.35, 23.29). Very good agreement between the numerical and analytical solutions is observed for all cases as shown in Figure 2.4. The analytical model can be used to illustrate the reciprocity principle which suggests that switching the locations of the active and observation wells and repeating the interference test should provide the same pressure response. For switched wells the new dimensionless parameters are:  $a_D=250/400=0.625$ ,  $b_D=150/400=0.375$ , and  $x_D=a_D-1=-0.375$ . For these parameters, the exact same results as those observed in Figure 2.4 are obtained. As explained at the end of Section 3, the analytical solution implies that the pressure at an observation well in region 3 depends only on the leak size and does not vary with changing the plume location with respect to the wells. This is both analytically and numerically investigated and confirmed. Changing the location of the plume while its size is constant ( $b_D=0.375$ ) does not change the pressure results presented in Figure 2.4.

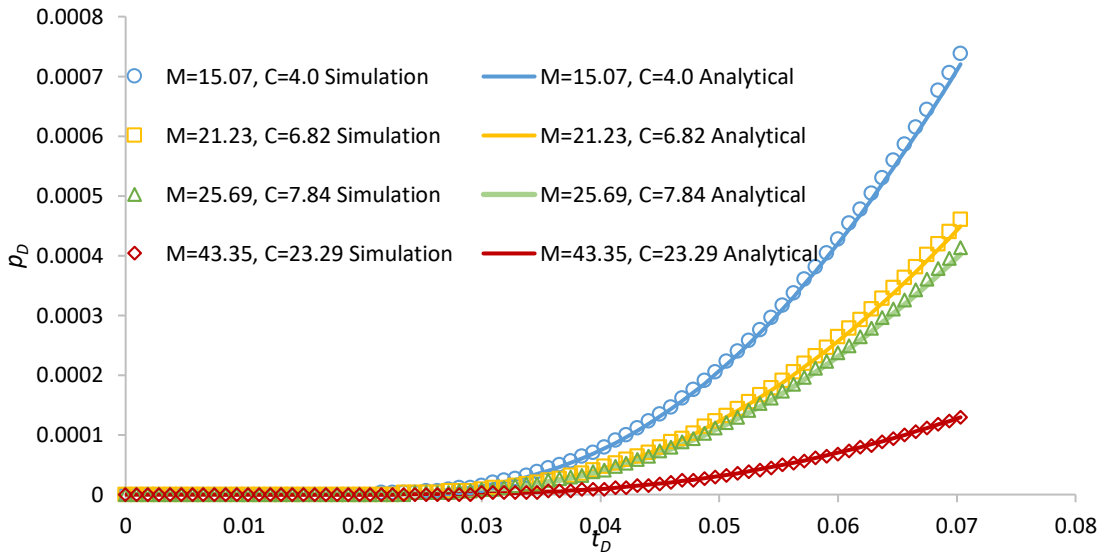


Figure 2.4. Comparison of analytical model with numerical simulation results for 4 combinations of  $M$  and  $C$  values.

The analytical solution can also be compared to a simplified analytical solution in absence of the plume. Considering identical rock and fluid properties for all the three regions, the linear composite analytical solution should reduce to the line-source infinite-acting solution (Theis 1935) on the  $x$ -axis ( $y=0$ ):

$$P_D = \frac{-1}{4\pi} Ei \left( \frac{-x_D^2}{4t_D} \right) \quad (2.14)$$

The dimensionless pressure is calculated for various  $x_D$  and  $t_D$  values and plotted in Figure 2.5 which shows an excellent agreement.

It is important to determine the ability of the analytical solution to provide information on the plume when the plume is not linearly shaped. In the next section we show that the influence time predicted by the three-region composite linear analytical model developed above is in close agreement with that obtained numerically regardless of the plume shape as long as the plume extent remains the same.

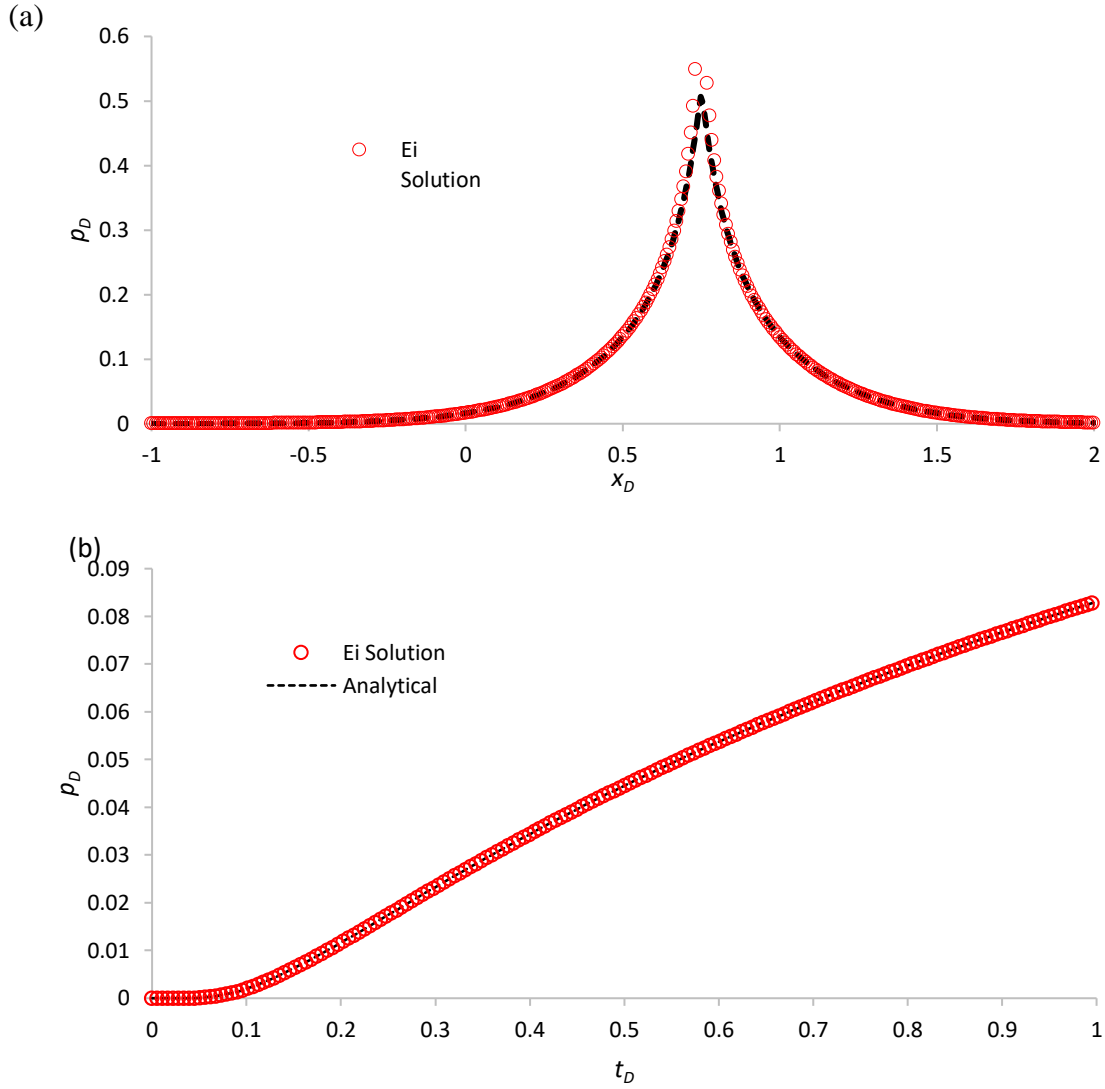


Figure 2.5. Comparison of the analytical solution with *Ei* (Theis 1935) solution results for a case with identical regions in terms of (a) dimensionless pressure versus dimensionless distance at dimensionless time,  $t_D=0.135$ , and (b) dimensionless pressure versus dimensionless time.

#### 2.4.1 Impact of plume shape on pressure response

We assess the impact of plume shape on the pressure behavior using a series of numerical simulations. Five different shapes are assigned to the plume (Figure 2.6). The base case configurations (presented in previous section) are exactly the same as those for the analytically modelled reservoir configuration. For other four cases, all other reservoir properties are exactly the same as the base case model with the only difference being shape of plume. While these cases



are different in shape, the plume boundaries (representing parameters  $a$  and  $b$ ) on the line connecting the two wells are the same for all the cases. Figure 2.7 shows the difference between the (dimensionless) pressure responses for these plume shapes considering  $M=15.07$  and  $C=4$  (corresponding to 5000-m depth). As expected, the pressure response for these different shapes is different.

It is important to find a common feature for these cases to enable gaining information from the analytical solution. The time when the pressure is felt at the observation well depends on the gauge resolution being deployed. For a given gauge resolution, the time at which the pressure is sensed at the observation well (referred to as pressure influence time,  $t_{inf}$ ) is measurable and therefore can be useful to characterizing the plume.

We investigate the usefulness of  $t_{inf}$  based on the numerical simulation results for different plume shapes. Considering 70 pa (0.01 psi) gauge resolution (which is available for today's quartz pressure sensors),  $t_{inf}$  is calculated analytically for various combinations of  $M$  and  $C$  values the results of which are given in Table 2.1. For each pair of  $M$  and  $C$ , the numerical  $t_{inf}$  is also calculated which is in close agreement with the analytically calculated  $t_{inf}$  obtained using equation (2.10) (maximum error is 0.9% observed for base case with  $M=15.07$  and  $C=4$ ). This shows the accuracy of the numerical results in predicting  $t_{inf}$  correctly.  $t_{inf}$  is calculated for four other plume shapes (given in Figure 2.6) which are reported in Table 2.1 for four combinations of  $M$  and  $C$ .  $t_{inf}$  for different plume shapes differs from the base case shape only by small error. The maximum error is 15% observed for case 4 with  $M=43.35$  and  $C=23.29$  and the average error is 5%. Given the one-to-one correspondence of the pressure and plume size,  $t_{inf}$  can be readily inverted using the analytical solution to obtain the plume size because  $t_{inf}$  values for different plume shapes with

identical plume extent (on the line connecting the active and observation wells) are practically the same.

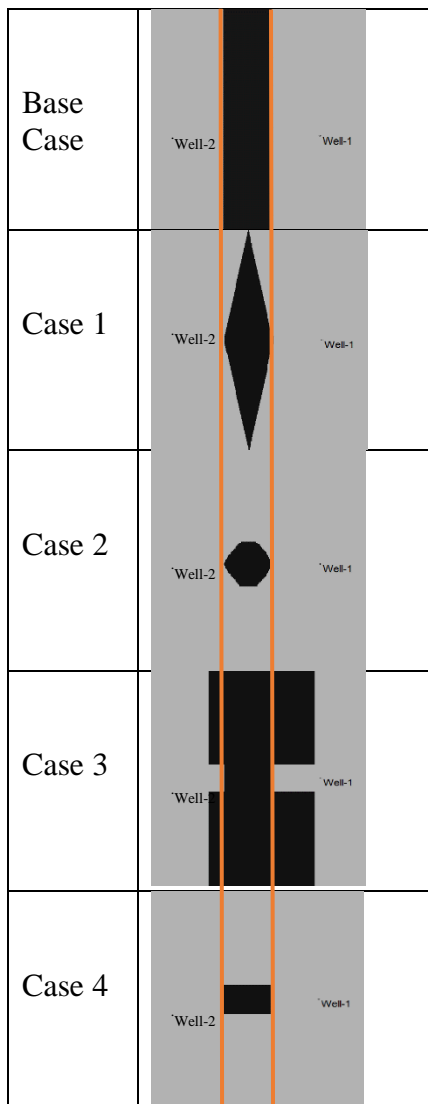


Figure 2.6. Plume shapes to investigate the effect of plume shape on pressure influence time

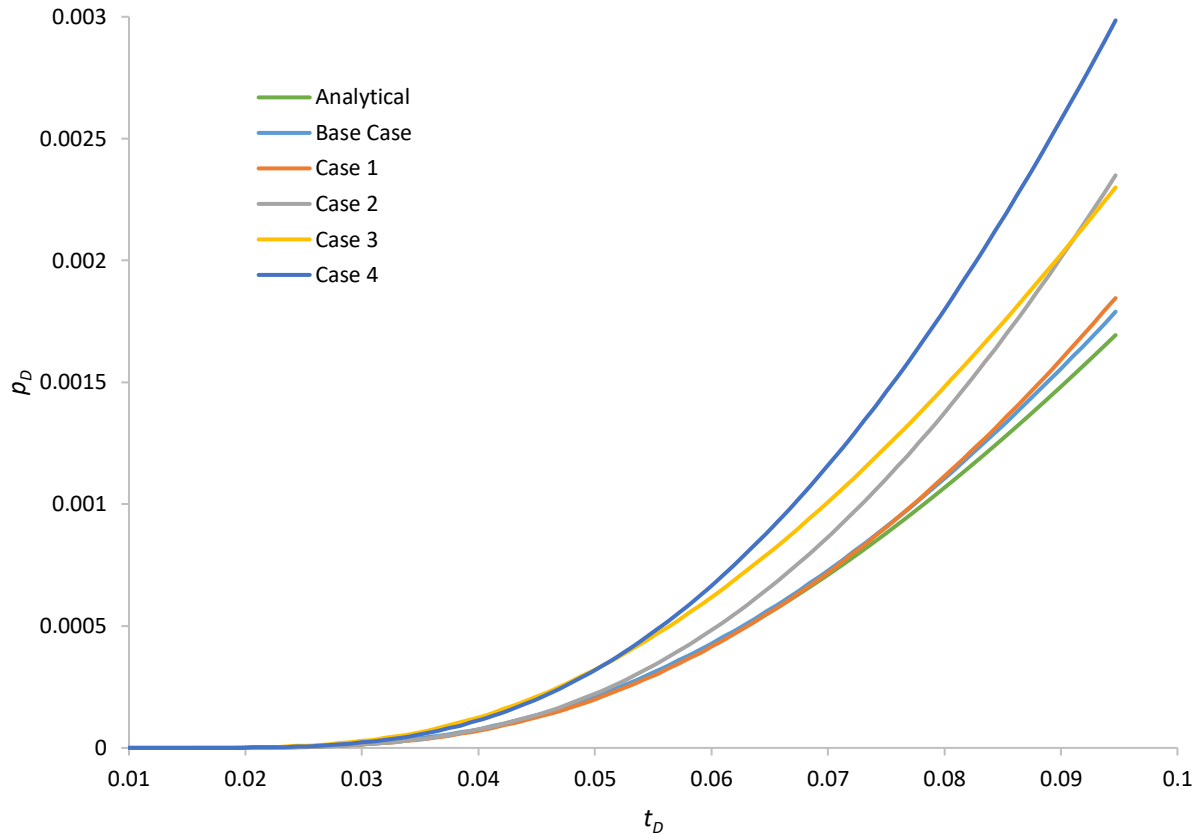


Figure 2.7. The pressure response at observation well ( $x_D=-0.25$ ) for various plume shapes for  $M=15.07$  and  $C=4$ . It suggests that the pressure influence time is identical (see Table 1) despite the difference between the pressure behavior for different plume shapes.

**Table 2.1.** Pressure influence time ( $t_{inf}$ ) at the observation well for a 0.01 psi (70 pa) gauge resolution considering different plume shapes.

$M$	$C$	Analytical $t_{inf}$ (hr)	Shape	Numerical $t_{inf}$ (hr)	Error%
43.35	23.29	11.9	Base Case	11.9	0.1
			Case 1	11.8	0.9
			Case 2	10.8	9.1
			Case 3	11.5	3.1
			Case 4	10.1	15.1
15.07	4	7.6	Base Case	7.6	0.9
			Case 1	7.7	0.7
			Case 2	7.6	0.9
			Case 3	6.8	11.4
			Case 4	6.9	9.1
21.23	6.82	8.6	Base Case	8.6	0.0
			Case 1	8.6	0.8
			Case 2	8.3	2.7
			Case 3	7.8	8.9
			Case 4	7.7	10.4
25.69	7.84	8.8	Base Case	8.8	0.0
			Case 1	8.8	0.6
			Case 2	8.5	3.2
			Case 3	7.9	9.5
			Case 4	7.8	11.4

## 2.5 Evaluation of Plume Size ( $b$ ) from $t_{inf}$

In practice, errors may be associated with measurement of pressure influence time ( $t_{inf}$ ) due to background noise and/or gauge metrology. Since determination of the plume extent from influence time is an inverse problem, small errors in reading  $t_{inf}$  may lead to large errors in plume size ( $b$ ) estimation. In the following, we use  $t_{inf}$  to estimate the plume size on the line connecting the pulse well to the observation wells (in dimensionless form represented by  $b_D$ ). In addition to  $b_D$ , the dimensionless pressure for a given dimensionless time and dimensionless distance in region 3 also depends on  $M$  and  $C$  (see Eq. (10)). For a given storage site conditions,  $M$  and  $C$  may be known

from other sources of data including well logs and cores. Therefore,  $b_D$  (or  $b$  dimensionally) is the only unknown to be determined from dimensionless  $t_{inf}$ . Here, we investigate the impact of errors in  $t_{inf}$  measurement on the plume size ( $b$ ) estimation. The  $t_{inf}$  is considered to vary within a normal distribution with mean value of 11.9 hr (or 0.067 in dimensionless terms) and variance of 0.3 hr (or 0.0017 in dimensionless terms which is 2.5% of the mean).  $M$  and  $C$  are 43.35 and 23.29 respectively. Monte Carlo simulations were ran to determine the distribution of  $b$  corresponding to this variation. The mean value of the plume size parameter,  $b$ , is found 151.9 m with a standard deviation of 20.0 m (13% of the mean).

## 2.6 Application for Plume Volume Estimation

For field applications,  $t_{inf}$  at a network of observation wells in response to injection/production at an active (pulse) well are required (Figure 2.1). Once obtained,  $t_{inf}$  from multiple observations wells can be inverted to obtain the plume volume on the line connecting each of the observation wells to the active well. In this section, we obtain and invert  $t_{inf}$  for multiple observation wells for a symmetric plume generated by numerical simulation. The generated plume is assumed to represent a plume caused by leakage.

### 2.6.1 Model set up

In this subsection, we explore the usefulness of  $t_{inf}$  to estimate the CO<sub>2</sub> plume volume in a homogeneous brine reservoir. CO<sub>2</sub> plume is generated by numerical simulation of CO<sub>2</sub> injection into 5-m thick aquifer. The initial reservoir pressure and temperature are 30 MPa and 110 °C respectively. Permeability and porosity are 36 mD and 0.18 respectively. The relative permeability for water is introduced using van Genuchten (1980) model and that of CO<sub>2</sub> gaseous phase is modelled using Corey (1954) model (see Table 2.2). The properties of this model are taken from

those given for a real CO<sub>2</sub> storage site model in the southeast United States (Haghighat et al. 2013, Petrusak et al. 2010, Koperna 2013). CO<sub>2</sub> injected for 45 days and followed by four years waiting period to allow for pressures in the reservoir to stabilize. After four years, an active (pulse) well is introduced at 147 m from the CO<sub>2</sub> injector. Water is injected at the active well at 300 m<sup>3</sup>/day through all layers. Pressures are observed at six observations wells co-linear to the CO<sub>2</sub> injector and active well at distances of 245, 280, 315, 350, 385, and 420 m from the pulse well. 70 Pa (0.01 psi) gauge resolution was used to determine the pressure influence time at each of the wells. Figure 2.8 shows a plan view of the system configuration. Three scenarios are simulated to arrive at different CO<sub>2</sub> plume distributions. Scenario 1 has zero irreducible water saturation ( $S_{wirr}=0$ ) and zero critical gas saturation ( $S_{gc}=0$ ). For scenario 2,  $S_{wirr}=0.3$  and  $S_{gc}=0$ . Scenario 3 considers  $S_{wirr}=0.3$  and  $S_{gc}=0.1$ . All simulations are performed using a numerical simulator, CMG-GEM (2015) compositional simulator. Figure 2.9 shows the cross-sectional view of the plumes for all three scenarios.

To translate the properties of the numerical simulation models to input of the analytical model, all the properties are evaluated at the start of water injection at the active well. Viscosity of aqueous and (gaseous) CO<sub>2</sub> phases are 0.05 Pa.s and 0.257 Pa.s respectively. The aqueous phase, CO<sub>2</sub> phase, and rock compressibilities are  $4.35 \times 10^{-7} \text{ Pa}^{-1}$ ,  $2.36 \times 10^{-5} \text{ Pa}^{-1}$ , and  $6.00 \times 10^{-7} \text{ Pa}^{-1}$  respectively. These properties correspond to 5.10 and 23.43 for the values of  $M$  and  $C$  to be used as an input into the analytical model. The analytical model uses  $b$  as the extent of pure gaseous CO<sub>2</sub> region on the line connecting the active and observation wells. In other words,  $b$  represents the gaseous CO<sub>2</sub> volume percentage on the active-observation connecting path. To obtain  $b$  from the reservoir simulation, the weighted block average saturation of gaseous CO<sub>2</sub> phase was taken along the line connecting the pulse and the observation wells. This was then multiplied by the total

length of that line to obtain  $b$ . The scenario with only irreducible water saturation had the lowest plume saturation, thus corresponding to the lowest  $b$  value.

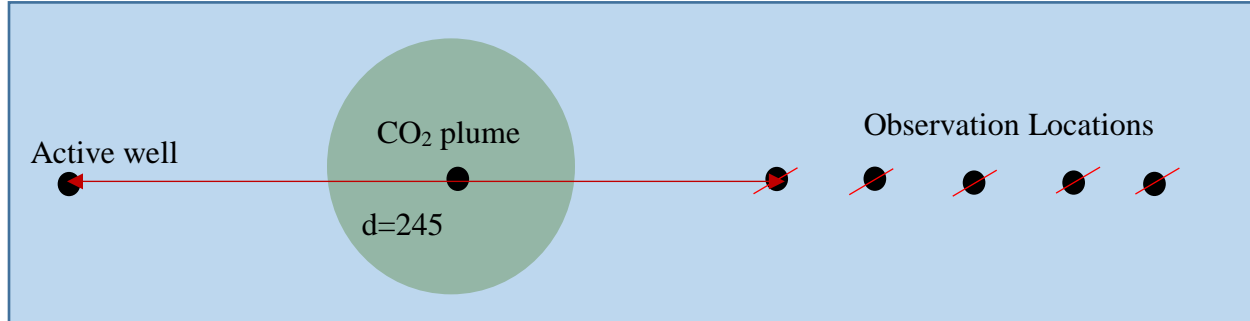
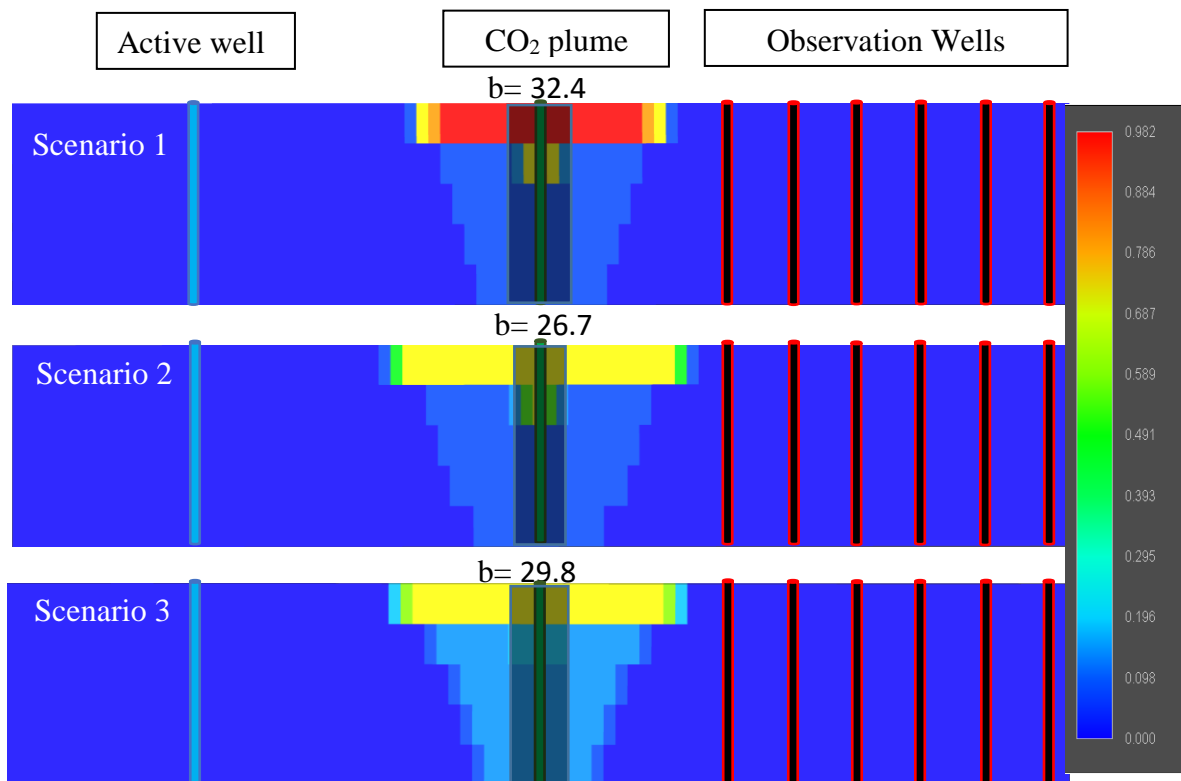


Figure 2.8. Plan view of model set up. Distance between neighboring observation points are constant at 35 m.



**Figure 2.9.** Plume shape and gas saturation for 3 simulated scenarios. The gas saturations are higher for scenario 3 due to the effects of critical gas saturation while scenario 1 has higher gas saturation in the top layer due to zero irreducible water saturation.  $b$  value is

Table 2.2. Relative permeability curves for the simulated cases

Aqueous phase relative permeability: van Genuchten (1980)	
$k_{ra} = \sqrt{S^*} \left( 1 - \left( 1 - [S^*]^{1/\lambda} \right)^\lambda \right)^2$	where: $S^* = \frac{S_a - S_{wirr}}{1 - S_{wirr}}$ , $\lambda=0.95$ ,
CO <sub>2</sub> gaseous phase relative permeability: Corey (1954)	
$k_{rg} = k_{rg}^0 \left( 1 - \hat{S} \right)^n \left( 1 - \hat{S}^2 \right)$	where: $\hat{S} = \frac{S_a - S_{wirr}}{1 - S_{wirr} - S_{gc}}$ , $k_{rg}^0 = 1$ , $n=2$

### 2.6.1 Forward and Inverse Modeling for $t_{inf}$ Values

In this subsection, the results of the numerical simulations are compared to those of the analytical model. The comparison is made in terms of both forward and inverse modeling. For forward modeling,  $b$  is assumed known (from field observations or synthetically from numerical simulation) and  $t_{inf}$  is to be calculated. For inverse calculation,  $b$  is to be evaluated from known  $t_{inf}$ . Practically, inversion of  $t_{inf}$  value available from field measurement (or synthetically obtained from numerical simulation) for calculation of  $b$  is of interest.

The results of forward calculations of  $t_{inf}$  values for the three scenarios are compared at different locations of observations wells (Table 2.3).  $t_{inf}$  values are directly available from the numerical simulation results considering 0.01 psi gauge resolution.  $b$  values obtained from the numerical simulations are used for forward calculation of  $t_{inf}$  using the analytical solution. As shown in Table 2.3, the error% between analytical and numerical  $t_{inf}$  values vary from 0.3-17.2% with an average of 3.7%. The highest error is observed for the scenario with irreducible water saturation and critical gas saturation. The errors do not show specific relationship with the distance from the plume.

In practice, one would measure  $t_{inf}$  values at the observation wells and invert them to calculate  $b$ . Here, we use  $t_{inf}$  values from numerical simulations as representatives of the  $t_{inf}$  values observed in



the field. Therefore,  $b$  values are calculated by inverting the  $t_{inf}$  values obtained from numerical simulations which are reported in Table 2.3. The inverted  $b$  values are compared to those directly available from the numerical simulations and the errors are given in Table 2.3. The errors in the inverted  $b$  value vary over a large range between 1.6 and 46.5 %. The  $b$  values inverted for different observation wells are averaged and reported in Table 2.4. The averaged inverted  $b$  values are in a better agreement with the actual  $b$  values with errors ranging between 5.7 to 24.0%. While large errors in calculation of  $b$  values for individual observation wells are possible, averaging the  $b$  values can reduce the errors making the inversion of  $t_{inf}$  an effective approach to estimate the extent of leakage plume.

The errors in inverting  $t_{inf}$  values are partially due to treatment of the leaked plume as a single-phase region. Further research is required to account for variation of the relative permeability of the phases within the plume. In addition, the effects of reservoir heterogeneities should be investigated in future work. While the homogenous system makes the plume symmetrical, having an irregular plume shape may impact the results. Also, for the simulation results reported above, the test has been performed after four years of wait time for pressures to stabilize and reduce the noise in the system. Methods for denoising the data to remove the effects of pressure perturbations caused by the leakage itself should be also investigated.

Table 2.3. Comparison of the numerical simulation and analytical model in terms of  $t_{inf}$  and  $b$  values.

Scenario	Distance from active well, m	Analytical $t_{inf}$ , hr	Numerical $t_{inf}$ , hr	$t_{inf}$ error%	True $b$ , m	Inverted $b$ , m	Inverted $b$ error%
No $S_{wirr}$ or $S_{gc}$	245	1.29	1.33	3.0	32.4	36.4	11.0
	280	1.63	1.67	1.9		35.0	7.4
	315	2.02	2.02	0.3		31.9	1.6
	350	2.45	2.40	1.9		29.0	11.7
	385	2.91	2.80	3.7		25.2	28.6
	420	3.41	3.25	5.0		22.7	42.7
With $S_{wirr}$	245	1.24	1.28	3.6	26.7	31.3	14.7
	280	1.58	1.63	3.7		32.1	16.8
	315	1.95	2.00	2.5		30.7	13.0
	350	2.37	2.38	0.7		27.9	4.3
	385	2.82	2.80	0.7		25.2	6.0
	420	3.32	3.25	2.2		22.7	17.6
With $S_{wirr}$ and $S_{gc}$	245	1.27	1.53	17.2	29.8	55.7	46.5
	280	1.61	1.80	10.6		46.6	36.1
	315	1.99	2.12	5.9		39.8	25.1
	350	2.41	2.48	2.9		35.1	15.1
	385	2.87	2.88	0.4		30.5	2.3
	420	3.37	3.33	1.1		27.6	8.0

Table 2.4. By taking the average values of the inverse  $b$  amongst all of the observation wells, lower errors can be obtained.

Scenario	True $b$ value	Average inverted $b$ value	Error%
No $S_{wirr}$ or $S_{gc}$	32.4	30.0	7.3
With $S_{wirr}$	26.7	28.3	5.7
With $S_{wirr}$ and $S_{gc}$	29.8	39.2	24.0

## 2.7 Conclusions

Leakage of CO<sub>2</sub> from a targeted geological storage formation may have adverse environmental impact. Pressure interference testing in an (above-zone) aquifer overlying the injection zone separated by a confining layer can be useful to detect and characterize a leaked plume. In this paper, we presented a method to use the pressure influence time ( $t_{inf}$ ) from interference test to determine the plume size. We presented a conceptual model where the above-zone containing the leaked plume is represented by a 3-region composite linear system. The governing PDE diffusivity equations and corresponding boundary conditions were written for these three regions and an analytical solution was obtained. The analytical solution is verified through comparison to numerical simulation results for various mobility and storativity values of the leaked plume and very good agreement was observed. The analytical solution for dimensionless pressure in region 3 reveals that the pressure is independent of the plume location and depends only on the size of the plume (represented by  $b$ ).

One important feature which can be analytically determined while being practically measurable is the pressure influence time ( $t_{inf}$ ).  $t_{inf}$  is the time at which the pressure change at the observation well attains the gauge resolution. Through comparison of the analytically calculated  $t_{inf}$  with that evaluated using numerical simulations for different plume shapes, we showed that  $t_{inf}$  may be considered independent of the plume shape and only depending on the plume size on the line connecting the active and observation wells ( $b$ ). As a result,  $t_{inf}$  should be readily invertible for calculation of plume size ( $b$ ). We showed that varying  $t_{inf}$  with 2.5% variance results in leaked plume size calculation with 13% variance.

As a field application example,  $t_{inf}$  values from six observation wells in response to injection at an active (pulse) well were inverted to obtain the CO<sub>2</sub> plume volume percentage ( $b$ ). Three different CO<sub>2</sub> plumes were modelled considering three sets of relative permeability end points to achieve different  $b$  values. We showed that while large errors in calculation of  $b$  from individual observation wells may be encountered, averaging the  $b$  values (obtained from multiple observation wells) can reduce the errors (to 5.7 – 24.0%) making the inversion of  $t_{inf}$  an effective approach to estimate the leaked CO<sub>2</sub> volume.

## **Chapter 3: CO<sub>2</sub> Plume Characterization Using Pressure Arrival Time**

### **3.1 Introduction**

CO<sub>2</sub> geological storage is a method to cut CO<sub>2</sub> atmospheric emissions as a means to mitigate climate change (IPCC 2005). The special distribution of injected CO<sub>2</sub> has important implications for the safety and liability of the CO<sub>2</sub> storage projects (Birkholzer and Zhou 2009, van der Meer and Yavuz 2009). It is required to determine how the injected CO<sub>2</sub> is distributed in the reservoir. Such determination will help the operator to optimize the CO<sub>2</sub> injection to avoid any unwanted CO<sub>2</sub> exposure. For example, CO<sub>2</sub> may reach a region which is densely drilled with potential leakage pathways which is to be avoided. It is also important to minimize the area exposed to CO<sub>2</sub> to minimize the risk of leakage. Undesirable impact of CO<sub>2</sub> migration from the injection zone include escape of CO<sub>2</sub> toward the surface and contamination of shallow potable aquifers by: (1) CO<sub>2</sub> intrusion resulting in dissolution and desorption of potentially toxic metals from minerals by acidic CO<sub>2</sub>-charged fluids, and (2) migration of deep formation brine which may contain high concentrations of metals and radionuclides (Kampman, Bickle, Wigley, et al. 2014, Kampman, Bickle, Maskell, et al. 2014). Potential leakage pathways include old abandoned wells which may not be properly plugged, currently active wells intersecting the injection zone, faults and fractures that may dilate due to the overpressure caused by injection, and local pathways in the low-permeability caprock. Failure effects may be manifested as: (a) Geological plumes or expanding formations of CO<sub>2</sub> gaseous fluid, (b) Uncontrollable pressure gradients that drive leakage or seepage of plumes, (c) Failure of bounding hydraulic seals for a depleted oil or gas reservoir slated for use as a CO<sub>2</sub> injection zone, (Rohmer and Bouc 2010, Zhang and Bachu 2011)

The purpose of this paper is to study how pressure arrival times from pressure interference tests can be used to characterize CO<sub>2</sub> plume in a target reservoir. For a known CO<sub>2</sub> plume, a pressure

pulse is induced at an active well, and pressure interference signals are monitored at several observation wells located inside and outside the plume. The arrival times are used to infer the saturation and extent of the CO<sub>2</sub> plume within the interference region.

Multiple-well tests (interference and pulse tests) are used to establish communication between wells and determine the interwell reservoir properties. In interference tests, reservoir properties including storativity,  $\phi h c_t$ , transmissivity,  $kh/\mu$ , and size of the reservoir are determined by measurements of well flow rate and well pressure (Kamal 1983). A pressure disturbance is applied to the reservoir through an active well by changing the flow rate. Effects are monitored at observation well(s) located at some distance from the active well. Pressure behavior vs time at the observation well induced by the active well can be interpreted for the reservoir properties. We introduce a method to use multi-well test that can determine the average gas saturation between the active and observation wells.

There are several techniques that have been developed in the past decade to monitor and characterize the extent of the CO<sub>2</sub> plume which includes 4D seismic data, electrical resistance tomography, seafloor-based acoustic tomography, and use of pH sensors (Alfi et al. 2015, Carrigan et al. 2013, Shitashima, Maeda, and Ohsumi 2013). Major disadvantages of these techniques include (i) cost ineffectiveness; (ii) inaccurate gas saturation evaluation; (iii) difficulty in deployment; and (iv) requiring long period of time to fully characterize plume behavior. Due to these drawbacks, albeit a relatively new concept, pressure transient analysis have been looked into as a strong alternative to CO<sub>2</sub> plume characterization. (Hosseini and Alfi 2016, Shakiba and Hosseini 2016, Sun et al. 2016). The method used in most recent literature to characterize CO<sub>2</sub> plume are regular and harmonic pulse testing. Pulse testing is monitoring the pressure responses of an observation well generated by a series of flow rate changes (pulses) at an active well.

(Johnson, Greenkorn, and Woods 1966) Harmonic pulse testing is a technique in which injection or production rate is varied in a periodic way. (Kuo 1972, Fokker, Renner, and Verga 2012) The pressure response in both the pulsing well and observation wells can be analyzed in the frequency domain to evaluate reservoir properties. We introduce a unique method by inducing a single pulse at the active well and utilizing the arrival time at the observation well to characterize the CO<sub>2</sub> plume. The advantages of well testing method over other monitoring methods include (i) simplicity; (ii) readiness to implement in the field; (iii) minimal time constrained by arrival time; and (iv) no new equipment necessary.

In departure from the work that has been recently done on using pressure to characterize the CO<sub>2</sub> plume, we use the pressure arrival time for such characterization. The pressure arrival time is a unique property that can be easily evaluated for a given constant rate pressure response at an observation well. The proposed method in this paper is to use the pressure arrival time at an interference well to evaluate the volume of CO<sub>2</sub> plume for any given time in a given direction. For doing this, at a given time at which the CO<sub>2</sub> plume extent is required, we induce a rate change at the injection (active) well and observe the arrival time of the pressure corresponding to that rate change. By utilizing the arrival time, we are able to characterize the CO<sub>2</sub> plume by determining the average CO<sub>2</sub>-rich gas saturation on the line connecting the two wells.

First, pressure arrival times are calculated by utilizing an analytical expression to compute multiphase diffusivity coefficients. The analytical arrival time was then compared to the numerical arrival time. There was a strong agreement between the analytical and numerical solutions. This strong agreement of arrival times allowed us to utilize the idea to inverse the pressure arrival time corresponding to an observation well to characterize a CO<sub>2</sub> plume by determining its average gas saturation between an active well and observation well. Results shows that average gas saturation

between an active well and observation well can be estimated accurately by using the pressure arrival times. Results from the study also indicate that by making use of the arrival times, defining geometrical boundaries and the extent of CO<sub>2</sub> plume is possible in homogenous and heterogeneous reservoirs.

### 3.2 Methodology

For radial flow in a single-phase system, the pressure arrival time,  $t_{arrival}$ , corresponds to the time at which the pressure derivative with respect to time is maximum in response to a constant rate production/injection (Lee, 1984). In other words, the pressure arrival time is the time at which the pressure change is maximum in response to an impulse rate injection/production. The radius from the wellbore corresponding to a given arrival time is referred to as radius of investigation (Kuchuk 2009). For single phase system with radial flow, the arrival time is given by:

$$r_{invs}^2 = 4\eta t_{arrival} \quad (3.1)$$

where  $\eta$  is the single-phase diffusivity coefficient and given by  $\eta = \frac{k}{\phi\mu c_t}$ .  $k$ ,  $\phi$ ,  $\mu$ , and  $c_t$  are permeability, porosity, viscosity, and total compressibility respectively.

Complications arise when there are two phases present. An analytical model to characterize a mixed phase diffusivity coefficient,  $D$ , in a CO<sub>2</sub>-brine-system is used for this study. (Hu et al. 2015b) The equation modified to include the effects of rock compressibility is given by

$$D = \left(\frac{k}{\phi}\right) \left[ \frac{\frac{k_{rw}}{\mu_w} \rho_w + \frac{k_{rg}}{\mu_g} \rho_g}{(S_w c_w + S_g c_g + c_r)(S_w \rho_w + S_g \rho_g)} \right] \quad (3.2)$$



where  $k_r, \rho, \mu, S, c$  represent the relative permeability, density, viscosity, saturation and compressibility respectively. The subscripts  $w$  and  $g$  represent water and gas phase.  $k$  is the permeability and  $\phi$  is the porosity. The approach to use the arrival time to estimate the average gas phase saturation will be useful to determine the average CO<sub>2</sub> saturation between an active well and observation well. First, we determine what permeability value should be used for the mixed CO<sub>2</sub>-brine diffusivity equation. This is especially important for cases of anisotropy and heterogeneity.

To determine the permeability for cases involving anisotropy, the numerical simulation was performed with single-phase water, with the permeability set at different values in the  $x$  and  $y$  direction to determine which permeability should be utilized for cases of anisotropy. Two observation wells were placed at equidistant locations relative to the active well. One observation well was located in the  $y$ -direction from the active well, and the other observation well was located in the  $x$ -direction from the active well. From eqn. (3.1), the permeability was calculated. It was found that the observation well placed horizontally corresponded to  $k = k_x$  and the well placed vertically corresponded to  $k = k_y$ . This led us to set  $k = k_x$  for cases with anisotropy since our observation wells were spaced in the  $x$ -direction with respect to the active well.

For cases of heterogeneity, before gas is introduced into the system, a water baseline was used to determine the average permeability for implementation into the mixed CO<sub>2</sub>-brine diffusivity equation. Water is injected for a short period of time. Arrival time is taken at each observation well and then utilized to determine the average permeability by using eqn. (3.1).

To invert the arrival time to determine the average gas saturation between active and observation wells, we have to ensure that the arrival times are in agreement analytically and numerically. If the arrival times calculated are not in agreement or are with high error with one another, then using

the method of inversion of arrival times to determine average gas saturation may prove to be impractical.

The definite integral for arrival time, eqn. (3.3), was converted to a Riemann Sum, eqn. (3.4), to directly calculate the arrival time based on results of the numerical simulation. Mixed phased diffusivity,  $D$ , was calculated for each grid block in the numerical simulator to be input into the Riemann sum.

$$\sqrt{t_{arrival}} = \frac{1}{2} \int_{r_1}^{r_2} \frac{dr}{\sqrt{D(r)}} \quad (3.3)$$

$$\sqrt{t_{arrival}} = \frac{1}{2} \sum_{i=1}^n \frac{1}{\sqrt{D}} \Delta r_i \quad (3.4)$$

Where the distance between the active well and observation well, varies from  $r_1$  to  $r_2$ , where  $r$  is the gas propagation path, and  $\Delta r_i$  is the size of each grid block.

For the case of the multilayer system, the value of the mixed-phase diffusivity coefficient,  $D$ , was obtained by averaging gas saturations through all layers at a given distance. Arrival times given by eqn. (3.4) were compared to arrival times obtained from numerical simulations. The numerical and arrival times are in strong agreement which is discussed in the results section. This strong agreement between the analytical and arrival time leads us to utilize the idea of taking the arrival time obtained by pressure interference test to estimate the average gas saturation between active and observations wells.

### 3.3 Cases for Numerical Model

The objective is to model a wide variety of CO<sub>2</sub> plumes which vary in shape and saturation in a fresh water aquifer in single layer and multi-layer conditions. Varying permeability alters the shape

while the implementation of irreducible water saturation,  $S_{wirr}$ , changes the overall saturation of the CO<sub>2</sub> plume.

The model was built by utilizing the CMG-GEM compositional simulator (CMG-GEM 2013). For each of the two systems, six different cases were considered, including the base case.

Base Case comprises a homogenous and isotropic reservoir with no irreducible water saturation ( $S_{wirr}=0$ ).

- Case 1 varies from the base case by adding 30% irreducible water saturation ( $S_{wirr} = 30\%$ ).
- Case 2 varies from the base case by including anisotropy while keeping irreducible water saturation at zero ( $S_{wirr}= 0$ ). Permeability in the x-direction, was two times greater than permeability in the y-direction.
- Case 3 adds both 30% irreducible water saturation and anisotropy (as described in case 1).
- Case 4 considers a complete heterogeneous system. Permeability was not spatially correlated but was randomly sampled from a log-normal distribution of permeability with mean equal to 36 mD and range from .54 to 1265 mD. The distribution can be seen in figure (3.1).
- Case 5 implemented a complete heterogeneous system as described in case 4 along with  $S_{wirr}=30\%$ .

The 6 cases were applied to both the single layer and multilayer systems, thereby making up a total of twelve different simulation scenarios.

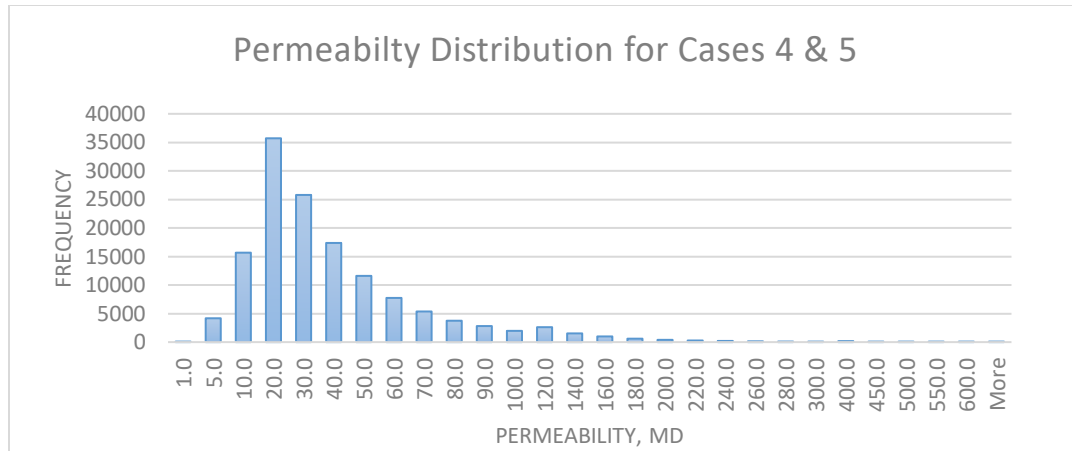


Figure 3.1. Permeability randomly sampled from log-normal distribution of range .54 to 1265 mD and average of 36 mD.

### 3.3.1 Description of numerical model

The reservoir area was chosen to be 1100 miles<sup>2</sup>. The large area was chosen to ensure that the behavior was that of an infinitely acting reservoir. The reservoir area was discretized into 141 x 141 cells. The thickness was 1 meter for the single layer, and 7 meters for the multi-layer. The multi-layer system consists of 7 layers with each layer being 1 meter thick. The active well was located at the cell with  $x$  and  $y$  indices of  $n_x=71$  and  $n_y=71$ . Grid blocks that enclose the CO<sub>2</sub> plume and observation wells were refined to have cell sizes of 1.4x1.4 meters for the single layer system. Grid blocks that enclose the CO<sub>2</sub> plume and observation wells were refined to have cell sizes of 7 x 7 meters for the multi-layer system.

For the single layer system, CO<sub>2</sub> plume was created by injecting CO<sub>2</sub> gas at  $2.0 \times 10^4$  m<sup>3</sup> /day through an active well for 45 days. After a waiting period of four years, the active well pulses water at 50 m<sup>3</sup> /day. The four year waiting period was selected to minimize noise in the system and allow the plume to stabilize.

Pressures were monitored at six selected observation wells located co-linear with the injection well. The closest observation well was located at 91.5 and 94.3 meters from the active well for the single layer and multi-layer systems respectively. The remaining observation wells were spaced 35 meters concurrently from each other for both systems.

The multilayer system was set up in similar fashion as the single layer system, but the CO<sub>2</sub> gas was injected at higher rates of  $1.4 \times 10^5$  m<sup>3</sup>/day for 45 days through all seven layers. Analogous to the single-layer system, there was a four-year waiting period. Pressure observations were made at the middle layer (layer 4). The change in pressure was found to be independent of the layer that was monitored when the distance between active well and observation well is much greater than the thickness of the reservoir.

Figure 3.2 shows the model set-up for both single and multi-layer systems. Figure 3.3 shows the plumes obtained from the numerical simulator for both systems. The single layer has a plan view, and the multi-layer system shows a three-dimensional view of each case.

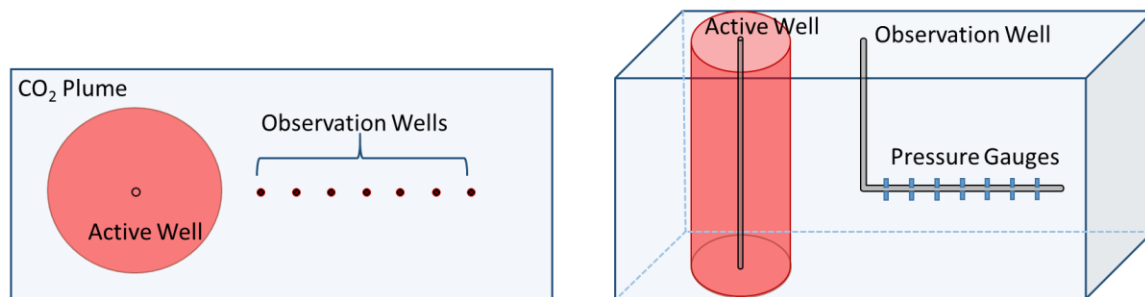


Figure 3.2. Shows the model in plan view and 3-deimentional view

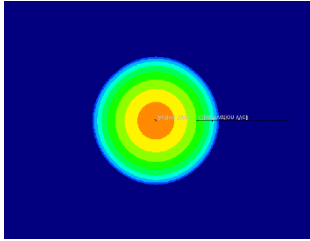
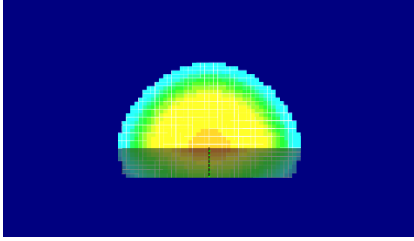
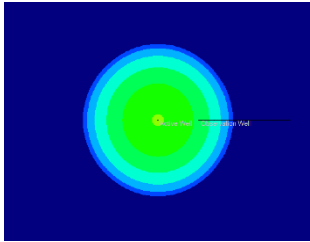
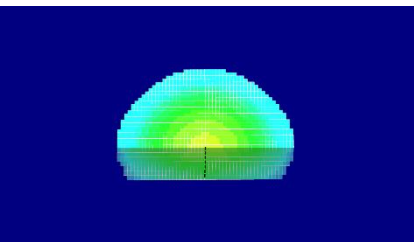
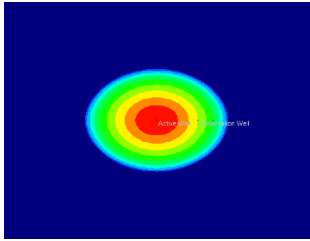
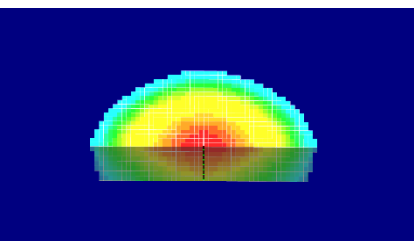
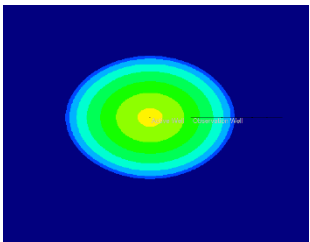
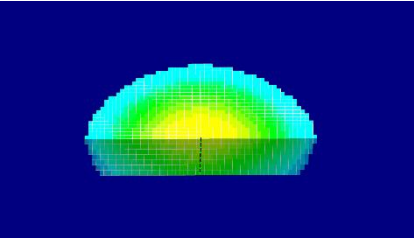
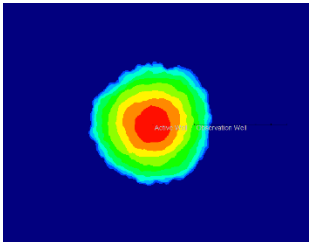
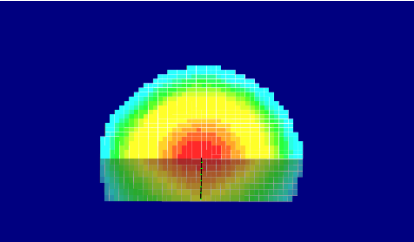
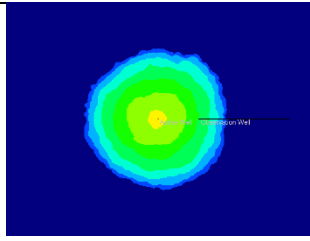
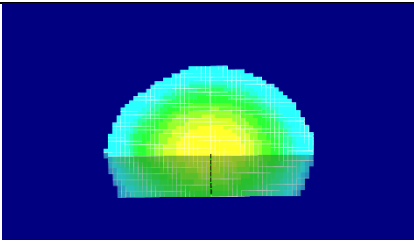
	Plan View	Three-Dimensional View
Base Case		
Case 1 $S_{wirr} = 30\%$		
Case 2 Anisotropy		
Case 3 Anisotropy, $S_{wirr} = 30\%$		
Case 4 Heterogeneity		
Case 5 Heterogeneity $S_{wirr} = 30\%$		

Figure 3.3. Shows the plume shape for all cases.

### 3.3.2 Reservoir Properties

The initial reservoir pressure was 30000 kPa at 2890-m depth (top depth). The initial reservoir temperature was 110 C°. The permeability was 36 mD for both homogenous and isotropic cases. For cases of anisotropy,  $k_x = 36\text{mD}$  and  $k_y = 18\text{ mD}$ . For cases of heterogeneity permeability was equal in all directions.

Fluid properties of CO<sub>2</sub> and water were created by using CMG WINPROP (CMG-GEM, 2013). Average fluid properties were read from the simulation but in the field, fluid properties can be obtained through various methods such as downhole fluid sampling. Relative permeability and capillary pressure were implemented into the numerical model by using well-known methods. The relative permeability of the aqueous phase were determined by the van Genuchten (1980) model using  $\lambda=0.95$  (see Table 3.1). Relative permeability of the CO<sub>2</sub> rich phase was determined using the model by Corey (1954), using  $n=2$ ,  $S_{gc}=0$ , and  $k_{rg}^0=1$  (see Table 3.1). For capillary pressure, the van Genuchten (1980) formulation as shown in Table 3.1 was used, with  $P_0=100\text{ kPa}$  and  $m=0.8$ . High capillary entry pressure,  $P_0$ , was used to capture a more accurate depiction of the CO<sub>2</sub> plume that is present in all layers. If capillary entry pressure is not included or too low, due to the buoyancy nature of gaseous CO<sub>2</sub>, the majority of the gas will rise to the top most layer while leaving trace amount of gas in the subsequent layers, thus giving an inaccurate representation of the gas plume.

Table 3.1. Drainage relative permeability and capillary pressure curves equations.

Aqueous phase relative permeability: van Genuchten (1980)	
$k_{ra} = \sqrt{S^*} \left( 1 - \left( 1 - [S^*]^{1/\lambda} \right)^\lambda \right)^2$	where: $S^* = \frac{S_a - S_{wirr}}{1 - S_{wirr}}$
CO <sub>2</sub> -rich phase relative permeability: Corey (1954)	
$k_{rg} = k_{rg}^0 \left( 1 - \hat{S} \right)^n \left( 1 - \hat{S}^2 \right)$	where: $\hat{S} = \frac{S_a - S_{wirr}}{1 - S_{wirr} - S_{gc}}$
Capillary pressure: van Genuchten (1980)	
$P_c = -P_0 \left( [S^*]^{-1/m} - 1 \right)^{1-m}$	where: $S^* = \frac{S_a - S_{wirr}}{1 - S_{wirr}}$

### 3.4 Determination of Average Gas Saturation

The main parameter of interest in this study is the average saturation. By using the arrival time from the numerical simulations, the value of  $r/\sqrt{D}$  was obtained from eqn. (3.3). By setting  $r$  to be the distance from the active well to the observation well, the two-phase diffusivity coefficient obtained can be considered as the average two-phase diffusivity coefficient,  $\bar{D}$ , between the two wells. Average saturation of gas,  $\bar{S}_g$ , was determined by using  $\bar{D}$ . This quantity can be obtained from the mixed phase diffusivity curve by plotting  $D$  versus  $S_g$ . Average saturation of gas can also be obtained by using a simple solver tool. It should be noted that there is non-uniqueness in the solution for the 2-phase diffusivity, but for the lower gas saturation difference when comparing the analytical and numerical solution, there was consistency in all cases using the lower limit of the two solutions to determine the analytical average gas saturation. An example graph of the mixed phase diffusivity coefficient vs saturation of gas is provided in figure (3.4). The example shown below illustrates how by using arrival time, average gas saturation can be obtained.



$t_{arrival} = 0.38 \text{ days}$  (Read from observation well)

$r = 94.3 \text{ meters}$

$$2 * \sqrt{.3799 * 86400} = \frac{94.3}{\sqrt{\bar{D}}} \Rightarrow \bar{D} = .068, \Rightarrow \bar{S} = .24$$

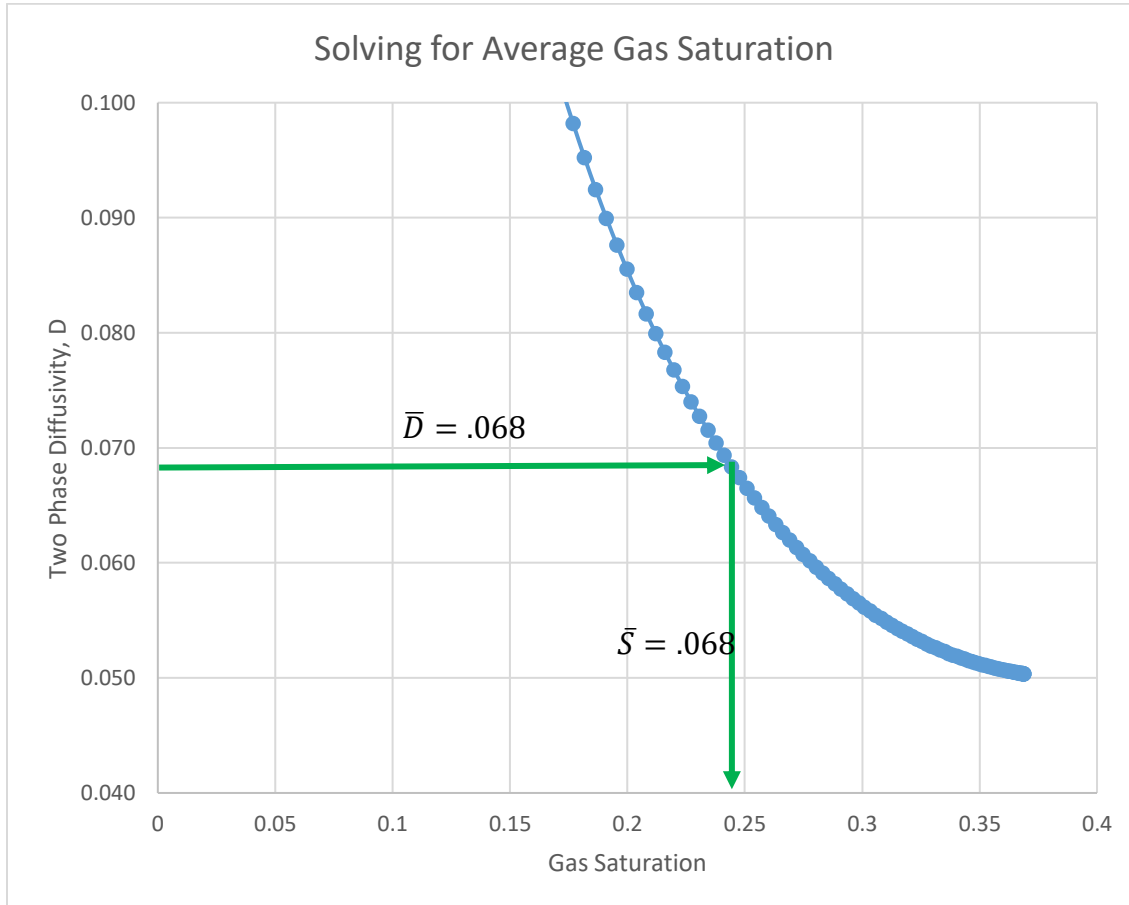


Figure 3.4. An example of the method to obtain average gas saturation. First, run pressure interference test to obtain an arrival time from the observation well. Then calculate the average mixed phase diffusivity coefficient,  $\bar{D}$ . Using equation 3.2, make a graph of two phase diffusivity versus gas saturation. Lastly, read the average gas saturation,  $\bar{S}_g$ , by using the average diffusivity coefficient. Instead of using the graphing method, a solver tool can be used.

### 3.5 Results

Arrival times were accurately determined by using the analytical solution for two-phased diffusivity, eqn. (3.2) and the line integral evaluation, eqn. (3.3). Tables (3.2) and (3.3) show percent error in calculations for arrival time for the single and multi-layer systems respectively. There is strong agreement between calculated arrival time and the arrival time obtained from the numerical simulator.

This strong agreement allows for the inversion of arrival time to accurately estimate average gas saturation. Although errors in calculated arrival times are low, it does not necessarily mean that errors in calculated average gas saturation are low. Variables such as grid refinement limitations, averaged reservoir properties, application of the inversion method, and misreading of pressure arrival times from pressure diagnostic plots can cause errors in the system. Tables 3.4 and 3.5 display numerical and analytical average gas saturations between an active well and observation well along with errors in calculated average gas saturations for the single layer and multilayer systems respectively. Although errors in calculated arrival times appear to be high (the highest error being 24%), the errors do not translate into large differences in average gas saturations. For example, for the case of 24% error in arrival time, the difference in gas saturation was only 6%. For all the cases studied, the average error in arrival times was about 10.5 %, whereas the average difference in all of the average gas saturations was only 2.1%.

Furthermore, with proper set up, calculated arrival times can also be used to solve for the plume boundary or how far the plume has migrated from the active well. Figure (3.5) shows the relation between arrival time versus distance, as well as gas saturation versus distance. The plume boundary location is defined where gas saturation is zero. The change in slope of the arrival time

provides a good estimate of the boundary location. This study is restricted to an idealized situation, because the observation wells were placed horizontally relative to one another. In the field, this may not be the case. Nevertheless, the results obtained are encouraging because if the CO<sub>2</sub> storage operation is large enough and is designed for a homogenous or heterogeneous reservoir, we can get a good sense of the extent of the plume, without having to take fluid samples from wells. The reason is that the plume is relatively symmetrical in heterogeneous and homogeneous cases. When anisotropy is present, this may not be a good method of analysis.

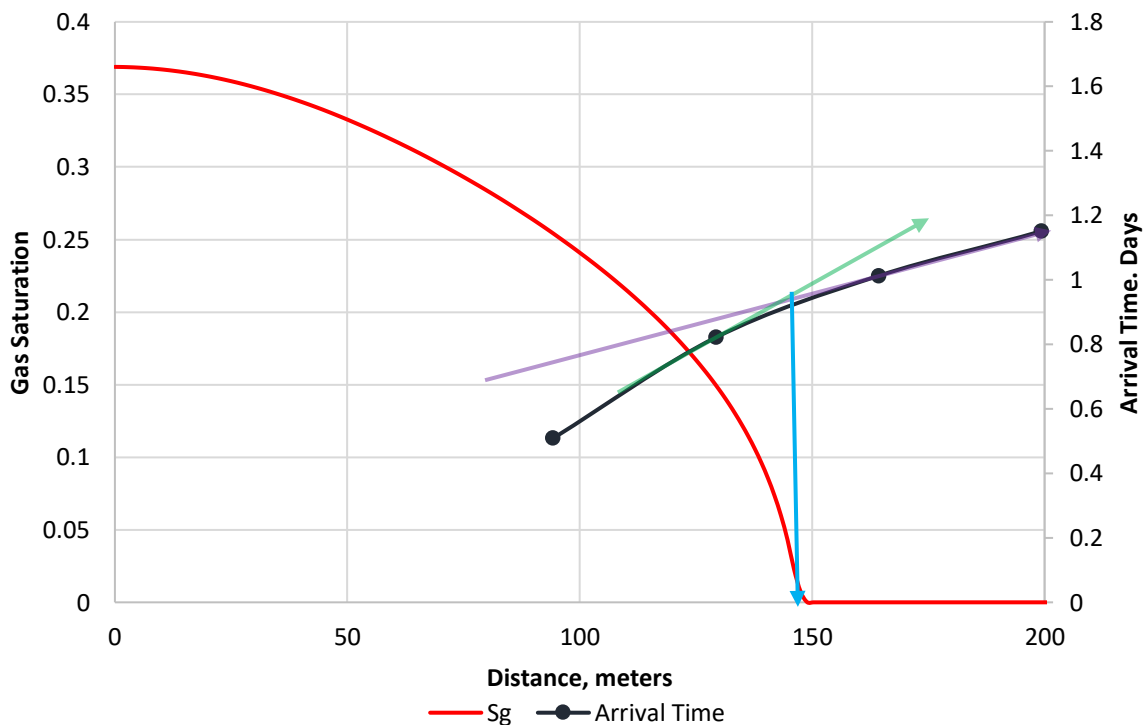


Figure 3.5. The base case for single layer. The tangent lines', colored purple and green, intersection show a good estimation of where the plume boundary lies which is defined as where the gas saturation is zero.

Table 3.2. Percent errors of arrival time of Riemann Sum and numerical simulation for single layer system

Distance	Base	Case 1	Case 2	Case 3	Case 4	Case 5
94.3	5.0	0.7	1.3	3.1	1.3	1.3
129.3	0.8	0.3	3.2	0.3	0.6	2.7
164.3	0.1	2.7	2.1	0.1	0.4	5.5
199.3	0.5	3.3	1.0	3.1	0.2	1.6
234.3	0.2	2.5	0.2	3.7	0.9	1.6
269.3	0.2	1.5	1.1	3.9	0.2	0.9
304.3	1.0	1.5	0.5	2.2	0.2	0.5

Table 3.3. Percent errors of arrival time of Riemann Sum and numerical simulation for multi-layer system

Distance	Base	Case 1	Case 2	Case 3	Case 4	Case 5
91.5	0.6	4.7	2.0	1.3	0.0	9.1
126.5	0.1	1.5	0.9	1.4	2.4	3.8
161.5	1.2	4.9	0.5	0.9	0.6	0.5
196.5	0.2	0.6	0.3	3.2	0.4	0.9
231.5	0.6	0.3	0.2	1.7	0.3	0.4
266.5	0.2	0.7	0.3	2.7	0.4	0.4
301.5	0.5	1.3	1.3	1.0	0.5	1.0

Tables 3.4. The percent errors in average gas saturations from inverting arrival time and the output average gas saturation from the simulation for single-layer system

Distance	94.3	129.3	164.3	199.3	234.3	269.3	304.3
Base	0.36	0.28	0.22	0.17	0.15	0.13	0.11
Base Output	0.33	0.29	0.24	0.20	0.17	0.15	0.13
Percent Error	11.3	2.8	8.3	12.1	13.6	15.1	16.6
Case 1	0.24	0.22	0.18	0.15	0.13	0.11	0.10
Case 1 Output	0.24	0.22	0.20	0.17	0.14	0.12	0.11
Percent Error	0.6	1.4	7.6	10.7	12.3	12.3	12.9
Case 2	0.40	0.34	0.27	0.21	0.18	0.15	0.13
Case 2 Output	0.39	0.35	0.31	0.26	0.22	0.19	0.17
Percent Error	1.8	3.5	14.1	18.2	19.3	21.7	22.3
Case 3	0.24	0.25	0.22	0.18	0.15	0.13	0.11
Case 3 Output	0.28	0.26	0.24	0.21	0.18	0.16	0.14
Percent Error	13.7	6.3	9.3	15.3	18.9	20.8	20.6
Case 4	0.35	0.28	0.20	0.17	0.14	0.12	0.10
Case 4 Output	0.37	0.31	0.25	0.21	0.18	0.15	0.14
Percent Error	4.1	11.8	17.4	19.6	20.8	22.8	23.5
Case 5	0.25	0.22	0.18	0.14	0.12	0.10	0.09
Case 5 Output	0.27	0.25	0.21	0.17	0.15	0.13	0.12
Percent Error	8.3	11.7	16.8	17.6	19.1	19.6	20.0

Tables 3.5. The percent errors in average gas saturations from inverting arrival time and the output average gas saturation from the simulation for multi-layer system

Distance	91.5	126.5	161.5	196.5	231.5	266.5	301.5
Base	0.34	0.29	0.23	0.18	0.15	0.13	0.11
Base Output	0.31	0.28	0.23	0.19	0.17	0.14	0.13
Percent Error	11.8	2.7	2.8	5.9	8.4	9.5	11.6
Case 1	0.28	0.24	0.19	0.16	0.13	0.11	0.10
Case 1 Output	0.22	0.21	0.19	0.16	0.14	0.12	0.11
Percent Error	24.2	12.3	0.5	1.8	5.1	6.8	8.9
Case 2	0.40	0.34	0.28	0.22	0.18	0.16	0.14
Case 2 Output	0.36	0.33	0.29	0.25	0.21	0.18	0.16
Percent Error	9.2	3.7	5.6	10.0	13.1	14.6	15.5
Case 3	0.28	0.26	0.23	0.19	0.16	0.13	0.12
Case 3 Output	0.26	0.25	0.23	0.21	0.18	0.15	0.14
Percent Error	5.4	4.1	2.3	9.3	11.4	14.0	14.1
Case 4	0.39	0.29	0.22	0.18	0.15	0.13	0.11
Case 4 Output	0.34	0.30	0.25	0.20	0.17	0.15	0.13
Percent Error	14.8	5.2	9.4	12.8	14.8	16.4	17.0
Case 5	0.28	0.25	0.21	0.16	0.13	0.11	0.10
Case 5 Output	0.25	0.23	0.21	0.17	0.15	0.13	0.11
Percent Error	9.4	5.9	0.2	6.5	11.6	13.3	13.0

### 3.7 Conclusion

This study has used numerical simulation techniques to characterize a CO<sub>2</sub> plume. Being able to characterize CO<sub>2</sub> plume is important as there are situations such as gas leaks where determining the extent and average gas saturation of the plume can play a vital role in remediation decisions. The industry uses pressure diagnostic plots obtained through well testing to determine reservoir parameters, but our study shows the strong potential of using well testing to characterize potential gaseous phase leaks.

The present study indicates that by using (i) interference well testing, (ii) the equation for two-phase diffusivity, and (iii) line source integral evaluation, average gas saturation can be accurately estimated. Geometry of the plume boundary can be also determined if sufficient observation points are set up around the active well in cases with no anisotropy.

Although this study demonstrates that the use of interference well testing holds promise as an investigative technique, there are opportunities for pursuing more extensive studies. This study did not include the effects of critical gas saturation or hysteresis affects that could significantly influence CO<sub>2</sub> plume behavior. In cases where multiple observation wells are not available, this study indicates that the ability to relate average gas saturation over time could play a vital role in the characterization of gas leaks

## **Chapter 4: Pressure Transient Test to Constrain CO<sub>2</sub> Plume Boundaries**

### **4.1 Introduction**

Geological carbon capture and storage (CCS) is recognized as a strategy for reducing CO<sub>2</sub> emissions. Also, enhanced oil recovery (EOR) using CO<sub>2</sub> has long been used for energy production from hydrocarbon reservoirs. A primary concern for successful CO<sub>2</sub> injection operations is the ability to economically and accurately monitor the CO<sub>2</sub> plume to ensure its containment in the target reservoir. By doing so, operators can efficiently prevent or be prepared to remediate migration of injected CO<sub>2</sub> to unwanted areas. In EOR applications, CO<sub>2</sub> containment is important to ensure maximized sweep efficiency of the injected CO<sub>2</sub>. We apply pressure transient analysis theory, which has been established in the upstream oil and gas industry for decades, to explore opportunities to effectively constrain the CO<sub>2</sub> plume boundaries in the geological formations.

Pressure transient analysis has been recently looked into to determine the CO<sub>2</sub> plume extent (Hosseini and Alfi 2016, Shakiba and Hosseini 2016, Sun et al. 2016, Sun, Lu, and Hovorka 2015, Hu 2017, Hu, Bayer, and Brauchler 2016, Hu et al. 2017, Hu et al. 2015a). These studies used harmonic and oscillatory pulse testing which involves observing the pressure at monitoring locations in response to a series of flow rate changes (pulses) at an active well (Johnson, Greenkorn, and Woods 1966). In pulse testing, determining the plume extent in any given direction requires at least two wells: the pulse well and the monitoring well. In addition, the pressure data are generally inverted and analyzed in frequency domain which is a barrier to convenient analysis of the data in real-time domain. The pressure arrival times from a pulse test were also used to characterize a CO<sub>2</sub> plume in a target reservoir (Zeidouni, Tran, and Munawar 2017, Tran and

Zeidouni 2017). Although using the arrival time is simpler and able to estimate the average gas saturation between two wells, it suffers the same consequence in pulse testing in that this method cannot determine the plume extent in one direction with a single monitoring location. In departure from interference-based methods, we introduce pressure transient technique requiring single well only.

Single well pressure transient testing (drawdown/buildup/injection/falloff) is widely used to determine reservoir properties and wellbore conditions. Log-log pressure diagnostic plots are used to identify different flow regimes in the reservoir and obtain reservoir/wellbore characteristics. In conventional pressure diagnostic plots, a combination of the pressure change (in response to constant rate perturbation) and its logarithmic derivative are used to identify different flow regimes. The logarithmic pressure derivative (hereafter derivative for brevity) is defined by:

$$\frac{d(\Delta p)}{d \ln t} = t \frac{d(\Delta p)}{dt} \quad (4.1)$$

where  $\Delta p$  is the pressure change from the initial value and  $t$  is time. Once the flow regimes are identified, the specialized graphical and/or computational approaches can be used to determine the reservoir/well properties (Lee, Rollins, and Spivey 2003, Spivey and Lee 2013). For a fully penetrating vertical well, the first observed flow regime (after the effects of wellbore storage and skin are passed) is the radial flow regime. Given its diffusive nature, the pressure averages out the small-scale heterogeneities and shows the bulk properties of the reservoir volume experiencing the pressure change. As a result, the radial flow regime is identified by a zero-slope linear behavior on the pressure derivative plot the magnitude of which is inversely proportional to fluid mobility (permeability divided by viscosity). For a well outside the CO<sub>2</sub> plume, the radial flow regime on



the derivative will be identified by a zero-slope line inversely proportional to the mobility of the native fluid. However, after the pressure effect reaches the CO<sub>2</sub> plume boundary, a deviation from the zero-slope line on the derivative will be observed. The deviation is due to the much higher mobility of the CO<sub>2</sub> compared to the native fluid mobility.

The primary goal in this study is to show that utilizing the pressure transient response to a constant rate perturbation at a distant well can be a strong tool to determine CO<sub>2</sub> plume boundaries. For field applications, CO<sub>2</sub> injection may be continuous or cease for a period of time during the pressure transient test in multiple test wells placed far from the injection well. The pressure diagnostic plots along with the new plume extent diagnostic plot proposed herein can determine how far the plume has migrated in the direction of the test well. By strategically choosing testing locations, not only can the operator determine how far the plume has migrated in each direction but find how the plume is moving over time. This technique can decrease the operator's financial burden associated with long-term monitoring by providing the capability to assess the position of the CO<sub>2</sub> plume in the target reservoir with greater certainty throughout the post-injection period.

In the following, we first develop a method to interpret the time at which deviation from zero-slope derivative occurs to obtain the distance from the testing well to the plume boundary. We use the superposition principle and no-flow boundary assumption to relate the deviation time to the plume boundary. We then test the relationship by applying to a variety of two and three dimensional numerical models that include homogeneous, heterogeneous, and anisotropic permeability distributions implemented into the system. Results are compiled in a format which shows the distance from the plume boundary to the test well, the corresponding diagnostic plots, and the result stemming from the diagnostic plot created by plotting the plume extent calculation

versus deviation time. Finally, we discuss the limitations of this pressure transient technique and potential solutions.

## 4.2 Methodology

In this study, we propose a pressure transient test based on bottom-hole pressure measurements at a fully-penetrating vertical well in response to constant-rate production/injection from/into a reservoir in which the CO<sub>2</sub> plume exists (Figure 4.1). For consistency, we consider production from the reservoir at the test well throughout this paper. Also, we assume that the reservoir hosting the CO<sub>2</sub> plume is a brine aquifer although the hosting reservoir can be any liquid-bearing permeable reservoir. Given that the plume extent is not known, the well is assumed to be outside the plume at an unknown distance from plume boundaries. The pressure during the production (drawdown) period is analyzed to determine the distance of the test well from the closest CO<sub>2</sub> plume boundary. Repeating the test in different wells at different locations/directions can fully constrain the plume boundaries. It is also possible to analyze the pressure buildup/falloff after production/injection and apply the same method presented here. However, one needs to replace the actual time by equivalent time function (Agarwal 1980). Again, for consistency, we only consider pressure drawdown during production in this study.

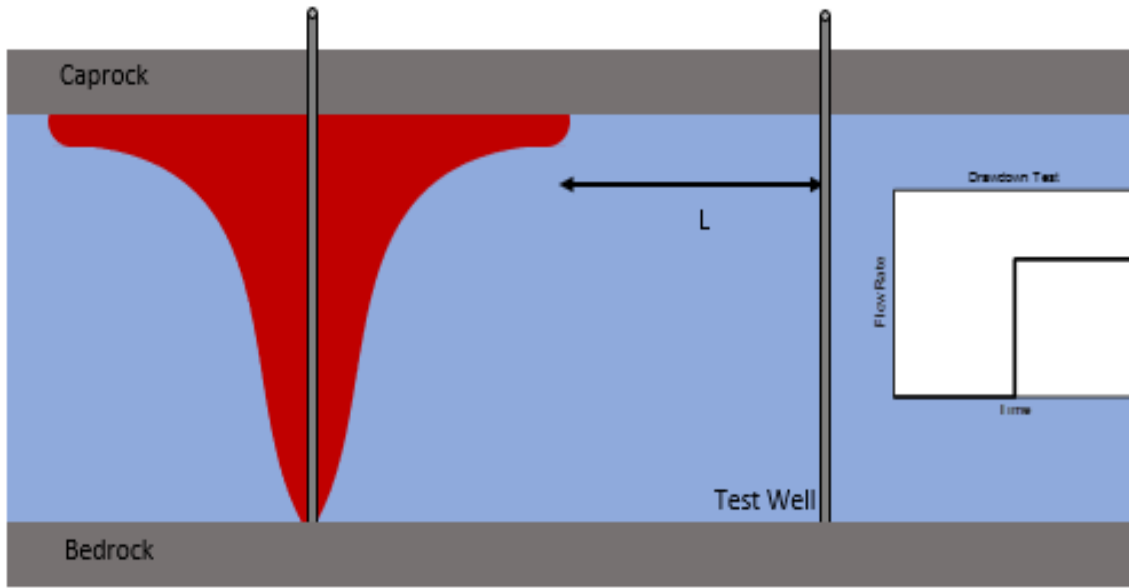


Figure 4.1. Schematics illustrating the typical CO<sub>2</sub> plume and drawdown test in a reservoir to estimate the plume extent.

#### 4.2.1 Pressure Drawdown Test

The primary purpose of pressure drawdown testing is to obtain the average reservoir permeability,  $k$ , of the reservoir, and to assess the damage/stimulation of the wellbore (skin). Log-log diagnostic plot of pressure derivative with respect to time is used to identify different flow regimes. For a fully penetrating vertical well, early time may show wellbore storage effect identified by unit slope linear behavior, followed by radial flow represented by a zero-slope horizontal line. The time at which the derivative deviates from the zero-slope line, marks the end of radial flow and is followed by boundary effects. For our case, the boundary is the outer edge of the CO<sub>2</sub> plume. The hypothesis of detecting the CO<sub>2</sub> plume boundary using pressure drawdown test is made possible due to the higher mobility ( $\lambda=k/\mu$ ) of the gaseous CO<sub>2</sub> relative to reservoir native fluid (brine). This implies that the mobility ratio ( $M$ ) of the CO<sub>2</sub> plume region over the brine region is larger than 1. In addition, the storativity ratio is also larger than 1. However, when the mobility ratio ( $M$ ) is large,

the storativity ratio has only a minor effect on the shape of pressure derivative (Chen, Chu, and Sadighi 1996). The original reservoir mobility can be calculated by using the zero-slope line value ( $m_0$ ) by Equation (4.2).

$$m_0 = \frac{q\mu B}{4\pi kh} \quad (4.2)$$

If the CO<sub>2</sub> plume was 100% gaseous CO<sub>2</sub>, we would see a sharp downward deviation followed by another zero-slope line in the derivative plot due to the higher mobility of gaseous CO<sub>2</sub>. But in reality, the gaseous CO<sub>2</sub> coexists with aquifer brine in the occupied pores, the overall mobility is still increased, however, the decline in the derivative plot is not as rapid but rather much slower and the zero-slope line does not occur. We aim to use the time which corresponds to the deviation from the radial flow caused by the CO<sub>2</sub> plume to detect the CO<sub>2</sub> plume boundary closest to the tested well. In order to use the time of derivation effectively, we develop a model considering the plume as constant-pressure boundary. The constant-pressure boundary assumption is also used in finding distance to the gas-oil contact in a well located in the oil leg down-dip from a gas-oil contact (Abbaszadeh and Hegermen 1990, Streltsova-Adams 1979). This assumption simplifies development of analytical relationship between deviation time and plume boundary using the theory of image wells and superposition. Also, considering the CO<sub>2</sub> plume as constant-pressure boundary (merely for finding the deviation time) is relevant since the existence of any boundary will similarly affect the deviation from the initial radial flow. In the following, we derive the equations to determine the location of the plume boundary.

#### 4.2.2 Relationship of deviation time with distance to plume boundary

Treating the plume boundary as a constant-pressure boundary, the pressure at the producing well will be given by:

$$\Delta p = p_i - p_{wf} = \frac{q\mu B}{4\pi kh} \left( -Ei\left(-\frac{r_w^2}{4\eta t}\right) + Ei\left(-\frac{4L^2}{4\eta t}\right) \right) \quad (4.3)$$

where,  $\eta$  is the pressure diffusivity given by  $\eta = \frac{k}{\phi\mu c_t}$ .  $\phi$  and  $c_t$  are the porosity and total compressibility respectively.  $p_i$  and  $p_{wf}$  are the initial pressure and the well flowing pressure respectively.  $q$  and  $B$  are the surface production rate and total formation volume factor respectively. The first term in the parentheses in the right-hand side of Equation (4.3) corresponds to the actual well while the second term is due to the image well at distance  $2L$ .  $L$  is the distance from the well to the plume boundary. The derivative of the pressure is given by:

$$m = t \frac{d\Delta p}{dt} = \frac{q\mu B}{4\pi kh} \left( \exp\left(-\frac{r_w^2}{4\eta t}\right) - \exp\left(-\frac{L^2}{\eta t}\right) \right) \quad (4.4)$$

If there is no boundary, the derivative would be:

$$m_0 = \left( t \frac{d\Delta p}{dt} \right)_0 = \frac{q\mu B}{4\pi kh} \exp\left(-\frac{r_w^2}{4\eta t}\right) \quad (4.5)$$

Therefore, the derivative deviation (from zero-slope line) at the time of arrival at the boundary is given by:

$$|m_0 - m| = \frac{q\mu B}{4\pi kh} \exp\left(-\frac{L^2}{\eta t}\right) \quad (4.6)$$

Therefore, the deviation time ( $t$ ) can be used to calculate  $L$ :

$$L = \sqrt{\eta t \ln\left(\frac{q\mu B}{4\pi kh|m_0 - m|}\right)} \quad (4.7)$$

Since the late-time derivative before reaching the boundary is  $m_0 = \left(t \frac{d\Delta p}{dt}\right)_0 = \frac{q\mu B}{4\pi kh}$ , we can write:

$$L = \sqrt{\eta t \ln\left(\frac{m_0}{|m_0 - m|}\right)} \quad (4.8)$$

The mobility, ( $\lambda = k/\mu$ ), is usually unknown unless obtained from prior well tests. We utilize Equation (4.2) to calculate the mobility from primary radial flow zero-slope line. The mobility is then used in Equation (4.8) to find the plume distance from the test well,  $L$ . From Equation (4.2),  $m_0$  should be estimated as the average at which radial flow occurs. Although there should be a clear deviation in the pressure derivative plot indicating that the boundary has been reached, there may be still difficulty in determining the actual time of deviation. Based on Equation (4.8), we find that Cartesian plot of the plume distance ( $L$ ) calculated from Equation (4.8) versus square-root of deviation time ( $\sqrt{t}$ ) can help in closely estimating the plume boundary. This graph shows a sharp change in slope at the plume boundary as shown in the example cases in Section 4. The clear deviation occurs at the end of radial flow and upon start of plume boundary effects. The intersection point of two lines with different slopes can be used in estimating the distance between the plume boundary and the test well. In the following, the technique proposed here is extensively

examined through applying to synthetic data generated by a commercial numerical simulation software (CMG-GEM 2015) for various cases.

#### 4.3 Model Setup

We examine the applicability of the drawdown test to determine CO<sub>2</sub> plume boundary by modeling pressure response at a test well outside the plume. Although having a single well is sufficient to determine how the plume is behaving in a homogeneous reservoir, multiple wells should be used in presence of heterogeneity and/or anisotropy.

In examining the method, we start with its application to a series of cases. Models are built considering both single layer and multilayer reservoirs. The single layer models are composed of three cases: (1) homogeneous, (2) heterogeneous, and (3) heterogeneous-anisotropic for two different test well locations. For multilayer reservoir, four cases are investigated: (1) homogeneous, (2) vertically and horizontally heterogeneous, (3) vertically and horizontally heterogeneous with  $x$ - $y$  anisotropy for two test wells, and (4) two plumes created by having two distinct injection zones separated by an impermeable layer. The CO<sub>2</sub> plume is created by a sandface injection rate of  $1.4 \times 10^5 \text{ m}^3/\text{day}$  for 45 days into a 7-m thick aquifer. The injection rate is chosen to create a large plume. For the multilayer cases, the thickness is divided into 7 layers of 1-m thickness each. The CO<sub>2</sub> is injected through all layers. Following the 45 days, the pressure drawdown test at the distant test well starts by producing brine at a constant rate of  $300 \text{ m}^3/\text{day}$  for 3 days. The reservoir properties are taken from those given for a real CO<sub>2</sub> storage site model in the southeast United States (Haghighat et al. 2013, Petrusak et al. 2010, Koperna 2013, Zeidouni, Hovorka, and Shi 2016). The initial reservoir pressure is 30 MPa at 3000-m depth and the initial reservoir temperature is at 110 deg C. The porosity of the reservoir for all cases has a value of

0.18. Viscosity of water is 0.5 cp. The irreducible water saturation is 0.35. The relative permeability of the aqueous phase is introduced using  $\lambda=0.95$  (van Genuchten 1980). Relative permeability of the CO<sub>2</sub> gaseous phase is introduced by (Corey 1954) model, using  $n=1$ ,  $S_{gc}=0$ , and  $k_{rg}^0=1$ . For capillary pressure, the (van Genuchten 1980) formulation is used with  $P_0=20$  kPa and  $m=0.8$ . The relative permeability and capillary pressure equations are summarized in Table 4.1. The models were built using CMG-GEM compositional simulator (CMG-GEM 2015) to model the drawdown test for all cases.

The reservoir area is  $3.1 \times 10^7$  m<sup>2</sup> which is discretized into  $161 \times 161$  cells and the injection well is located at  $n_x=81$  and  $n_y=81$ . The injection and test wells are placed in a refined section of the grid. For all cases, the test well is located 500 m from the injection well in the  $x$ -direction. For cases that include anisotropy, heterogeneity-anisotropy, and vertical and horizontal heterogeneity with  $x$ - $y$  anisotropy, a second test well is added 500 m from the injection well in the  $y$ -direction. The homogeneous reservoir for single layer has permeability of 36 mD. We add heterogeneity and then combined heterogeneity and anisotropy to enable more realistic asymmetric CO<sub>2</sub> plume. For the heterogeneous case in single layer, the  $x$ -direction and  $y$ -direction permeability field were created by assigning permeability values near the injection well with the range of 11 to 60 mD and then using an inverse distance weighting interpolation to fill in the rest of the grid blocks (Shepard 1968). For heterogeneous-anisotropic case, the same permeability field stated above was used in the  $x$ -direction, and the  $y$ -direction permeability is half that of the  $x$ -direction's permeability.

The permeability is also 36 mD for the multilayer homogeneous case. In the vertically and horizontally heterogeneous case, the permeability field was created in a similar fashion to single layer heterogeneous case but each layer is different by assigning values of permeability differing



in range and location. For the vertically and horizontally heterogeneous case with  $x$ - $y$  anisotropy, the permeability field was created with the same permeability in the  $x$ -direction as stated above with the  $y$ -direction permeability being half that of the  $x$ -direction's permeability. For all multilayer cases, the ratio of vertical permeability to horizontal permeability,  $k_v/k_h$ , is 0.2.

Table 4.1. Drainage relative permeability and capillary pressure curve equations.

Aqueous phase relative permeability: van Genuchten (1980)	
$k_{ra} = \sqrt{S^*} \left( 1 - \left( 1 - [S^*]^{1/\lambda} \right)^\lambda \right)^2$	where: $S^* = \frac{S_a - S_{wirr}}{1 - S_{wirr}}$
CO <sub>2</sub> -rich phase relative permeability: Corey (1954)	
$k_{rg} = k_{rg}^0 \left( 1 - \hat{S} \right)^n \left( 1 - \hat{S}^2 \right)$	where: $\hat{S} = \frac{S_a - S_{wirr}}{1 - S_{wirr} - S_{gc}}$
Capillary pressure: van Genuchten (1980)	
$P_c = -P_0 \left( [S^*]^{-1/m} - 1 \right)^{1-m}$	where: $S^* = \frac{S_a - S_{wirr}}{1 - S_{wirr}}$

#### 4.4 Results

To compare with the numerical simulation, the plume extent is considered to be the point at which the gas saturation reaches less than 1% in the corresponding grid block. For multilayer cases, the plume edge is where the vertically averaged gas saturation becomes less than 1%. In the following, we investigate the results for single- and multiple-layer cases which are summarized in Table 4.2. Figures 4.2-4.10 show the plume shape, diagnostic plots and plume estimation for various cases.

Table 4.2. Results showing the estimated distance of the plume boundary to the active monitoring well for (a) single layer and (b) multilayer.

Single-Layer Results (a)			
Case	Estimated L, m	Numerical L, m	Percent Error
Homogeneous	340	350	2.86
Heterogeneous	337	340	0.89
Heterogeneous-Anisotropic Well Location 1 (x-direction)	285	310	8.77
Heterogeneous-Anisotropic Well Location 2 (y-direction)	370	380	2.70

Multiple-layer Results (b)			
Case	Estimated L, m	Numerical L, m	Percent Error
Homogeneous	342	346	1.16
Vertically and Horizontally Heterogeneous	326	340	4.29
Vertically and Horizontally Heterogeneous with x-y Anisotropy Well Location 1 (x-direction)	276	303	9.78
Vertically and Horizontally Heterogeneous with x-y Anisotropy Well Location 2 (y-direction)	365	364	0.27
Two Plumes Separated by Impermeable Layer	327	330	0.92

#### 4.5.1 Single-Layer Cases

As expected, the CO<sub>2</sub> plume for a homogeneous reservoir in single layer provides a symmetrical plume (Figure 4.2a). The distance from the plume boundary to the test well taken from the numerical simulation is 350 m. The zero-slope derivative value ( $m_0$ ) obtained from the derivative is 556 kPa. Knowing the permeability and viscosity from the numerical simulation, the  $m_0$  value can be also calculated using Equation 4.2. The  $m_0$  value is found to be identical to that obtained from the derivative plot which shows that the numerical simulation correctly calculates the pressure response. Looking at the pressure diagnostic plot in Figure 4.2b to determine the time of deviation to be used in Equation 4.8 may be insufficient. This is a problem because deviation time can be subjective. By calculating  $L$  from Equation (4.8) and plotting versus  $\sqrt{t}$  as seen in Figure 4.2c, the distance from the plume boundary to the test well can be accurately estimated. By drawing two lines of differentiating slopes, the intersection yields 340 m in comparison to the actual value from the numerical simulation, 350 m. Based on Equation (4.8), the first slope is proportional to square root of brine diffusivity coefficient and the second slope is proportional to square root of diffusivity coefficient of the inner plume.

The heterogeneous case provides a slightly irregular plume shape (displayed in Figure 4.3a) due to the varying permeability field. The distance from the test well to the plume boundary taken from the simulation is 340 m. The  $m_0$  value is 470 kPa which signifies a higher mobility than the homogeneous case. With the method proposed of using the derivative plot and  $L$  vs  $\sqrt{t}$  (Figures 4.3b and 4.3c), the intersection of the two unique sloping lines gives an estimation of 337 m.

Single layer heterogeneous-anisotropic case is investigated considering two wells: one well 500 m in the  $x$ -direction and another well 500 m in the  $y$ -direction with respect to the injection well. The

$y$ -direction permeability is half that of the  $x$ -direction causing an oval shape plume while the heterogeneity causes asymmetric plume (Figures 4.4a and 4.5a). Taken from the simulation, the distance from the plume boundary to the test well located in the  $x$ -direction is 310 m while the distance from the plume boundary to the test well placed in  $y$ -direction is 380 m. The derivative plots in Figures 4.4b and 4.5b differ in that the  $m_0$  values are 665 and 761 kPa for the test wells. The pressure drawdown test done in the well located in the  $y$ -direction reveals a higher mobility which should be expected as the permeability in  $y$ -direction is half that of the  $x$ -direction. The results obtained from Figures 4.4c and 4.5c are 285 m and 370 m respectively compared to the actual distances from the numerical simulation, 310 m and 380 m for the test well in the  $x$ -direction and  $y$ -direction respectively.

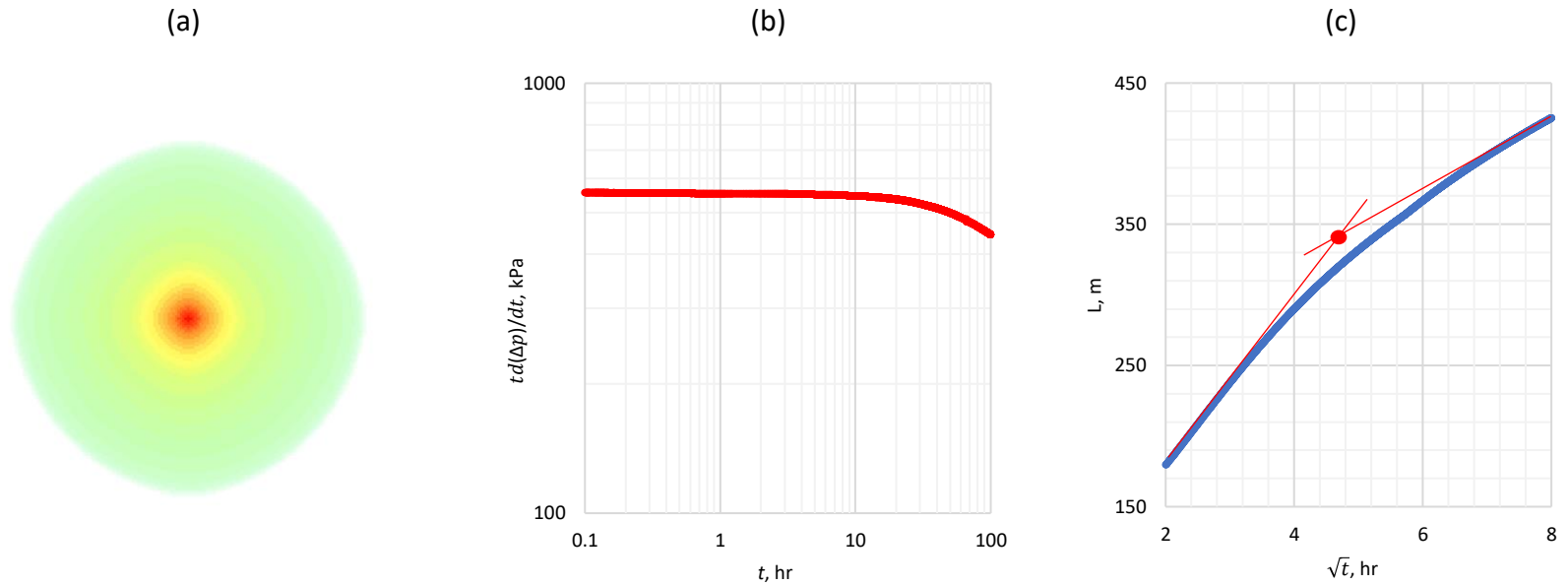


Figure 4.2. Homogeneous single-layer case: (a) the plan view of the plume, (b) the derivative plot, and (c)  $L$  from Equation (4.8) versus  $\sqrt{t}$  to determine the plume extent. Deviation point (plume boundary) is marked by the red circle in (c) created by intersection two lines of different slopes.

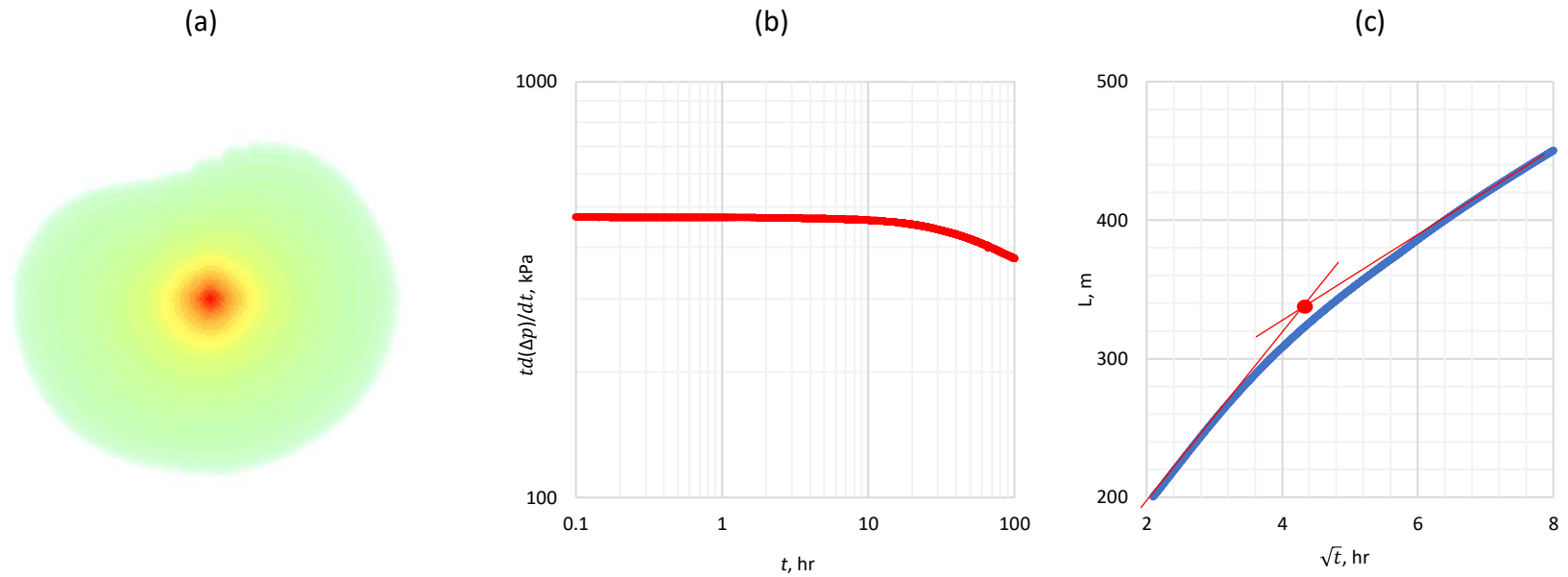


Figure 4.3. Heterogeneous single-layer case: (a) the cross section of the plume, (b) the derivative, and (c)  $L$  from Equation (4.8) versus time to determine the plume extent.

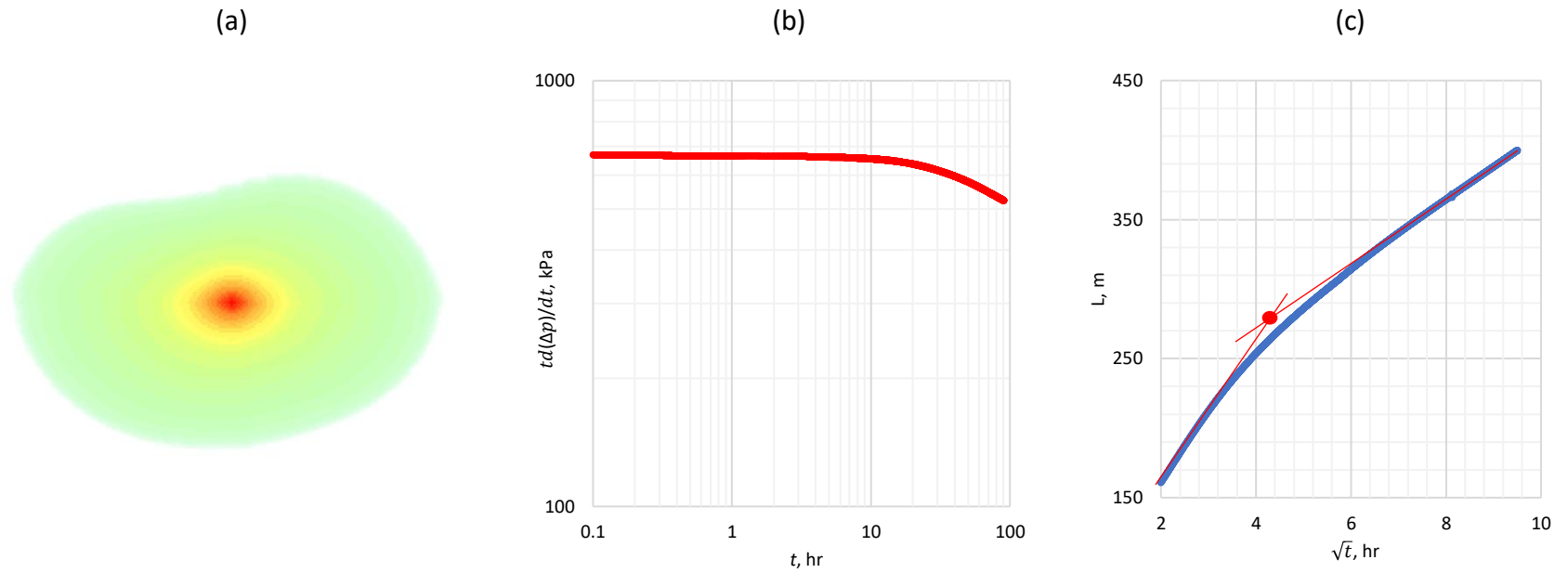


Figure 4.4. Heterogeneous anisotropic single-layer case, Well 1 ( $x$ -direction well): (a) the plan view of the plume, (b) the derivative, and (c)  $L$  from Equation (8) versus time to determine the plume extent.

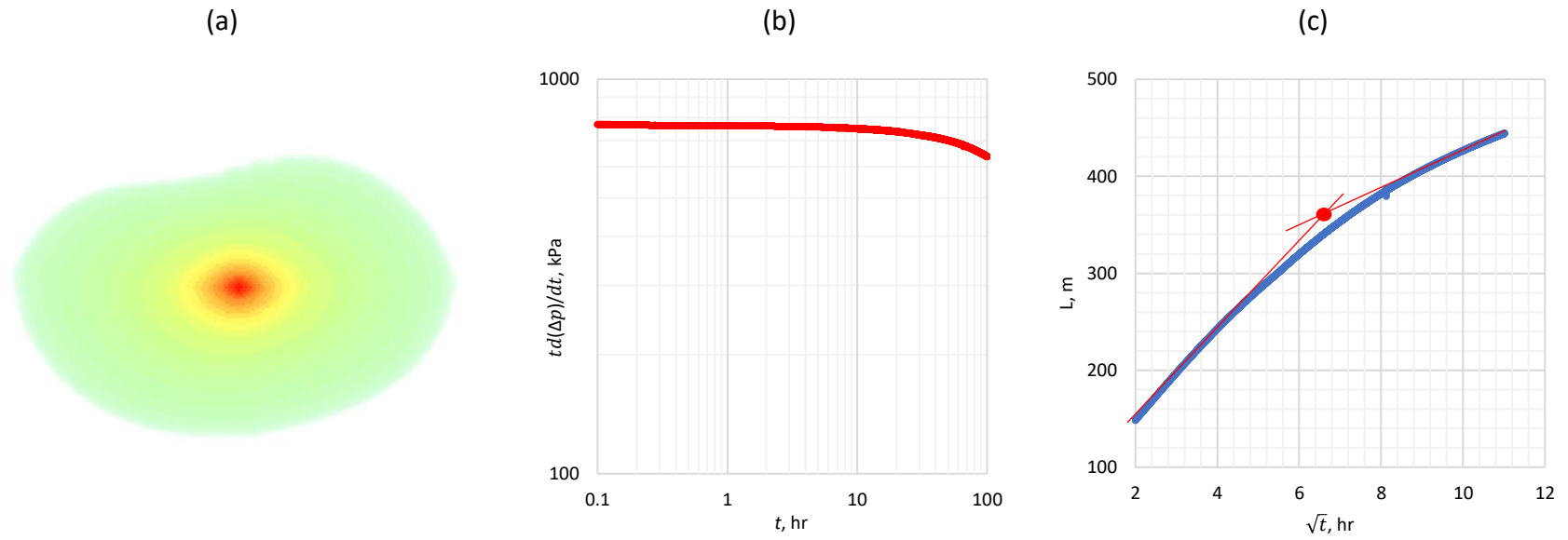


Figure 4.5. Heterogeneous anisotropic single-layer plume, Well 2 (y-direction well): (a) the side view of the plume in the  $x$ - $z$  direction, (b) the derivative, and (c)  $L$  from Equation (4.8) versus time to determine the plume extent.



#### 4.5.2 Multi-Layer Cases

With the vertical permeability being 7.2 mD versus the horizontal permeability of 36 mD for the homogeneous case, the gas plume migrated upwards but still left trace amounts of gas horizontally in each layer as seen in Figure 4.6a.i-4.6a.viii. The  $m_0$  value obtained from the derivative plot in Figure 4.6b is 554 kPa which is very similar to the single layer homogeneous case, 556 kPa, which signifies negligible effect of vertical permeability on mobility estimation. The distance from the plume boundary to the test well is taken as an average of how far the CO<sub>2</sub> has migrated in each layer. For the homogeneous cases, this is 330, 334, 338, 342, 346, 350, 354 m for layers 1 through 7 (numbered from top to bottom) respectively with the average being 346 m. By using the  $L$  vs  $\sqrt{t}$  plot, the estimated distance of the plume boundary to the test well is 342 m.

To create a more realistic plume, vertical and horizontal heterogeneity are added to the system. As shown in Figures 4.7a.i-4.7a.viii, the plume's shape differ in each layer. The cross section of the heterogeneous case is not as uniform as the homogeneous case. The distance from the plume boundary to the test well for layers 1 through 7 respectively is 326, 330, 334, 338, 342, 350, 362 m with the average of 340 m. The value obtained from the zero-slope radial flow line in the derivative plot, Figure 4.7b, is 474 kPa. The pressure drawdown test for the heterogeneous case shows higher mobility, due to the higher average permeability. The plume migrates slightly less towards the test well, 340 m compared to the 346 m from the homogeneous case. When using the  $L$  vs  $\sqrt{t}$  plot, Figure 4.7c, the estimated value of the distance between the plume boundary and test well is 326 m. This is not only accurate to the numerical value of 340 m, but also witnesses the same trend as the numerical results. When comparing heterogeneous to homogeneous cases the

estimated value of heterogeneous case is less than estimated value for homogeneous case, 326 m versus 342 m, similar to the trend seen in the numerical results 340 m versus 346 m.

To add another element of complexity,  $x$ - $y$  anisotropy is added to the vertically and horizontally heterogeneous case. Similar to the single layer heterogeneous-anisotropic case, this multi-layer case has two wells. One placed 500 m in the  $x$ -direction, and the other 500 m in the  $y$ -direction relative to the same injection well. As seen in Figures 4.8a.i-4.8a.vii and 4.9a.i-4.9a.vii, the plume is the same, but the cross section 4.8a.viii and 4.9a.viii is very different. Figure 4.8a.viii is what the pressure transient from the  $x$ -direction test well is going to see, which is a much thicker plume compared to what the pressure transient will see for the test well in the  $y$ -direction, Figure 4.9a.viii. The  $m_o$  obtained from Figures 4.8b and 4.9b values are similar to one another at 670 kPa and 674 kPa for the testing wells in the  $x$ -direction and  $y$ -direction respectively. With both wells experiencing similar mobilities, the pressure transient in the  $x$ -direction well will deviate first due to being closer to the plume as this is evident in Figures 4.8b and 4.10b. The average length of the plume to the  $x$ - and  $y$ -direction test wells obtained from the numerical simulation are 303 m and 364 m respectively. The results by using the  $L$  vs  $\sqrt{t}$  for both cases are 276 m and 365 m for the  $x$ - and  $y$ -direction well respectively.

The last case differs from all previous cases in that there are two plumes shown in Figures 4.10a.i-4.10a.vii. The plume is created by two different perforation intervals separated by an impermeable interlayer. The  $m_o$  value, 646 kPa, gives the average permeability to be 35.7 mD. Two symmetrical plumes are expected as the two zones composing of three layers are the same in the homogeneous systems. The average plume boundary to the test well while neglecting the impermeable layer is 330 m. By plotting the  $L$  versus  $\sqrt{t}$  plot, Figure 4.10c, the estimated distance from the plume

boundary to the test well is 327 m. Compared to the actual distance, 330 m from the numerical model, the results suggest that the presence of impermeable layer does not hinder this method from correctly predicting the CO<sub>2</sub> boundary relative to the test well.

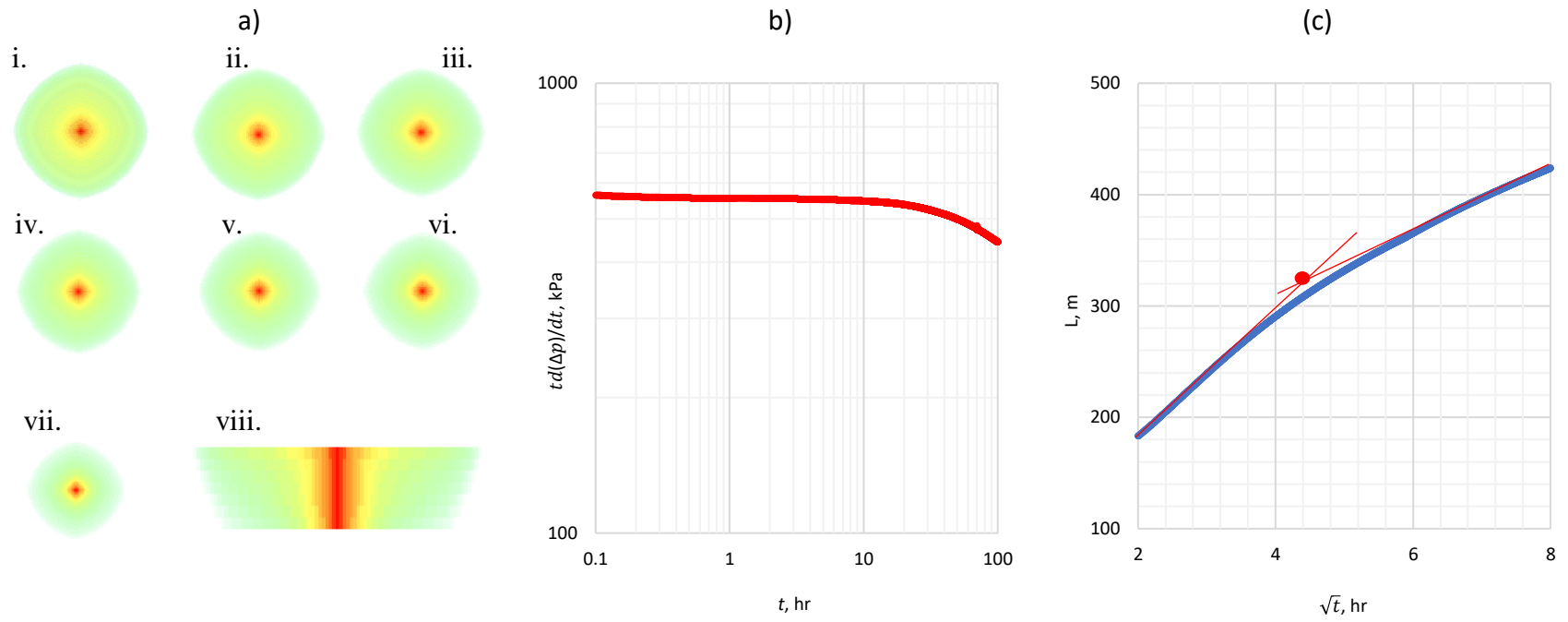


Figure 4.6. Homogeneous multilayer case: (a.i-a.viii) the plume shape in layers 1 through 7 (numbered top to bottom) and the  $x$ - $z$  plane cross section of the plume, (b) the derivative, and (c)  $L$  from Equation (4.8) versus time to determine the plume extent.

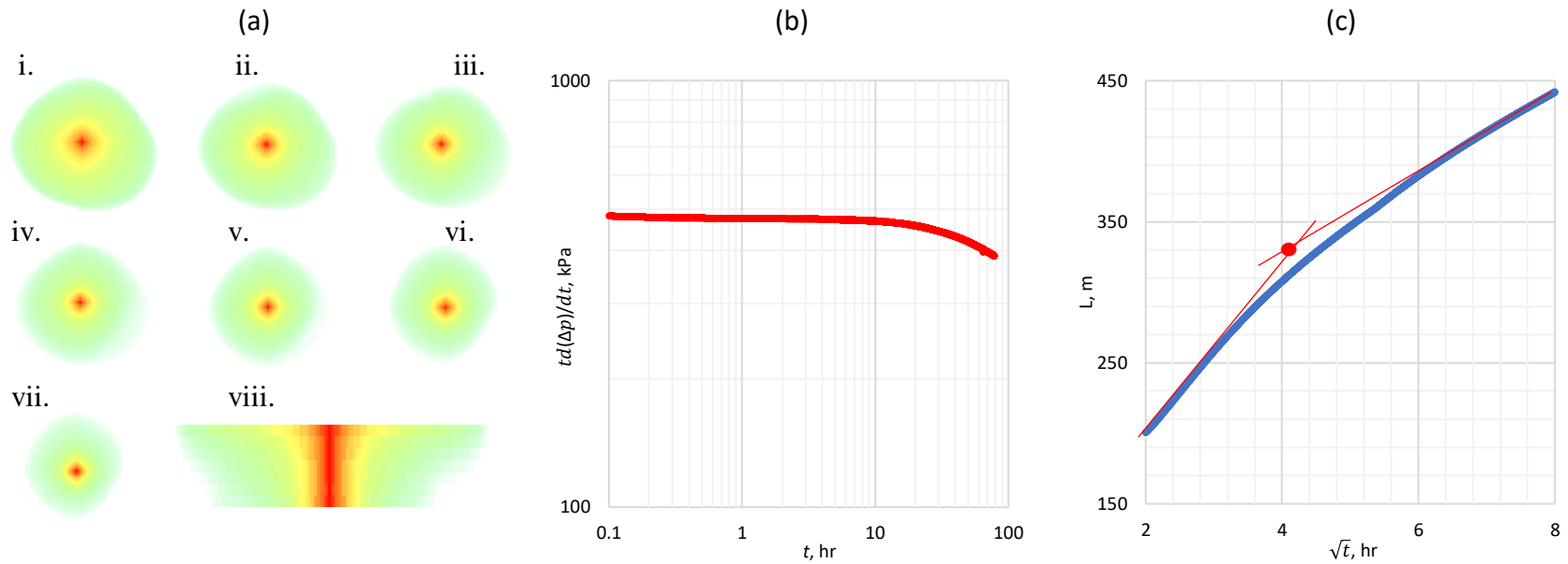


Figure 4.7. Vertically and horizontally heterogeneous case: (a.i-a.viii) the plume shape in layers 1 through 7 (numbered top to bottom) and the x-z plane cross section of the plume, (b) the derivative, and (c)  $L$  from Equation (4.8) versus time to determine the plume extent.

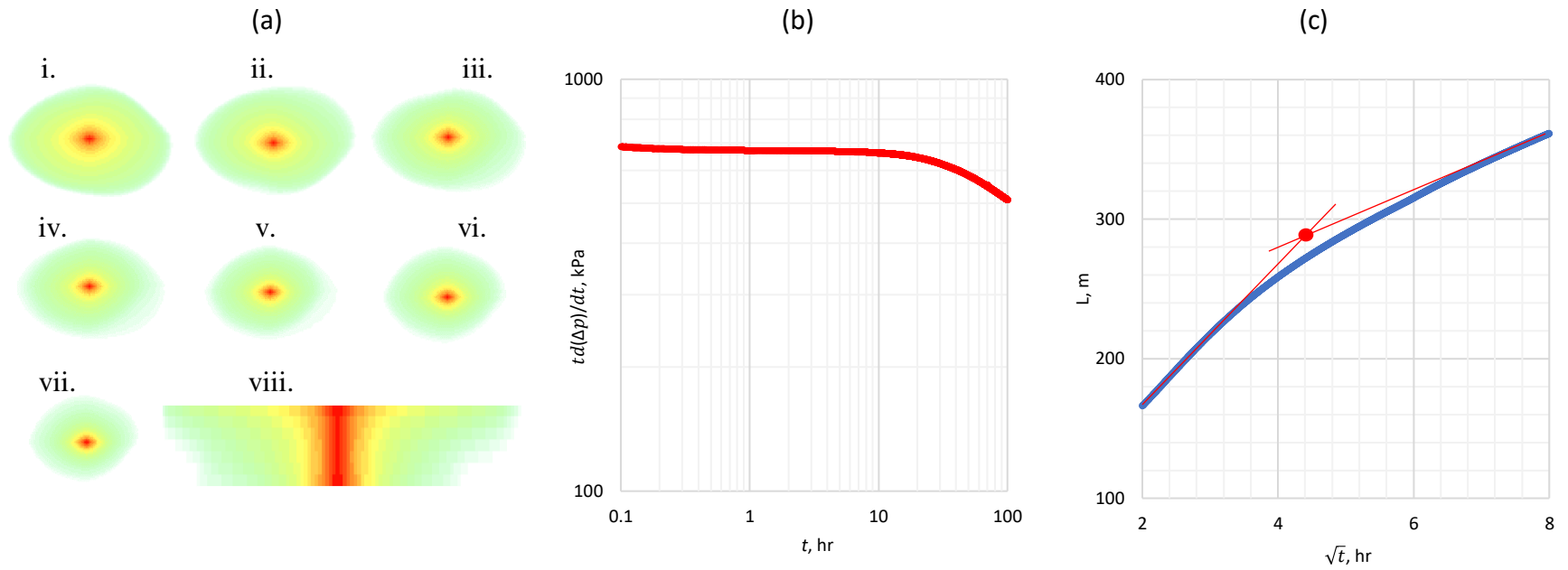


Figure 4.8. Vertically and horizontally heterogeneous case with  $x$ - $y$  anisotropy, Well 1 : (a.i-a.viii) the plume shape in layers 1 through 7 (numbered top to bottom) and the  $x$ - $z$  plane cross section of the plume, (b) the derivative, and (c)  $L$  from Equation (4.8) versus time to determine the plume extent.

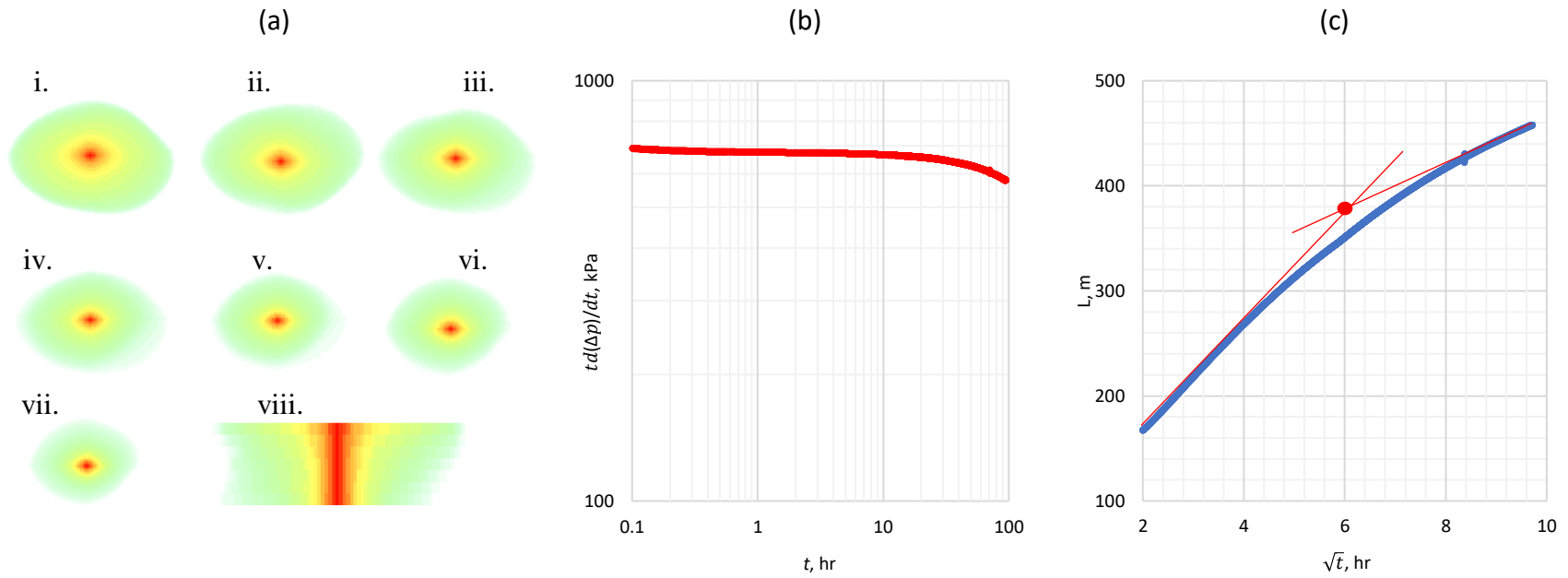


Figure 4.9. Vertically and horizontally heterogeneous case with x-y anisotropy, Well 2: (a.i-a.viii) the plume shape in layers 1 through 7 (numbered top to bottom) and the y-z plane cross section of the plume, (b) the derivative, and (c)  $L$  from Equation (4.8) versus time to determine the plume extent. The cross section in a.viii displays a shorter length plume versus the previous case of the cross section in the x-z plane, Figure 4.8aviii.

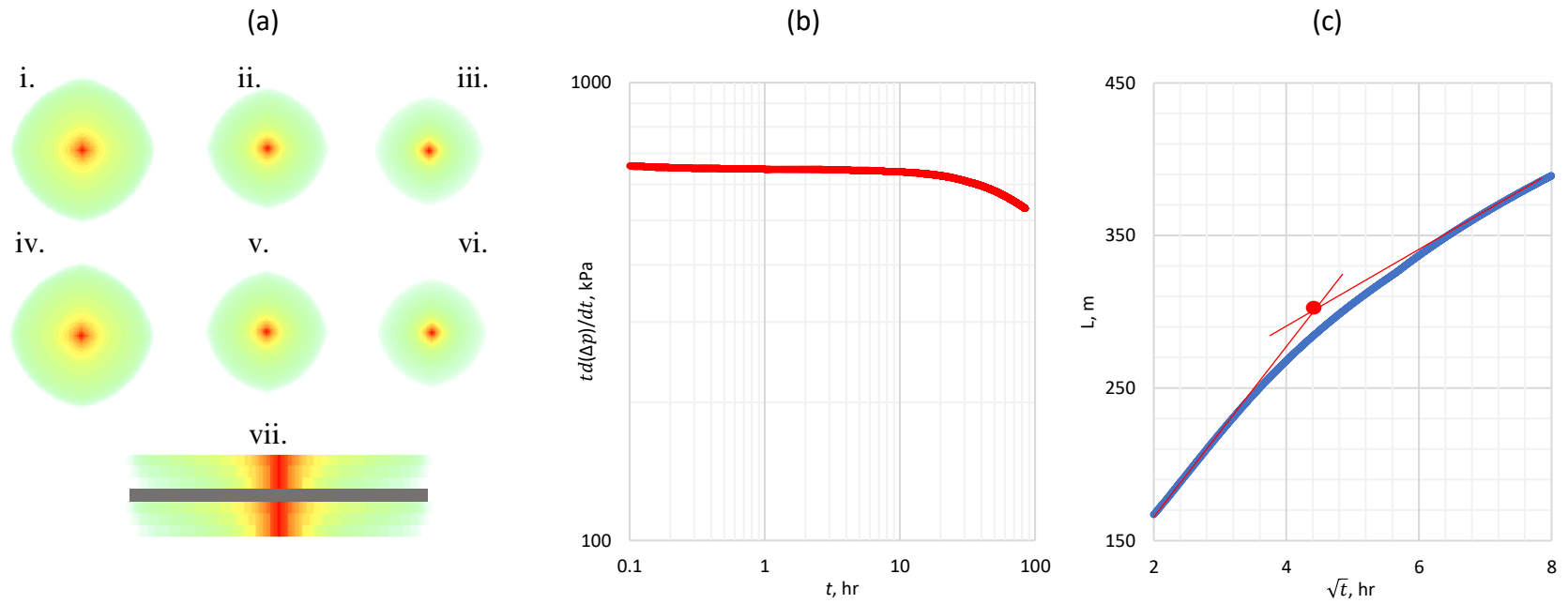


Figure 4.10. Homogeneous multilayer case with impermeable interlayer: (a.i-a.viii) the plume shape in layers 1 through 7 (numbered top to bottom) and the y-z plane cross section of the plume, (b) the derivative, and (c)  $L$  from Equation (4.8) versus time to determine the plume extent. The impermeable layer shows no effect in either (b) the derivative plot and (c) the  $L$  vs  $\sqrt{t}$  plot.



## 4.5 Discussion

In the presence of local heterogeneities, the zero-slope line may not be fully established and therefore, it may be difficult to obtain the deviation time. By running a baseline test prior to CO<sub>2</sub> injection, the time of deviation can be clearly identified. In addition, a correct  $m_0$  value can be also obtained. Utilizing the time of deviation from this method should yield accurate results in determining the location of the plume boundary without the need for  $L$  versus  $\sqrt{t}$  plot.

With the continuous injection of CO<sub>2</sub>, background noise due to interference from injection activities can be introduced into the pressure data from the drawdown test. Through our numerical investigation, the noise was found to be minimized by increasing the brine production in the test well during the injection of CO<sub>2</sub>. If the constant production rate is too high or not achievable to overcome the noise created by the injection well, shutting in the CO<sub>2</sub> injector and waiting for pressures to relatively stabilize before starting the pressure drawdown test at a lower rate can also minimize the noise in the pressure data. The range of stabilization times can vary depending on the rate of CO<sub>2</sub> injection and the time of the injection period. Ultimately, the optimal flow rates of CO<sub>2</sub> and brine, along with the ability to shut in the CO<sub>2</sub> injector, should be decided considering the reservoir characteristics being studied.

To determine the length of time required for the drawdown test, distance from the injection well(s) and the test well has to be considered. A good estimation to determine the drawdown test period is to use the single-phase diffusivity equation to determine the time it takes for the pressure propagation to reach the injection well. By doing so, the plume boundary should be noticeable as the deviation should occur before the time the pressure propagation would reach the injection well in the single-phase scenario. If permeability is unknown, then the drawdown test should be done

until a clear downward deviation is seen in the derivative plot due to the higher mobility CO<sub>2</sub>. 3-day test duration was found enough for a 500-m spaced test well in a 36 mD average permeability reservoir with the characteristics given in section 3. However, this duration may not be sufficient for cases with lower diffusivity coefficients.

The high mobility of gas relative to brine makes pressure transient analysis possible to detect the CO<sub>2</sub> plume. If the difference in mobility of the two fluids is small, then the pressure propagation may not see the CO<sub>2</sub> plume. Thus, no deviation from the zero-slope line in the derivative plot would be observed. There are other factors that can lower the relative difference in mobility of the two fluids. Increasing the  $n$  value (see Table 4.1) for the CO<sub>2</sub> rich relative permeability curve gives lower mobility to the CO<sub>2</sub> gaseous phase, and decreasing the  $\lambda$  value (see Table 4.1) for the aqueous phase relative permeability may decrease aqueous phase mobility such that the difference in mobility is not enough to see a clear deviation in the pressure diagnostic plot. The relative difference in mobility between the CO<sub>2</sub> and brine would have to be very small for the pressure propagation to not detect the CO<sub>2</sub>. The results from the numerical study presented above suggest that the pressure propagation sees the CO<sub>2</sub> plume in its outermost region of the plume where the CO<sub>2</sub> saturation is less than 1%. It should be noted that the proposed methodology estimates  $L$  at a specific time. The assumption of constant  $L$  is reasonable considering that the rate of plume expansion (time scale of changes in  $L$ ) is generally much slower than the test time-scale.

#### 4.6 Conclusions

The knowledge of CO<sub>2</sub> plume boundaries and other possible hosting formation is crucial to the accountability and safety of CO<sub>2</sub> storage operations. In this study, we introduced a pressure transient test at a distant well from the CO<sub>2</sub> injection well to determine the extent of the plume at

any given time. The test is based on producing/injecting at constant rate at the distant well for a short period of time (hours to days) and observing the pressure behavior in that well. Deviation time from the zero-slope line on diagnostic plot which correspond to radial flow in the reservoir was related to the plume distance from the distant well. A series of simulations which included a wide variety of cases were performed using numerical models to demonstrate the application of the method. Results suggest that, the time at which there is a deviation from radial flow in the derivative diagnostic plot can be used as a means of determining where the CO<sub>2</sub> has migrated relative to a distant test well. The errors in estimation of the plume extent varied in the range of 0.27 % to 9.78 % with a mean value of 3.5 %. Because the requirement of shutting in the injection well is not necessary along with the straight forward method, this active monitoring technique has the potential to be deployed as a long-term cost-effective alternative to monitor the CO<sub>2</sub> plume.

## **Chapter 5: Linear Composite Model with Harmonic Pulse Testing**

### **5.1 Introduction**

Harmonic Pulse Testing (HPT) is a well testing method in which the injection or production rate fluctuates in a periodic manner. The pressure response obtained in the field from the pulser well and the observation wells can be converted from the time domain to the frequency domain by Fourier Transform. The amplitude and phase spectrum obtained from the pressure response in frequency domain can then be used to evaluate the reservoir properties such as storativity and transmissivity. Given HPT sensitivity to storativity and transmissivity, the possibility to characterize CO<sub>2</sub> plume for implementation in ongoing and future carbon storage projects is explored by use of Frequency Domain Analysis. Frequency Domain Analysis has been used since the early 1950's for filtering out undesired bands of frequencies (Zaded 1953). Frequency Domain Analysis has a diverse variety of applications such as nuclear magnetic resonance measurements, electric power systems, and brain cancer detection (Hein, Larsen, and Parsekian 2017, Yuan et al. 2017, Mazhari, Montaser Kouhsari, and Ramirez 2017). Pressure Transient Analysis in the frequency domain has already been investigated to determine the permeability distribution in a reservoir (Ahn and Horne 2011, 2010). Research has also been conducted for Frequency Domain Analysis to detect CO<sub>2</sub> leakage (Shakiba and Hosseini 2016, Sun et al. 2016). These studies have focused on early detection of CO<sub>2</sub> leakage in a leaky well and using a network of observation wells for CO<sub>2</sub> characterization.

We borrow the model from Chapter 2 and develop an analytical solution for the three-region linear composite system which is used to estimate the location and size of CO<sub>2</sub> between an observation

well, and an activation well. This method differs from chapter 2 by not utilizing the influence time which can differ depending on gauge resolution. Instead the pressure injection and observation well pressure data are converted and analyzed together and separately in the frequency domain in hope to characterize the CO<sub>2</sub> plume. Synthetic frequency response is created using numerical simulation to model the HPT in a reservoir where CO<sub>2</sub> has been injected for storage. This chapter will focus on the development of the analytical model and the match obtained with a homogenous system which will be continued to fully characterize a CO<sub>2</sub> plume.

## 5.2 Overview of Pressure Pulse Processing

Given the pressure pairs measured from the active and monitoring wells for a linear 3-region composite model, we estimate the plume extent and location relative to either wells. The procedure composes of two parts: (1) pressure data preprocessing to obtain the frequency components and (2) the inverse problem of matching the attenuation data at multiple frequencies. Typically phase shift and attenuation can be obtained from the pressure pairs, but for this study we focus on the attenuation obtained from the pressure pair, and the magnitude of the individual wells. Because the injection well is sourced with a square pulse, applying a discrete fourier transform on the data set such as the Fast Fourier Transform (FFT) will extract information regarding the magnitude and the attenuation at harmonic of the fundamental frequency. Properties of both regions (water and CO<sub>2</sub>) are assumed to be known leaving the only unknowns to be the extent of and location of region 2.

## 5.3 Methodology

To use the model from Chapter 2 for periodic pulse testing, the sinusoidal steady-state assumption has to be applied to flow rate and pressure as being periodic such as:

$$p_D(x_D, y_D, t_D) = g_D(x_D, y_D)e^{i\omega_D t_D} \quad (5.1)$$

$$q = Q_0 e^{i\omega_D t_D} \quad (5.2)$$

Where the dimensionless frequency of periodic pulses,  $\omega_D$ , is defined as  $\frac{\phi\mu c_t d^2 \omega}{k}$  with  $\omega = \frac{2\pi}{T_p}$ . To determine what output is needed from the analytical solution, let  $P_{inj}$  and  $P_{obs}$ , pressures from the injection and observation wells in Regions 1 and 3 respectively (Figure 2.2), represent the pressure responses obtained from the injector and an observation well. With the impulse response function denoted as  $h(t)$ , the impulse-response relationship of the reservoir is given by the convolution integral.

$$P_{obs} = \int_0^t P_{inj}(t - \tau)h(\tau)d\tau \quad (5.3)$$

The convolution theorem states that under suitable conditions, the Fourier transform of a convolution is the pointwise product of Fourier transforms. In general, the convolution in Equation 5.3, in the frequency domain becomes:

$$P_{obs}(\omega) = P_{inj}(\omega)H(\omega) \quad (5.4)$$

Where  $H(\omega)$  is defined as the transfer function which represents the reservoir properties, in our case, the CO<sub>2</sub> location and extent. Now with the goal of having a solution in the form of Equation 5.4, we can develop an analytical solution that replaces the interpretation with respect to time.

## 5.4 Analytical Solution

The assumptions and boundary conditions for the linear composite model are the same as those in chapter 2, with the addition of periodic steady state meaning the pressure at a given time is the same at every period after that time. Pre-processing the pressure data by detrending is necessary to hold that assumption when analyzing the output from the injection and monitoring wells. Taking the governing equations from Chapter 2 and replacing the rate with the sinusoidal steady state assumptions of Equations 5.2 and 5.3, a new set of governing equations are derived for Regions 5.1, 5.2, and 5.3 in dimensionless form.

$$\frac{\partial^2 g_{D1}}{\partial x_D^2} + \frac{\partial^2 g_{D1}}{\partial y_D^2} + \delta(x_D - a_D) \delta(y_D) = i\omega_D g_{D1} \quad (5.5)$$

$$\frac{\partial^2 g_{D2}}{\partial x_D^2} + \frac{\partial^2 g_{D2}}{\partial y_D^2} = i\omega_D g_{D2} \quad (5.6)$$

$$\frac{\partial^2 g_{D3}}{\partial x_D^2} + \frac{\partial^2 g_{D3}}{\partial y_D^2} = i\omega_D g_{D3} \quad (5.7)$$

Unlike the previous chapter where the Laplace Transform and the Fourier Transform were applied, we have already eliminated the time variable, thus only the Fourier Transform is applied with respect to the  $y$ -direction. The spatial Fourier transform is defined as:

$$g_D(x_D, \xi, \omega) = \mathcal{F}\{g_D(x_D, y_D, \omega)\} = \int_{-\infty}^{\infty} g_D(x_D, y'_D, \omega) e^{i\xi y'_D} dy'_D \quad (5.8)$$

Applying the Fourier transform to the governing Equations 5.5, 5.6, and 5.7, we arrive at new set of equations to solve simultaneously:

$$g''_{D1} - (\xi^2 + i\omega)g_{D1} = \delta(x_D - a_D) \quad (5.9)$$

$$g''_{D2} - (\xi^2 + \frac{C}{M}i\omega)g_{D2} = 0 \quad (5.10)$$

$$g''_{D3} - (\xi^2 + i\omega)g_{D3} = 0 \quad (5.11)$$

Solving for Equations 5.9, 5.10, and 5.11 yields the following final solution for the pressure response in Regions 5.1, 5.2, and 5.3 respectively.

$$g_{D1} = \frac{e^{-A(a_D + x_D)} \left( \frac{e^{2Ab_D}(A^{0.5} - B^{0.5}M^2)}{M(A^{0.75}B(e^{2Bb_D} + 1) + B^{0.5}M)} + (e^{2Aa_D} - e^{2Ax_D})\theta(x_D - a_D) + e^{2Ax_D} \right)}{2A} \quad (5.12)$$

$$g_{D2} = \frac{(e^{2Bx_D}(A + BM) - A + BM)e^{-Aa_D + Ab_D - Bx_D}}{2((A^{0.5} + B^{0.5}M^2)\sinh(Bb_D) + 2ABM\cosh(Bb_D))} \quad (5.13)$$

$$g_{D3} = \frac{2BMe^{A(-a_D + b_D + x_D) + Bb_D}}{A^{0.5}(M^2 + 1)(e^{2Bb_D} - 1) + 2ABM(e^{2Bb_D} + 1)} \quad (5.14)$$



Where  $A = \sqrt{\xi^2 + i\omega_b}$  and  $B = \sqrt{\xi^2 + \frac{C}{M}i\omega_b}$ . The amplitude is defined as the magnitude of the individual pressure response from the well in the frequency domain,  $|g_D|$ . The attenuation is defined as the ratio of the magnitudes.

$$|H(\omega)| = \frac{|P_{obs}(\omega)|}{|P_{inj}(\omega)|} = \frac{|g_{D3}|}{|g_{D1}|} \quad (5.15)$$

$$= \frac{4ABMe^{b_D(A+B)+2Ax_D}}{(A^{0.5}(M^2+1)(e^{2Bb_D}-1) + 2ABM(e^{2Bb_D}+1))\left(\frac{e^{2Ab_D}(A^{0.5}-B^{0.5}M^2)}{M(A^{0.75}B(e^{2Bb_D}+1)+B^{0.5}M)} + (e^{2Aa_D}-e^{2Ax_D})\theta(x_D-a_D) + e^{2Ax_D}\right)}$$

Similar to chapter 2, we will be using equation 5.15 to estimate parameters  $b_D$ , the thickness of the CO<sub>2</sub> but unlike chapter 2, we intend to identify the location of the plume,  $a_D$ . Although there are two unknowns and only one equation, we explore the possibility of using individual wells. In chapter 2, results showed that the pressure response in the observation well was independent of the location of region 2, thus identifying the plume boundaries was not possible. This is not the case for the injection well where the pressure response depends on both the plume location and size. We can use this information to individually match the frequency response of each well. The observation well will be used to estimate the extent,  $b_D$ , which will later be used as an input parameter for equation 5.12 to determine the location of the plume boundary.

### 5.5 Match for Homogenous Case

Reservoir parameters and fluid properties used for the numerical simulation are the same as those in Chapter 2 (Section 2.5). The main purpose of this section is to match the analytical model to the homogenous case and discuss problems that arise when CO<sub>2</sub> is introduced into the system. The first step is to match the individual observation and injection well magnitudes with the numerical simulator. Both the injection and observation wells for the numerical simulator showed a smaller amplitude when compared to the analytical solution as seen in Figures 5.1 and 5.2.

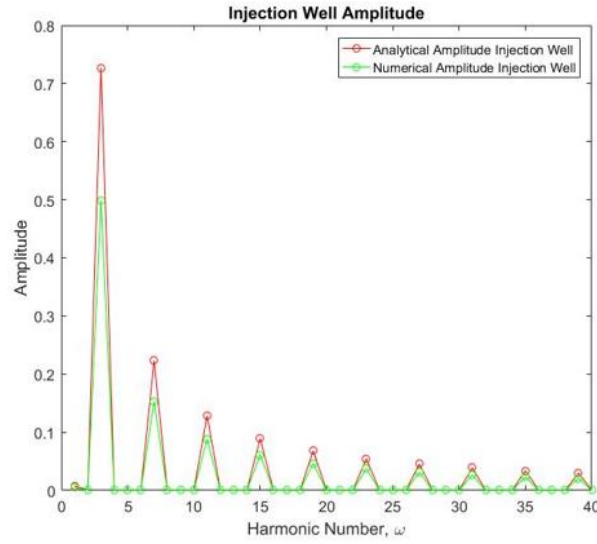


Figure 5.1. Mismatched amplitude for injection well

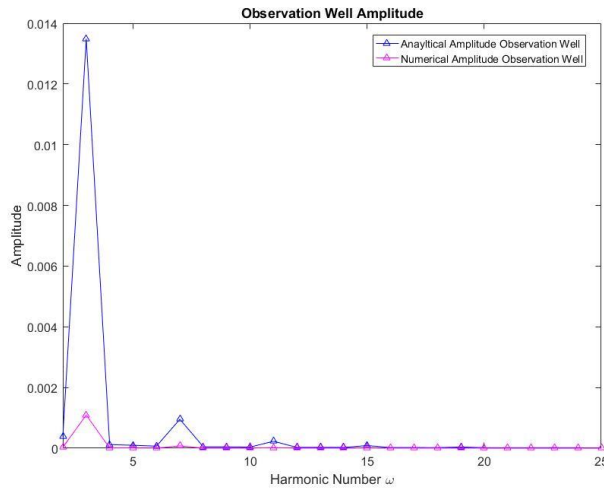


Figure 5.2. Mismatched amplitude for observation well

Upon further investigation, the attenuation, which is the ratio of the amplitudes, was found to be a perfect match as seen in Figure 5.3. Upon this finding, a hypothesis of why the attenuation matched but not the individual wells was composed. When processing the data obtained from the numerical simulator using Fast Fourier Transform (FFT), the output scale could be different from the analytical solution. A method was developed to scale both the analytical solution and numerical simulator. The simple method was to scale the amplitude corresponding to the first frequency, also

called the Sourcing Frequency, to 1. When this is done a perfect match for individual wells is obtained as seen in Figures 5.4 and 5.5 for the injection and observation well respectively.

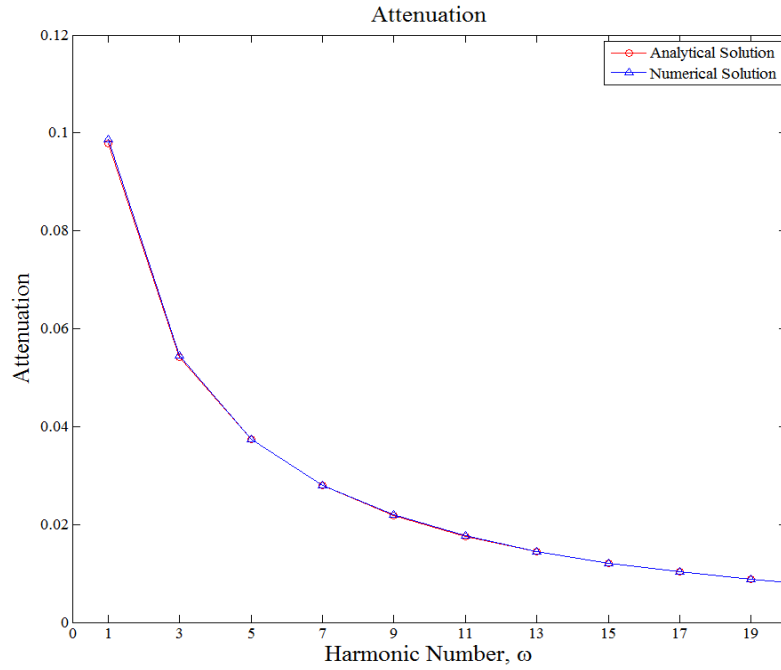


Figure 5.3. Very good match of the ratios (attenuation) from Figures 5.1 and 5.2.

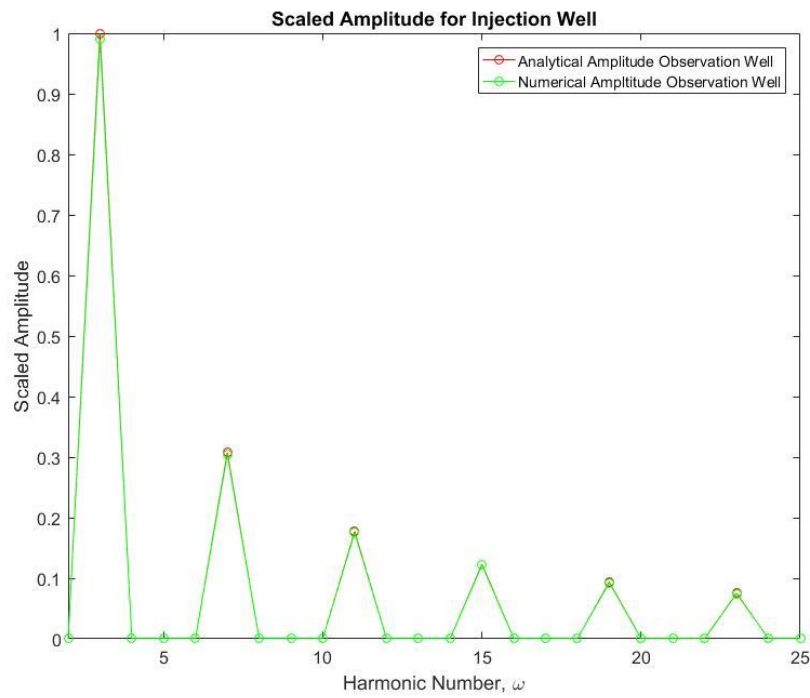


Figure 5.4. Good match of the scaled amplitude for the injection well

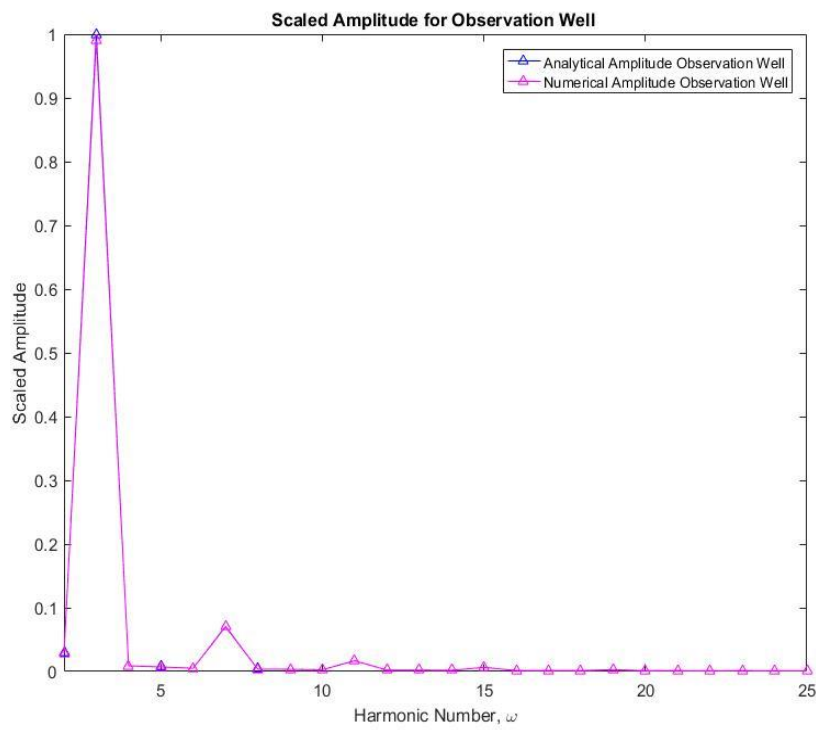


Figure 5.5. Good match of the scaled amplitude for the observation well

Following a satisfactory match, further investigation is done into recreating pressure response curves in time domain from the frequency domain data. The equation which related time domain pressure to frequency domain below was used to return to the time domain.

$$p_D = \text{Im}(\sum_{k=1,3,5\dots}^n \frac{1}{k} g(r, \omega) e^{i\omega_k t}) \quad (5.16)$$

The reason why only odd harmonics are taken is due to the impulse that was created by a square wave injection scheme. If the injection is not a square wave, e.g. a rectangle or saw-toothed, appropriate harmonics must be taken. The pressure in time domain corresponds to the imaginary part of the above equation because the square wave corresponds to a *sin* graph. By using Euler's equation  $e^{i\omega t} = \cos(\omega t) + i\sin(\omega t)$ , the imaginary component corresponds to the *sin* part of the equation. If pressure data was taken with a shift which turns the pressure data into a *cos* graph, the pressure in time domain would correspond to the real part of Equation 5.14. After taking the pressure data from frequency domain back into the pressure form in time domain, a very good match was observed for both active and monitoring wells as seen in Figures 5.6 and 5.7 respectively. There is a slight mismatch in the first period, most noticeably in the observation well, but this may be due to pre-processing error when detrending the data.

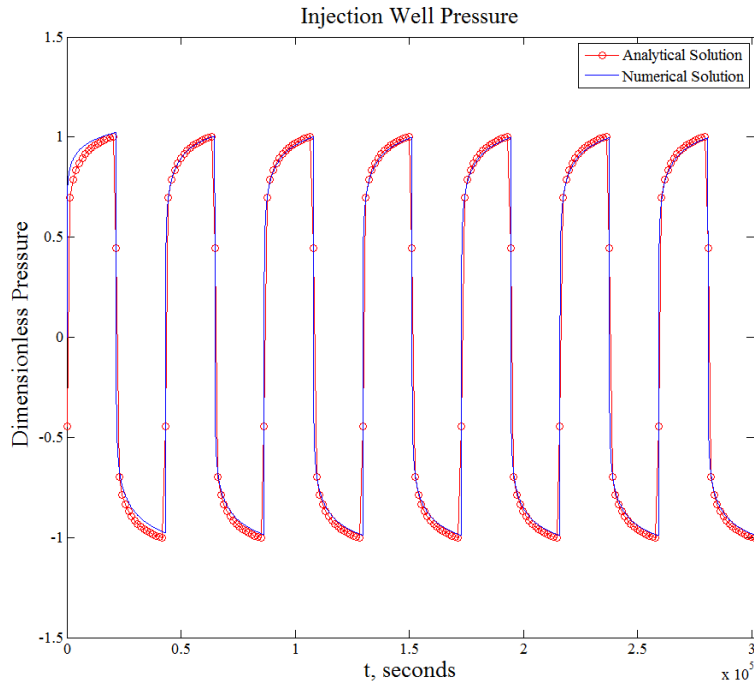


Figure 5.6. Pressure history match going from frequency domain back to the time domain. A very good agreement is seen here for the injection well.

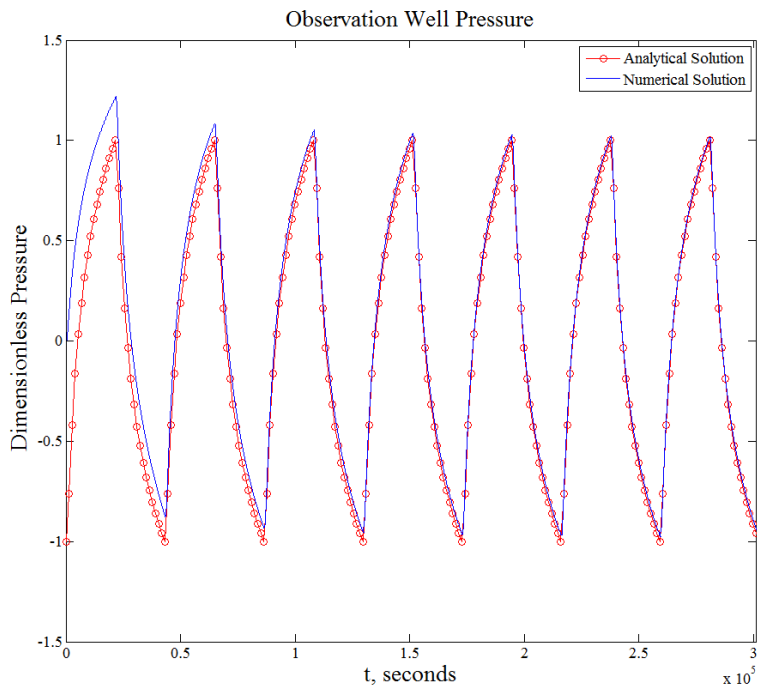


Figure 5.7. Pressure history match going from frequency domain back to the time domain. A very good agreement is seen here for the observation well aside from the first harmonic. This may be due to the inability to remove all the pressure transient trend.

## 5.6 Discussion and Further Work

For the homogenous case, a very good match was obtained for both frequency and time domain pressure signals. There are three main problems in which, if this work is continued, must be solved. The first problem is getting a match where there is  $\text{CO}_2$  in the system. There is a very strong agreement in the homogenous system because everything is assumed to be infinite acting. As seen in Chapter 4, when there is a plume, the pressure diagnostic shows a no flow boundary behavior. Where this is even more drastic in the model for Chapter 5 because the  $\text{CO}_2$  is pure gaseous phase with no mixture of water. The pressure front may see the pure  $\text{CO}_2$  as a temporary boundary which should be handled when deriving the analytical solution. The second problem is converting the pure gas in Region 2 into something realistic. This can be done by appropriate scaling and utilizing techniques from chapter 3 which estimates the average gas saturation. For example, it may be possible to translate a pure  $\text{CO}_2$  zone that is 100 m thick, to a  $\text{CO}_2$  plume that has average gas saturation of 50% but 200 meters thick. The third problem is determining how the period should be for each harmonic which depends on the size of the plume and location of the observation well. For pure  $\text{CO}_2$  that was 100 m thick with an observation well location 300 meters from the injection well, it took approximately 1-day periods. Although this may not seem like a problem and is still a better option for the monitoring of permanent  $\text{CO}_2$  storage zones, when it comes to other applications such as water flooding or  $\text{CO}_2$  flooding, this may not be the case. Sourcing rectangle pulses or even triangle pulses may also work better to address this problem. My goal was to provide a ground work for the first analytical solution of a 2D-Cartesian system in the frequency domain that can be improved upon with further studies and even be applied to different applications outside of  $\text{CO}_2$  sequestration.

## **Chapter 6: Discussion and Main Conclusions**

A variety of pressure transient analysis techniques were conducted to obtain gas plume properties such as the average saturation, location of boundaries, and the extent. First, we developed an analytical model for a linear 3 region composite model for constant rate injection test. We defined and inverted the influence time to determine characteristics of the CO<sub>2</sub> plume. After applying the method to the model, we developed a numerical simulation to apply the tool to a realistic plume shape. In Chapter 3, pressure arrival time and corresponding 2-phase diffusivity equation were utilized to determine the average gas saturation of the plume with the possibility of accurately determining the boundary if multiple observation points are available inside and outside the plume. The forth chapter treated the plume as a constant pressure boundary, and through the super position principle, a model was developed to determine the location of the CO<sub>2</sub> boundary using single well test pressure diagnostic plots. For the fifth chapter, we revisited chapter 2, and redeveloped the analytical solution for periodic pressure sinusoidal steady state. This chapter was only the start of the work, with recommendations on how to move forward.

The main conclusions of this thesis are:

Chapter 2: Through analytical modelling confirmed with multiple numerical simulations, it was determined that the pressure influence time (the time at which the pressure change at the observation well attains the gauge resolution) is independent of the plume shape while only depending on the plume extent. By using this relationship, we inverted the influence time to estimate the plume extent and applied this tool to realistic plumes generated by numerical simulations. The main drawback is the need for high resolution gauges with results becoming inaccurate for poor resolution.



Chapter 3: By using interference well testing, average gas saturation can be accurately estimated. This is done by utilizing a two-phase diffusivity coefficient, and line source integral evaluation. With the use of multiple wells, the location of the boundary can be determined.

Chapter 4: We introduce a pressure transient test at a distant well from the CO<sub>2</sub> injection well to determine the plume boundary relative to the distant well at any given time. The test used for the study is constant rate injection but constant rate production may also be used. By observing the pressure diagnostic plot, the time at which the zero-slope line deviates from the radial flow due to the high mobile gas was used to relate to the location of the plumes' boundary. This is an active monitoring technique, meaning that shutting in the CO<sub>2</sub> injection well while running the test is not necessary. While this technique is useful to estimating one boundary, the true strengths are when there are multiple wells surrounding the CO<sub>2</sub> injection well which can thus provide an accurate depiction of the CO<sub>2</sub> front.

Chapter 5: Chapter 2 is revisited to solve problems the original analytical model could not handle such as: location of the well, and the non-dependency on gauge resolution. This was done by creating the ground work for the analytical solution in the frequency domain for the simplest case of a homogeneous system. Upon arrival of the analytical solution, the separate wells' magnitude did not match, but the ratios of the magnitude (attenuation) provided a strong match. Upon further investigation, when processing the data from the numerical simulator using Fourier Transform, the scale was different from the analytical solution. To solve this problem, a simple technique was implemented to scale both the data and analytical solution to easily compare them. After this was done, a strong match was achieved. After achieving the individual matches, we investigate the possibility of going back into the time domain to pressure history match. After achieving a strong match in the time domain, we discussed what should be done to complete this

problem which includes correcting the analytical solution to take into account for region 2's boundary, optimization of injection/shut in periods, and best shapes (outside the square pulse flow rate) that can allow for best pressure signal at the observation well.

## References

- Agarwal, Ram G. 1980. A New Method To Account For Producing Time Effects When Drawdown Type Curves Are Used To Analyze Pressure Buildup And Other Test Data. Proc.
- Ahn, Sanghui, Roland N. Horne. 2010. Estimating Permeability Distributions From Pressure Pulse Testing. Proc.
- Ahn, Sanghui, Roland N. Horne. 2011. The Use of Attenuation and Phase Shift to Estimate Permeability Distributions from Pulse Tests. Proc.
- Alfi, Masoud, Seyyed A. Hosseini, Mehrdad Alfi et al. 2015. Effectiveness of 4D Seismic Data to Monitor CO2 Plume in Cranfield CO2-EOR Project. Proc.
- Azizi, Ehsan, Yildiray Cinar. 2013. Approximate analytical solutions for CO2 injectivity into saline formations. *SPE Reservoir Evaluation & Engineering* **16** (02): 123-133.
- Bear, J. 1972. *Dynamics of Fluids in Porous Media*. New York, Elsevier (Reprint).
- Bergmann, P., M. Diersch, J. Gotz et al. 2016. Review on geophysical monitoring of CO2 injection at Ketzin, Germany (in English). *Journal of Petroleum Science and Engineering* **139**: 112-136. <Go to ISI>://WOS:000370718300011.
- Birkholzer, Jens T., Quanlin Zhou. 2009. Basin-scale hydrogeologic impacts of CO2 storage: Capacity and regulatory implications. *International Journal of Greenhouse Gas Control* **3** (6): 745-756.
- Bixel, H. C. , B. K. Larkin, van Poolen H. K. 1963. Effect of linear discontinuities on pressure build-up and drawdown behavior. *Journal of Petroleum Technology* **15** (8): 885-895.
- Bohm, G., J. M. Carcione, D. Gei et al. 2015. Cross-well seismic and electromagnetic tomography for CO2 detection and monitoring in a saline aquifer (in English). *Journal of Petroleum Science and Engineering* **133**: 245-257. <Go to ISI>://WOS:000365253300026.

- Bruggeman, GA. 1972. The reciprocity principle in flow through heterogeneous porous media. *IN: FUNDAMENTALS OF TRANSPORT PHENOMENA IN POROUS MEDIA*.
- Carcione, J. M., D. Gei, S. Picotti et al. 2012. Cross-hole electromagnetic and seismic modeling for CO2 detection and monitoring in a saline aquifer (in English). *Journal of Petroleum Science and Engineering* **100**: 162-172. <Go to ISI>://WOS:000315311400019.
- Carrigan, Charles R., Xianjin Yang, Douglas J. LaBrecque et al. 2013. Electrical resistance tomographic monitoring of CO2 movement in deep geologic reservoirs. *International Journal of Greenhouse Gas Control* **18**: 401-408.
- Chabora, Ethan R., Sally M. Benson. 2009. Brine Displacement and Leakage Detection Using Pressure Measurements in Aquifers Overlying CO2 Storage Reservoirs. *Energy Procedia* **1** (1): 2405-2412. <http://www.sciencedirect.com/science/article/pii/S1876610209003142>.
- Chadwick, RA , R Arts, O Eiken. 2005. 4D seismic quantification of a growing CO2 plume at Sleipner, North Sea. *Pet. Geol. Conf. series* **6**: 1385-99.
- Chen, C. C., Wei-Chun Chu, Soleiman Sadighi. 1996. Pressure-Transient Testing of Gas Reservoirs With Edge-Waterdrive.
- CMG-GEM. CMG-GEM Version 2013 user's guide. Computer Modelling Group Ltd., <http://www.cmgl.ca/software/gem.htm>.
- CMG-GEM. Computer Modelling Group CMG-GEM Version 2015 user's guide. Computer Modelling Group Ltd., <http://www.cmgl.ca/software/gem.htm>.
- CMG-IMEX. CMG-IMEX Version 2015 user's guide. Computer Modelling Group Ltd., <http://www.cmgl.ca/software/gem.htm>.
- Cooley, James W, John W Tukey. 1965. An algorithm for the machine calculation of complex Fourier series. *Mathematics of computation* **19** (90): 297-301.
- Corey, Arthur T. 1954. The interrelation between gas and oil relative permeabilities. *Producers monthly* **19** (1): 38-41.
- Couëslan, Marcia L., Valerie Smith, George El-Kaseeh et al. 2014. Development and implementation of a seismic characterization and CO2 monitoring program for the Illinois Basin – Decatur Project. *Greenhouse Gases: Science and Technology* **4** (5): 626-644. <http://dx.doi.org/10.1002/ghg.1452>.

- Court, B., T. R. Elliot, J. Dammel et al. 2012. Promising synergies to address water, sequestration, legal, and public acceptance issues associated with large-scale implementation of CO<sub>2</sub> sequestration (in English). *Mitigation and Adaptation Strategies for Global Change* **17** (6): 569-599. <Go to ISI>://WOS:000305985200002
- Ettehadtavakkol, Amin, Larry W. Lake, Steven L. Bryant. 2014. Impact of Storage Tax Credit on Economic Viability of CO<sub>2</sub> Storage with EOR. Proc.
- Falade, GK, WE Brigham. 1979. The Reciprocity Principle in Fluid Flow Through Porous Media. *Society of Petroleum Engineers Journal* **19** (04): 200-202.
- Fenghour, W., Wakeham, A., Vesovic, V. 1998. The viscosity of carbon dioxide. *J. Phys. Chem.:* 31-44.
- Fokker, Peter A., Joerg Renner, Francesca Verga. 2012. Applications of Harmonic Pulse Testing to Field Cases. Proc.
- Haghighat, S. A., S. D. Mohaghegh, V. Gholami et al. Pressure History Matching for CO<sub>2</sub> Storage in Saline Aquifers: Case Study for Citronelle Dome. *Alexandria, Virginia*.
- Hein, Annette, Jakob Juul Larsen, Andrew D. Parsekian. 2017. Symmetry based frequency domain processing to remove harmonic noise from surface nuclear magnetic resonance measurements. *Geophysical Journal International* **208** (2): 724-736.  
<http://dx.doi.org/10.1093/gji/ggw433>.
- Hosseini, Seyyed A., Masoud Alfi. 2015. Time-lapse application of pressure transient analysis for monitoring compressible fluid leakage. *Greenhouse Gases: Science and Technology*: n/a-n/a. <http://dx.doi.org/10.1002/ghg.1570>.
- Hosseini, Seyyed A., Masoud Alfi. 2016. Time-lapse application of pressure transient analysis for monitoring compressible fluid leakage. *Greenhouse Gases: Science and Technology* **6** (3): 352-369. <http://dx.doi.org/10.1002/ghg.1570>.
- Hovorka, Susan D., Timothy A. Meckel, Ramón H. Treviño. 2013. Monitoring a large-volume injection at Cranfield, Mississippi—Project design and recommendations. *International Journal of Greenhouse Gas Control* (0).  
<http://www.sciencedirect.com/science/article/pii/S1750583613001527>.

- Hu, L. W., P. Bayer, P. Alt-Epping et al. 2015a. Time-lapse pressure tomography for characterizing CO<sub>2</sub> plume evolution in a deep saline aquifer (in English). *International Journal of Greenhouse Gas Control* **39**: 91-106. <Go to ISI>://WOS:000358627100009.
- Hu, Linwei. 2017. Characterization of CO<sub>2</sub> plumes in deep saline formations using fluid pressure tomography.
- Hu, Linwei, Peter Bayer, Peter Alt-Epping et al. 2015b. Time-lapse pressure tomography for characterizing CO<sub>2</sub> plume evolution in a deep saline aquifer. *International Journal of Greenhouse Gas Control* **39**: 91-106.  
<http://dx.doi.org/10.1016/j.ijggc.2015.04.013>.
- Hu, Linwei, Peter Bayer, Ralf Brauchler. 2016. Detection of carbon dioxide leakage during injection in deep saline formations by pressure tomography. *Water Resources Research*.
- Hu, Linwei, Joseph Doetsch, Ralf Brauchler et al. 2017. Characterizing CO<sub>2</sub> plumes in deep saline formations: comparison and joint evaluation of time-lapse pressure and seismic tomography. *Geophysics* **82** (4): ID1-ID18.
- IPCC. 2005. Intergovernmental Panel on Climate Change, Special Report on Carbon Dioxide Capture and Storage.
- Johnson, C. R., R. A. Greenkorn, E. G. Woods. 1966. Pulse-testing: a new method for describing reservoir flow properties between wells. *Journal of Petroleum Transactions*.  
<http://www.onepetro.org/journal-paper/SPE-1517-PA>.
- Jung, Y. J., Q. L. Zhou, J. T. Birkholzer. 2013. Early detection of brine and CO<sub>2</sub> leakage through abandoned wells using pressure and surface-deformation monitoring data: Concept and demonstration (in English). *Advances in Water Resources* **62**: 555-569. <Go to ISI>://WOS:000327540600017.
- Kamal, M. M. 1983. Interference and Pulse Testing - A Review. (December).
- Kampman, N., M. J. Bickle, A. Maskell et al. 2014. Drilling and sampling a natural CO<sub>2</sub> reservoir: Implications for fluid flow and CO<sub>2</sub>-fluid-rock reactions during CO<sub>2</sub> migration through the overburden. *Chemical Geology* **369**: 51-82.
- Kampman, Niko, Mike Bickle, Max Wigley et al. 2014. Fluid flow and CO<sub>2</sub>-fluid-mineral interactions during CO<sub>2</sub>-storage in sedimentary basins. *Chemical Geology* **369**: 22-50.

- Kempka, Thomas, Michael Kühn. 2013. Numerical simulations of CO<sub>2</sub> arrival times and reservoir pressure coincide with observations from the Ketzin pilot site, Germany. *Environmental earth sciences* **70** (8): 3675-3685.
- Koperna, George J. . Anthropogenic Test Simulation Results *Austin, TX*.
- Kreyszig, E. 2011. *Advanced Engineering Mathematics*. New York, Wiley, 10th edition (Reprint).
- Kuchuk, F. 2009. Radius of Investigation for Reserve Estimation From Pressure Transient Well Tests. Proc.
- Kuo, C. H. 1972. Determination of Reservoir Properties from Sinusoidal and Multirate Flow Tests in One or More Wells.
- Lee, J., J.B. Rollins, J.P. Spivey. 2003. *Pressure transient testing*, 376, SPE Textbook Series, Vol. 9, Society of Petroleum Engineers (Reprint).
- Liebscher, Axel, Fabian Möller, Andreas Bannach et al. 2013. Injection operation and operational pressure–temperature monitoring at the CO<sub>2</sub> storage pilot site Ketzin, Germany—Design, results, recommendations. *International Journal of Greenhouse Gas Control* **15** (0): 163-173.  
<http://www.sciencedirect.com/science/article/pii/S1750583613001138>
- [http://ac.els-cdn.com/S1750583613001138/1-s2.0-S1750583613001138-main.pdf?\\_tid=4e2d9f74-cc92-11e2-92db-00000aacb361&acdnat=1370294132\\_e4b20260713591c0882dc6220c17ff49](http://ac.els-cdn.com/S1750583613001138/1-s2.0-S1750583613001138-main.pdf?_tid=4e2d9f74-cc92-11e2-92db-00000aacb361&acdnat=1370294132_e4b20260713591c0882dc6220c17ff49).
- Little, Mark G, Robert B Jackson. 2010. Potential impacts of leakage from deep CO<sub>2</sub> geosequestration on overlying freshwater aquifers. *Environmental science & technology* **44** (23): 9225-9232.
- MacMinn, Christopher W., Ruben Juanes. 2009. A mathematical model of the footprint of the CO<sub>2</sub> plume during and after injection in deep saline aquifer systems. *Energy Procedia* **1** (1): 3429-3436. <http://www.sciencedirect.com/science/article/pii/S1876610209007760>.
- Mathias, S. A., G. J. G. M. de Miguel, K. E. Thatcher et al. 2011. Pressure Buildup During CO<sub>2</sub> Injection into a Closed Brine Aquifer (in English). *Transport in Porous Media* **89** (3): 383-397. <Go to ISI>://WOS:000295589400006

<http://link.springer.com/content/pdf/10.1007%2Fs11242-011-9776-z.pdf>.

Mathias, S. A., P. E. Hardisty, M. R. Trudell et al. 2009. Approximate Solutions for Pressure Buildup During CO<sub>2</sub> Injection in Brine Aquifers (in English). *Transport in Porous Media* **79** (2): 265-284. <Go to ISI>://000268548900008.

Mazhari, Seyed Mahdi, Shahram Montaser Kouhsari, Abner Ramirez. 2017. A novel frequency-domain approach for distributed harmonic analysis of multi-area interconnected power systems. *Electric Power Systems Research* **143**: 669-681.  
<http://www.sciencedirect.com/science/article/pii/S037877961630445X>.

Meckel, T. A., M. Zeidouni, S. D. Hovorka et al. 2013. Assessing sensitivity to well leakage from three years of continuous reservoir pressure monitoring during CO<sub>2</sub> injection at Cranfield, MS, USA. *International Journal of Greenhouse Gas Control* **18** (0): 439-448.  
<http://www.sciencedirect.com/science/article/pii/S1750583613000352>.

Mosaheb, Mojtaba, Mehdi Zeidouni. 2017a. Above-Zone Pressure Response to Distinguish Between Fault and Caprock Leakage. Proc., 2017 Western Regional Meeting, Bakersfield, California, USA.

Mosaheb, Mojtaba, Mehdi Zeidouni. 2017b. Pressure Transient Analysis for Leaky Well Characterization and its Identification From Leaky Fault. Proc., SPE Health, Safety, Security, Environment, & Social Responsibility Conference - North America, New Orleans, Louisiana, USA.

Nelson, Charles R. Factors Affecting the Potential for Co<sub>2</sub> Leakage from Geologic Sinks.

Nunez-Lopez, Vanessa, Javier Muñoz-Torres, Mehdi Zeidouni. Temperature monitoring using distributed temperature sensing (DTS) technology. *Austin, TX*.

Petrusak, Robin L. , Shawna Cyphers, Stephen B. Bumgardner et al. Saline Reservoir Storage in an Active Oil Field: Extracting Maximum Value From Existing Data for Initial Site Characterization; Southeast Regional Carbon Sequestration Partnership (SECARB) Phase III. *New Orleans, LA*.

Redlich, Otto, Joseph NS Kwong. 1949. On the thermodynamics of solutions. V. An equation of state. Fugacities of gaseous solutions. *Chemical reviews* **44** (1): 233-244.



- Rohmer, Jeremy, Olivier Bouc. 2010. A response surface methodology to address uncertainties in cap rock failure assessment for CO<sub>2</sub> geological storage in deep aquifers. *International Journal of Greenhouse Gas Control* **4** (2): 198-208. <http://dx.doi.org/10.1016/j.ijggc.2009.12.001>.
- Shakiba, Mahmood, Seyyed A. Hosseini. 2016. Detection and characterization of CO<sub>2</sub> leakage by multi-well pulse testing and diffusivity tomography maps. *International Journal of Greenhouse Gas Control* **54**: 15-28. <http://linkinghub.elsevier.com/retrieve/pii/S1750583616304972>.
- Shepard, Donald. 1968. A two-dimensional interpolation function for irregularly-spaced data. Proc., Proceedings of the 1968 23rd ACM national conference, 517-524.
- Shitashima, Kiminori, Yoshiaki Maeda, Takashi Ohsumi. 2013. Strategies for detection and monitoring of CO<sub>2</sub> leakage in sub-seabed CCS. *Energy Procedia* **37**: 4283-4290.
- Spivey, John P., W. John Lee. 2013. *Applied Well Test Interpretation*, Vol. 13, SPE Textbook Series (Reprint).
- Stehfest, H. . 1970. Algorithm 368 numerical inversion of Laplace transforms. D-5. *Commun. ACM* **13** (1): 47-49.
- Strandli, C. W., S. M. Benson. 2013. Identifying diagnostics for reservoir structure and CO<sub>2</sub> plume migration from multilevel pressure measurements (in English). *Water Resources Research* **49** (6): 3462-3475. <Go to ISI>://WOS:000322241300026  
<http://onlinelibrary.wiley.com/store/10.1002/wrcr.20285/asset/wrcr20285.pdf?v=1&t=hpn5393p&s=23df580bf4b80c9ae3713b314e1634cc0b48919e>.
- Sun, A. Y., J. M. Lu, S. Hovorka. 2015. A harmonic pulse testing method for leakage detection in deep subsurface storage formations (in English). *Water Resources Research* **51** (6): 4263-4281. <Go to ISI>://WOS:000358301200021.
- Sun, Alexander Y., Jiemin Lu, Barry M. Freifeld et al. 2016. Using pulse testing for leakage detection in carbon storage reservoirs: A field demonstration. *International Journal of Greenhouse Gas Control* **46**: 215-227. <http://dx.doi.org/10.1016/j.ijggc.2016.01.015>.
- Sun, Alexander Y., Mehdi Zeidouni, Jean-Philippe Nicot et al. 2013. Assessing leakage detectability at geologic CO<sub>2</sub> sequestration sites using the probabilistic collocation

- method. *Advances in Water Resources* **56** (0): 49-60.  
<http://www.sciencedirect.com/science/article/pii/S0309170812002990>.
- Theis, C.V. 1935. The relation between the lowering of the piezometric surface and rate and duration of discharge of a well using ground water storage. *Trans. AGU* **16**: 519-524.
- Tran, Nam H., Mehdi Zeidouni. 2017. CO<sub>2</sub> Plume Characterization Using Pressure Arrival Time. *Proc.*
- van der Meer, L. G. H., Ferhat Yavuz. 2009. CO<sub>2</sub> storage capacity calculations for the Dutch subsurface. *Energy Procedia* **1** (1): 2615-2622.
- van Genuchten, M Th. 1980. A closed-form equation for predicting the hydraulic conductivity of unsaturated soils. *Soil science society of America journal* **44** (5): 892-898.
- Wandrey, Maren, Sebastian Fischer, Kornelia Zemke et al. 2011. Monitoring petrophysical, mineralogical, geochemical and microbiological effects of CO<sub>2</sub> exposure—Results of long-term experiments under in situ conditions. *Energy Procedia* **4**: 3644-3650.
- Wang, Zan, Mitchell J Small. 2014. A Bayesian approach to CO<sub>2</sub> leakage detection at saline sequestration sites using pressure measurements. *International Journal of Greenhouse Gas Control* **30**: 188-196.
- Yuan, Wu, Carmen Kut, Wenxuan Liang et al. 2017. Robust and fast characterization of OCT-based optical attenuation using a novel frequency-domain algorithm for brain cancer detection. *Scientific Reports* **7**: 44909. <http://dx.doi.org/10.1038/srep44909>.
- Zaded, L. A. 1953. Theory of Filtering. *Journal of the Society for Industrial and Applied Mathematics* **1** (1).
- Zeidouni, Mehdi. 2014. Analytical model of well leakage pressure perturbations in a closed aquifer system. *Advances in Water Resources* **69** (0): 13-22.  
<http://www.sciencedirect.com/science/article/pii/S0309170814000499>  
[http://ac.els-cdn.com/S0309170814000499/1-s2.0-S0309170814000499-main.pdf?\\_tid=53b98dd6-c71e-11e3-8c26-00000aacb35f&acdnat=1397842062\\_ccb2860ad6e21863dd5708bd4713e890](http://ac.els-cdn.com/S0309170814000499/1-s2.0-S0309170814000499-main.pdf?_tid=53b98dd6-c71e-11e3-8c26-00000aacb35f&acdnat=1397842062_ccb2860ad6e21863dd5708bd4713e890).

- Zeidouni, Mehdi, Susan D. Hovorka, Kewei Shi. 2016. Tracer test to constrain CO2 residual trapping and plume evolution. *Environmental Earth Sciences* **75** (22): 1451. <http://dx.doi.org/10.1007/s12665-016-6261-6>.
- Zeidouni, Mehdi, Jean-Philippe Nicot, SusanD Hovorka. 2014. Monitoring above-zone temperature variations associated with CO2 and brine leakage from a storage aquifer (in English). *Environmental Earth Sciences* **72** (5): 1733-1747. <http://dx.doi.org/10.1007/s12665-014-3077-0>.
- Zeidouni, Mehdi, Mehran Pooladi-Darvish. 2012a. Leakage characterization through above-zone pressure monitoring: 1—Inversion approach. *Journal of Petroleum Science and Engineering* **98–99** (0): 95-106. <http://www.sciencedirect.com/science/article/pii/S0920410512002215>.
- Zeidouni, Mehdi, Mehran Pooladi-Darvish. 2012b. Leakage characterization through above-zone pressure monitoring: 2—Design considerations with application to CO2 storage in saline aquifers. *Journal of Petroleum Science and Engineering* **98–99** (0): 69-82. <http://www.sciencedirect.com/science/article/pii/S0920410512002203>.
- Zeidouni, Mehdi, Nam H Tran, Muhammad D Munawar. 2017. Interpretation of above-zone pressure influence time to characterize CO2 leakage. *Greenhouse Gases: Science and Technology*.
- Zeidouni, Mehdi, V Vilarrasa. 2016. Identification of above-zone pressure perturbations caused by leakage from those induced by deformation (in English). *Environmental Earth Sciences* **75** (18): 1271.
- Zhang, Min, Stefan Bachu. 2011. Review of integrity of existing wells in relation to CO2 geological storage: What do we know? *International Journal of Greenhouse Gas Control* **5** (4): 826-840. <http://dx.doi.org/10.1016/j.ijggc.2010.11.006>.

## Appendix: Analytical Solution Development

The system of PDEs (equations (2.1) to (2.3)) and corresponding boundary conditions (Equations (2.4) and (2.5)) is made dimensionless using the following dimensionless parameters;

$$x_D = \frac{x}{d}, \quad y_D = \frac{y}{d}, \quad a_D = \frac{a}{d}, \quad b_d = \frac{b}{d}, \quad t_D = \frac{\eta t}{d^2}, \quad p_{Di} = \frac{kh}{q\mu} \Delta p_i \quad (2A-1)$$

where  $d$  represents a reference distance between injection/production (active) well and any observation location and  $i$  refers to the region 1, 2 or 3. Using these dimensionless parameters the governing PDE system becomes;

$$\frac{\partial^2 p_{D1}}{\partial x_D^2} + \frac{\partial^2 p_{D1}}{\partial y_D^2} + \delta(x_D - a_D) \delta(y_D) = \frac{\partial p_{D1}}{\partial t_D} \quad (2A-2)$$

$$\frac{\partial^2 p_{D2}}{\partial x_D^2} + \frac{\partial^2 p_{D2}}{\partial y_D^2} = \frac{C}{M} \frac{\partial p_{D2}}{\partial t_D} \quad (2A-3)$$

$$\frac{\partial^2 p_{D3}}{\partial x_D^2} + \frac{\partial^2 p_{D3}}{\partial y_D^2} = \frac{\partial p_{D3}}{\partial t_D} \quad (2A-4)$$

where  $M$  and  $C$  are the mobility ratio and storativity ratio respectively defined by:

$$M = \frac{(k/\mu)_a}{k/\mu}, \quad C = \frac{c_{ia}}{c_i}$$

Similarly, all boundary conditions are also made dimensionless by use of dimensionless parameters. These dimensionless boundary conditions for each zone are given by;

$$p_{Di}(x_D, -\infty, t_D) = 0 \quad \text{for } i=1,2,3 \quad (2A-5)$$

$$p_{Di}(x_D, \infty, t_D) = 0 \quad \text{for } i=1,2,3 \quad (2A-6)$$

$$p_{D1}(\infty, y_D, t_D) = 0 \quad (2A-7)$$

$$p_{D3}(-\infty, y_D, t_D) = 0 \quad (2A-8)$$

$$p_{D1}(b_D, y_D, t_D) = p_{D2}(b_D, y_D, t_D) \quad (2A-9)$$

$$p_{D2}(0, y_D, t_D) = p_{D3}(0, y_D, t_D) \quad (2A-10)$$

$$\left. \frac{\partial p_{D2}}{\partial x_D} \right|_{(b_D, y_D, t_D)} = \frac{1}{M} \left. \frac{\partial p_{D1}}{\partial x_D} \right|_{(b_D, y_D, t_D)} \quad (2A-11)$$

$$\left. \frac{\partial p_{D3}}{\partial x_D} \right|_{(0, y_D, t_D)} = M \left. \frac{\partial p_{D2}}{\partial x_D} \right|_{(0, y_D, t_D)} \quad (2A-12)$$

Analytical solutions for diffusivity equations given by equations (2A-2) through (2A-4) that are subject to initial and boundary conditions given by equations (2A-5) through (2A-12) are sought through application of Laplace and Fourier integral transforms. Laplace transform in time and the exponential Fourier transform in  $y$ -coordinate are applied which are defined by:

$$\bar{p}_D(x, y, s) = \mathcal{L}\{p_D(x_D, y_D, t_D)\} = \int_0^{\infty} p_D(x_D, y_D, t'_D) e^{-st'_D} dt'_D \quad (2A-13)$$

$$\tilde{\bar{p}}_D(x_D, \omega, s) = \mathcal{F}\{\bar{p}_D(x_D, y_D, s)\} = \int_{-\infty}^{\infty} \bar{p}_D(x_D, y'_D, s) e^{i\omega y'_D} dy'_D \quad (2A-14)$$

Application of Laplace and Fourier transforms convert the PDE system into ODE system in Laplace-Fourier domain given by:

$$\frac{d^2 \tilde{\bar{p}}_{D1}}{dx_D^2} - \omega^2 \tilde{\bar{p}}_{D1} + \frac{1}{s} \delta(x_D - a_D) = s \tilde{\bar{p}}_{D1} \quad (2A-15)$$

$$\frac{d^2 \tilde{\bar{p}}_{D2}}{dx_D^2} - \omega^2 \tilde{\bar{p}}_{D2} = \frac{C}{M} s \tilde{\bar{p}}_{D2} \quad (2A-16)$$

$$\frac{d^2 \tilde{\bar{p}}_{D3}}{dx_D^2} - \omega^2 \tilde{\bar{p}}_{D3} = s \tilde{\bar{p}}_{D3} \quad (2A-17)$$

where  $\tilde{\bar{p}}_D$  indicates that dimensionless pressure is in Laplace and Fourier domain. Boundary conditions over  $x_D$  are translated into Fourier and Laplace domain as;

$$\tilde{\bar{p}}_{D1}(b_D, \omega, s) = \tilde{\bar{p}}_{D2}(b_D, \omega, s) \quad (2A-18)$$

$$\tilde{\bar{p}}_{D2}(0, \omega, s) = \tilde{\bar{p}}_{D3}(0, \omega, s) \quad (2A-19)$$

$$\left. \frac{\partial \tilde{\bar{p}}_{D2}}{\partial x_D} \right|_{(b_D, \omega, s)} = \frac{1}{M} \left. \frac{\partial \tilde{\bar{p}}_{D1}}{\partial x_D} \right|_{(b_D, \omega, s)} \quad (2A-20)$$

$$\left. \frac{\partial \tilde{\bar{p}}_{D3}}{\partial x_D} \right|_{(0, \omega, s)} = M \left. \frac{\partial \tilde{\bar{p}}_{D2}}{\partial x_D} \right|_{(0, \omega, s)} \quad (2A-21)$$

All the PDEs are now linearized and have been converted into ODEs. ODE for Region 1 given by Equation (2A-15) is non-homogeneous while those for region 2 and 3 are homogeneous. Solution of these ODEs by application of variation of parameters method and solving characteristic polynomial equation (Kreyszig 2011) are as follows;

$$\tilde{\bar{p}}_{D1} = \frac{1}{2As} e^{-A|x_D - a_D|} + C_1 e^{-Ax_D} \quad (2A-22)$$

$$\tilde{\bar{p}}_{D2} = C_2 e^{Bx_D} + C_3 e^{-Bx_D} \quad (2A-23)$$

$$\tilde{\bar{p}}_{D3} = C_4 e^{Ax_D} \quad (2A-24)$$

where  $A^2 = \omega^2 + s$  and  $B^2 = \omega^2 + \frac{C}{M}s$ .

Here  $C_1$ ,  $C_2$ ,  $C_3$  and  $C_4$  are constants of general solutions that can be determined by finding particular solution using boundary conditions given by equations (2A-18) through (2A-21). Application of boundary conditions and solving linear system of equations for these constants results in:

$$\tilde{\tilde{p}}_{D1} = \frac{e^{-A|a_D - x_D|} + \frac{e^{-A(a_D - 2b_D + x_D)}(-1 + e^{2Bb_D})(A - BM)(A + BM)}{-(A - BM)^2 + e^{2Bb_D}(A + BM)^2}}{2As} \quad (2A-25)$$

$$\tilde{\tilde{p}}_{D2} = \frac{e^{A(-a_D + b_D)}(BM \cosh(Bx_D) + A \sinh(Bx_D))}{(2ABMs \cosh(Bb_D) + (A^2 + B^2M^2)s \sinh(Bb_D))} \quad (2A-26)$$

$$\tilde{\tilde{p}}_{D3} = \frac{2Be^{Bb_D + A(-a_D + b_D + x_D)}M}{-(A - BM)^2s + e^{2Bb_D}(A + BM)^2s} \quad (2A-27)$$

## Appendix: Acknowledgement Forms

3011 Grassy Lake Drive  
Baton Rouge, 70816  
2/14/2018

Mehdi Zeidouni  
Louisiana State University  
3209 Patrick F. Taylor Hall  
Baton Rouge, LA 70803

Dear Dr. Zeidouni:

I am completing an MSc dissertation at Louisiana State University entitled "Pressure Transient Techniques for Continuous Monitoring of CO<sub>2</sub> Storage/EOR." I would like your permission to reprint the following material in my dissertation:

"Interpretation of above-zone pressure influence time to characterize CO<sub>2</sub> leakage" *Greenhouse Gases Science and Technology* Volume 7, Issue 6 (2017): 1050-1064


The requested permission extends to any future revisions and editions of my dissertation, including nonexclusive world rights in all languages. These rights will in no way restrict republication of the material in any other form by you or by others authorized by you. Your signing of this letter will also confirm that you own the copyright to the above-described material, or that you otherwise have sufficient rights to the material in order to grant the requested permission.

To grant this permission, please sign where indicated below and return it to me in the enclosed return envelope. Please contact me should you have any questions or need additional information. Thank you very much.

Sincerely,



Nam Tran

_____ Mehdi Zeidouni _____ Printed Name
_____  _____ Signature
_____ February 15, 2018 _____ date
Acknowledgement: <i>Permission is granted to Mr. Nam H. Tran to include the above mentioned paper in his thesis</i>

3011 Grassy Lake Drive  
Baton Rouge, 70816  
2/28/2018

Muhammed Dawood  
Flat # 8, Block # 10, PHA Flats, G-8/4  
Islamabad, 44080

Dear Mr. Munawar:

I am completing a MSc dissertation at Louisiana State University entitled "Pressure Transient Techniques for Continuous Monitoring of CO<sub>2</sub> Storage/EOR." I would like your permission to reprint the following material in my dissertation:

"Interpretation of above-zone pressure influence time to characterize CO<sub>2</sub> leakage" *Greenhouse Gases Science and Technology* Volume 7, Issue 6 (2017): 1050-1064

The requested permission extends to any future revisions and editions of my dissertation, including nonexclusive world rights in all languages. These rights will in no way restrict republication of the material in any other form by you or by others authorized by you. Your signing of this letter will also confirm that you own the copyright to the above-described material, or that you otherwise have sufficient rights to the material in order to grant the requested permission.

To grant this permission, please sign where indicated below and return it to me in the enclosed return envelope. Please contact me should you have any questions or need additional information. Thank you very much.

Sincerely,



Nam Tran

Muhammad Dawood Munawar  
Printed Name



\_\_\_\_\_  
Signature

01<sup>st</sup> March, 2018  
Date

Acknowledgement: *Permission is granted to Nam H. Tran to include the above mentioned paper in his thesis.*



## **Vita**

Nam Hoang Tran, born in Gulfport Mississippi, earned his bachelor's degree in petroleum engineering from Louisiana State University. Afterwards, he continued his education at the same institution in pursuit of a master's degree in petroleum engineering. Upon completion of his master's degree, Nam wishes to work in the oil industry.